Nanotemplates and Conformations of Tri-Metal Endofullerenes on Surfaces

Dissertation

zur

Erlangung der naturwissenschaftlichen Doktorwürde
(Dr. sc. nat.)

vorgelegt der

Mathematisch-naturwissenschaftlichen Fakultät
der
Universität Zürich

von

Roland Stania
aus Deutschland

Promotionskommission
Prof. Dr. Thomas Greber (Vorsitz)
Prof. Dr. Jürg Osterwalder
Prof. Dr. Pietro Gambardella

Zürich 2016

Das Volumen des Festkörpers wurde von Gott geschaffen,
seine Oberfläche aber wurde vom Teufel gemacht.

Wolfgang Pauli

Abstract

65 years after the predictions of Gordon Moore, the doubling of the complexity of integrated electronics per two years, further miniaturization in devices is reaching a limiting barrier due to effects like quantum confinement and superparamagnetism. As Moore's law is not in effect anymore, new approaches towards nanostructures and alternatives to conventional Silicon (Si) based electronics become more important. In this dissertation two main approaches are presented: Nanotemplate structures on metallic alloys and detailed structural analysis of single molecule magnets on surfaces, good candidates for a *spintronic* approach, the usage of magnetic spin direction in addition to the electric charge to store and read information.

X-ray photoelectron diffraction (XPD) is a strong method for surface sensitive and element specific structural analysis. While conventional channeltron analyzer based XPD is a well understood method, novel two dimensional analyzers, as used in the PhotoEmission and Atomic Resolution Laboratory (PEARL) of the Swiss Light Source (SLS) (as introduced in Section 3.2), require new evaluation methods due to angle-dependent transmission function effects. A new normalization and evaluation routine was developed and is presented in Section 4.

Self-assembly of nanostructures as a method of modern nanotechnology has many possible applications, from hydrogen storage and catalysis towards magnetic information storage. In Section 5, the self-assembly of nanoscale lateral segregation profiles, the formation of highly ordered, nanometer sized patches in the top layer of transition metal alloys, formed during the growth of a nanomesh-like, single layer of *h*-BN, is presented. For the case of a PtRh alloy, Rh patches are formed and isolated from each other by a 'sea' of Pt atoms, as concluded from experiments and density functional theory. Similar segregation profiles can be expected, using different alloy combinations and thus the findings can be extended to form nanometer sized magnetic domains.

With the rising interest in the research towards spintronic devices, single molecule magnets are gaining more and more attention. While many single molecule magnets were characterized, based on their magnetic properties, mainly scanning tunneling microscopy investigations were performed in the field of structural analysis in the presence of a surface. Tri-metal endofullerenes like $\mathrm{TbSc_2N@C_{80}}$ show high thermal stability and often count to the single molecule magnet family if they contain lanthanides. The structural behavior and the different conformations, both the endohedral unit and the carbon cage can assume - with respect to each other and to surfaces - is rigorously discussed in Section 6. Multiple degrees of freedom and possible conformations are identified, using surface science techniques. Temperature resolved studies concluded transitions from a well aligned conformation in an immobilized setup, in alignment with the substrate at low temperatures, over a free three-dimensional motion of the endohedral unit within an immobilized carbon cage at intermediate temperatures, up to motion of the endohedral unit and the cage at room temperatures.

Zusammenfassung

65 Jahre nach Gordon Moores Voraussagen, daß sich die Komplexität integrierter elektronischer Schaltkreise im Zweijahresrhythmus verdoppeln würde, erreichen die Versuche, weiterhin die Miniaturisierung von Schaltkreisen voranzutreiben, ihre Grenzen, aufgrund von Effekten wie Quantenconfinement und Superparamagnetismus. Mit dem Ende der Gültigkeit von Moore's Law steigt die Wichtigkeit neuer Ansätze, um Nanostrukturen und Alternativen zu konventionellen Si-basierten Schaltkreisen zu finden. In dieser Dissertation werden zwei Ansätze präsentiert: Die Formierung von Nanoschablonen in metallischen Legierungen, sowie eine detaillierte Studie bezüglich des strukturellen Verhaltens von monomagnetischen Molekülen auf Oberflächen, was ein vielversprechender Ansatz ist, um Spintroniken, die Nutzung der magnetischen Spinausrichtung zusätzlich zur elektrischen Ladung, zwecks Informationsspeicherung, zu realisieren.

Röntgenphotoelektronendiffraktion ist ein mächtiges Werkzeug für oberflächensensitive und elementspezifische Strukturanalysen. Während die Nutzung konventioneller Channeltronanalysatoren sich als altbewährtes Standartverfahren etabliert hat, ist die Umsetzung der Messmethode, unter Verwendung der neuen Generation von zweidimensionalen Channelplate-Detektoren, wie auch verwendet im *PhotoEmission and Atomic Resolution Laboratory* (PEARL) an der Swiss Light Source (beschrieben in Kapitel 3.2), noch nicht etabliert. Neue Normalisierungsverfahren und Evaluationsroutinen sind von Nöten, um den winkelabhängigen Einfluß der Transmissionfunktion zu umgehen. Diese Routinen werden in Kapitel 4 präsentiert und diskutiert.

Die eigenständige Anordnung von Nanostrukturen, als eine Basis für moderne Nanotechnologie, ist vielversprechend für viele mögliche Anwendungen. Diese reichen von Wasserstoffspeicherung, über katalytische Oberflächennutzung, bis hin zu magnetischer Speicherung von Informationen. In Kapitel 5 wird die selbstständige Anordnung von lateral segregierten Profilen auf der Nanometerskala präsentiert: Die Formierung von hochgradig geordenten, nanometergroßen, voneinander separierten Zonen in der obersten Schicht einer Legierung aus Übergangsmetallen, die sich während des Wachstums eines monoatomar dünnen Films hexagonalen Bornitrids formt. Für den Fall einer Platin-Rhodium Legierung formen sich Rhodiumzonen, die strikt voneinander getrennt sind, und von einem 'Meer' aus Platin umgeben sind, wie aus einer Reihe von experimentellen Untersuchungen und theoretischer Berechnungen (DFT) geschlussfolgert werden kann. Ein ähnliches Segregationsverhalten ist für verschiedenste Legierungszusammensetzungen zu erwarten, und sollte auf die gleiche Art und Weise auch für die Erzeugung von geordneten magnetischen Nanodomänen übertragbar sein.

Mit dem wachsenden Interesse an der Forschung in Richtung Spintronik werden auch monomagnetische Moleküle (SMM) immer wichtiger. Zwar wurden schon viele SMMs charakterisiert und untersucht, allerdings beschränkt sich ein Großteil der Forschung auf die Untersuchung der magnetischen Eigenschaften und strukturelle Analysen im Einflußbereich einer Oberfläche wurden hauptsächlich unter Nutzung von Rastertunnelmikroskopie durchgeführt. Trimetallische Endofullerene, wie $TbSc_2N@C_{80}$, weisen eine hohe thermische Stabilität auf und zählen meist zur Familie der monomagnetischen

Moleküle, wenn sie Lanthanide beinhalten. Das strukturelle Verhalten und die verschiedenen Konformationen, die, sowohl endohedrale Einheit, als auch Kohlenstoffkäfig, zueinander und in Bezug auf die Oberfläche, annehmen können, wird detailliert in Kapitel 6 diskutiert. Mehrere Freiheitsgrade und mögliche Konformationen können identifiziert werden, unter Nutzung von Meßmethoden der Oberflächenphysik. Die verschiedenen Anordnungen reichen hierbei von einer Konformation in eingefrorenem Zustand mit ausgerichteter endohedralen Einheit bei tiefen Temperaturen über eine freie dreidimensionale Bewegung der endohedralen Einheit bei bewegungslosem Kohlenstoffkäfig, bis hin zu zwei voneinander unabhängigen Bewegungen, von endohedraler Einheit und Kohlenstoffkäfig, bei Raumtemperatur.

Contents

1. Introduction

In 1965 Gordon E. Moore predicted the doubling of the complexity (the number of transistors) of integrated electronics per year. He predicted that production costs will be reduced with the increment of required components in addition to the development of microelectronics and miniaturization to fight off heat dissipation problems and that no physical barrier existed but that of thermodynamics as encountered in chemical reactions [1].

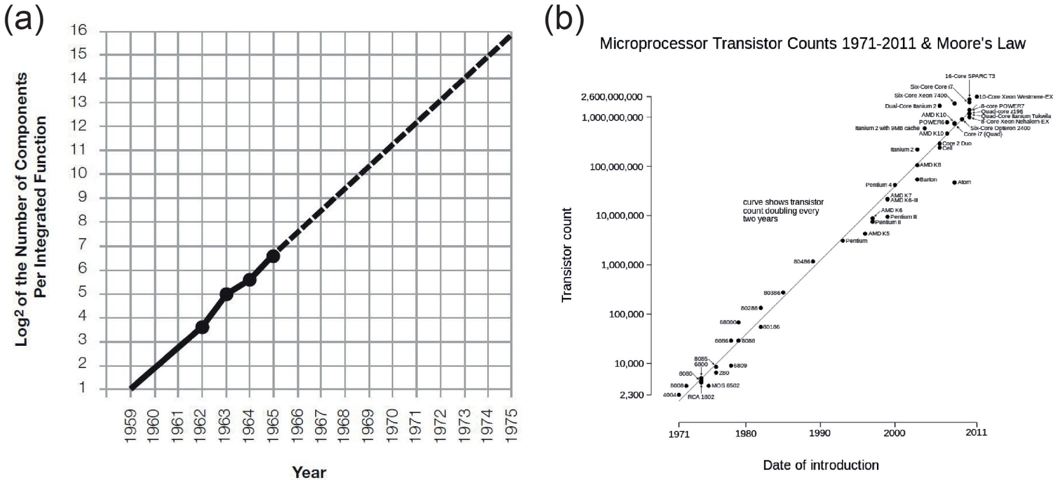

Figure 1: Moore's law: (a) original prediction published in 1965 [1]; (b) development of microprocessor transistor counts until 2011 (taken from [2]).

Even though he corrected his prediction two years later to a doubling per two years, it became known as *Moore's law* and was a reliable rule until 2015, as shown in Figure 1: The original graph by Moore in (a) compared to a sketch about the development until 2011.

It took 51 years until the miniaturization reached the borders of classical physics and global leading chip developers (Intel, AMD, TSMC, GlobalFoundries and IBM) reported the first deviation from this law as reported in [3].

At the current size of microelectronics in the nanometer scale and the atomic limit, local structural defects gain an increasing effect on the circuits. Additionally, quantum confinement occurs at structural sizes in the magnitude of Bohr's radius, leading to atoms and transitions from continuous to discrete energy levels. Also, at sizes in the nanometer scale, of ferromagnetic and ferrimagnetic material loses its properties to maintain stable magnetization below the Curie temperature - called the superparamagnetic limit [4].

To further press the process of miniaturization, alternative concepts to the silicon based transistor technology are required. The creation of nanostructures using novel materials like sp^2 layers, the emerging field of *spintronics* and *quantum computing* are promising candidates for future developments.

1.1. Spintronics

Conventional electronics base on the manipulation of electronic charge. As an alternative concept, *spintronics* move away from pure charge manipulation and focuses on the manipulation of the electronic spin in different materials, to access the possibility of reading and writing information using magnetism. Spin based devices, or the combined use of spin and conventional charge in devices, promise an increased processing rate at a reduced power consumption [5].

In addition to the traditional spin information (up and down), also the alignment, with respect to an external field, can be used as further information.

This novel research field is full of major challenges, like the optimization of life times, the fast detection of spin in nanostructures and the manipulation of nuclear and electron spin.

Most renown approaches to implement spintronics are *spin valves*, giant magneto-resistive effect (GMR) based devices, and *magnetic tunnel junctions* (MTJ), devices with a pinned layer and a free layer, being separated by insulating thin layers. Both can be combined to MRAM devices to store data using magnetic hysteresis, while the read out is performed using magnetoresistance.

1.2. sp^2 layers on alloys

sp^2-hybridized material or layers require a π-bond for the double-bonds between atoms, while only three σ-bonds are formed. Most renown is Graphene, a unique material consisting out of a monolayer of hexagonally ordered Carbon atoms, which is a gapless semiconductor with exotic transport properties. The cousin of graphene is hexagonal boron nitride (h-BN) which, contrary to graphene, is a large bandgap insulator. While properties and characteristics of h-BN were investigated using epitaxially grown monolayer on many substrates [6–15], few investigations were performed concerning the influence of grown sp^2 layers on surfaces.

While only minor influence on the substrate may be expected for the case of sp^2 layers grown on single crystals, the effect on alloys can be expected to create new types of surfaces. A nanomesh-like structure as h-BN grown on rhodium (Rh) [13] or graphene on ruthenium (Ru) [16] would enforce different strains and adhesive forces between the sp^2 layer and the substrate - and this on the nanometer scale. The correct combination of metals as substrate - in form of a two (or multi) component alloy - and grown sp^2 layer can result in surface segregation effects and thus the formation of nano-templates. Going further this can be used as a lever to solve miniaturization problems for catalysts and magnetic storages.

1.3. Single Molecule Magnets

Since the finding of long magnetization times in absence of external magnetic fields for molecular transition metal coordination compounds in the early 1990s [17] the large family of *single molecule magnets* (SMM) [18] became more and more an area of interest [19]. SMMs can be considered as molecular equivalents of classical bulk ferromagnets and can serve as an approach to realize new technical applications and spintronics [20]. Major technical problems are faced in order to realize SMM-based technology: The unique properties of SMMs are only accessible at low temperatures (liquid Helium temperature regime) and only few SMMs were investigated on surfaces yet. To visualize the example, the *web of knowledge* [21] counted 2457 entries for "Single Molecule Magnet" but only 102 entries which also considered "surface" in the topic (August 2016).

The quality of an SMM can is defined by three main properties. First the magnetic blocking temperature, which is the highest temperature at which hysteresis is still shown in a magnetization curve. Second, the strength of the coercive magnetic field required to drive the magnetization of a powder sample of SMM to zero. Third, the anisotropy barrier (energy barrier) to reverse the magnetization and to turn the SMM into a paramagnet.

SMMs designed with high anisotropy barriers appear to be single-ion magnets containing lanthanides (Ln) [22–24] and actinides (Ac) [25, 26]. Especially the Ln-SMMs containing Terbium (Tb) and Dysprosium (Dy) are promising candidates due to large and unquenched magnetic moments, small but significant ligand fields [27] and the large magnetic quantum number m_j of the ground state. While Dy-SMMs are more numerous due to Dy(III) being a Kramers' ion - a system with a half-integer total spin due an odd number of electrons - the Tb-SMMs are of great interest due to a very large anisotropy barrier.

1.4. Scope of this thesis

This thesis follows a *bottom-up* approach, coming from the basic science approach towards a more generalized outlook. In order to functionalize new materials such as nano patches of different metallic components or single molecule magnets, structural analysis and sample preparation techniques are indispensable. Structural analysis of the properties of new material is the foundation for further research.

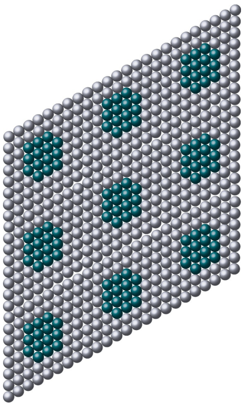

Figure 2: Sketch of a laterally segregated nanotemplate: Rh atoms (green) for isolated patches surrounded by Pt atoms (grey).

This work combines a multiplet of different surface sensitive characterization methods of electron spectroscopy, mainly x-ray photoelectron diffraction, and focuses on two different aspects of new functionalizable material.

In Section 5 the influence of epitaxially grown hexagonal boron nitride on transition metal alloys is investigated, at the example of a $Pt_{50}Rh_{50}$ single crystal. The resulting lateral segregation effect that forms nanometer sized, isolated Rh patches, are representative for a large array of possible alloy combination and are not only of interest for catalysis, but also for the creation of nano-magnetic surfaces by exchanging the alloy components (for example to Fe_xPt_{100-x}).

In Section 6 the structural conformations of one monolayer of the SMM $TbSc_2N@C_{80}$ on a *h*-BN/Ni(111) surface is investigated. Again, the choice of the endofullerene is representative for the behavior of relatives of the endofullerene family since the influence of the surface should have comparable effects on the conformation of the SMMs.

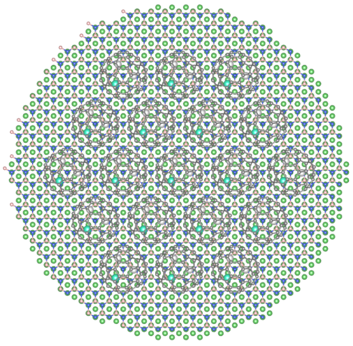

Figure 3: Sketch of $TbSc_2N@C_{80}/h$-BN/Ni(111) from top.

2. Methods

In this section an overview is given on the methods which were used in this thesis. In particular *X-ray Photoelectron Spectroscopy* (XPS) and *X-ray Photoelectron Diffraction* (XPD) will be described. *Low Energy Electron Diffraction* (LEED) and *Scanning Tunneling Microscopy* (STM) are briefly described, followed by a short introduction into *Supraconducting QUantum Interference Device* (SQUID) techniques. For the interested reader all those methods are rigorously discussed in standard literature [18, 28–30].

2.1. Photoelectron Spectroscopy

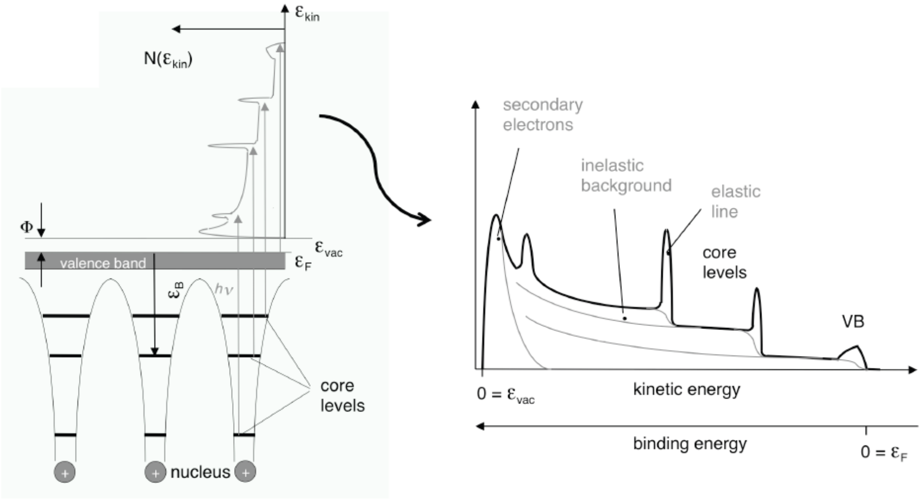

Figure 4: Schematic view of a photoelectron emission process: the left sketch shows the process covered by the *three-step model* - right: sketch of a measured XPS spectrum with elastic lines; Figure taken from [30].

Modern Photoelectron Spectroscopy or Electron Spectroscopy for Chemical Analysis (ESCA) [31, 32] bases on Einstein's photoelectric effect described in 1905 [33]. In an absorption process the full energy of a light quantum $h\nu$ excites a single electron from an occupied state into the vacuum following

$$E_K = h\nu - E_B - \Phi, \tag{1}$$

where E_K and E_B are kinetic and binding energy (usually with respect to the Fermi energy) and Φ is the material dependent work function. Based on the inelastic mean free path of an electron in a solid this method is very surface sensitive as the mean free path of a photoelectron is energy dependent and is in the order of $\lambda = 1$ nm for soft x-rays (500 eV $< h\nu <$ 2000 eV). The information in a photoemission spectrum is manifold: The elastic lines, which indicate the core levels of the electrons give quantitative information about the chemical composition of the material, Auger electrons, that originate from secondary processes where a given energy, independent of the photon energy, from a core-hole recombination is released, fixes the Auger electrons at one kinetic energy. The inelastic background originates from inelastic processes and shows strong emission increments at each elastic line.

The process of a photoelectron absorption can be described in numerous ways but a common insight is given by the *three-step model* [34]:

1. Absorption of the photon $h\nu$ by a core electron. The electron is excited from the initial state $|\psi_i\rangle$ with a binding energy E_B in the solid to a final state $|\psi_f\rangle$ with a kinetic energy E_K, following Fermi's golden rule:

   $$\Gamma_{i\to f} = \frac{2\pi}{\hbar} \left|\langle f|H'|i\rangle\right|^2 \rho, \tag{2}$$

   where ρ is the density of final states and $\langle f|H'|i\rangle$ the matrix element of the pertrubation H' between initial state and final state. Energy conversation is given by the relation between initial and final energy following

   $$E_f(\vec{k}_f) = E_i(\vec{k}_i) + h\nu \tag{3}$$

   At the same time momentum conversation has to be fulfilled. This is realized with an addition of a reciprocal lattice vector $\vec{G}$:

   $$\vec{k}_f = \vec{k}_i + \vec{k}_{h\nu} + \vec{G}, \tag{4}$$

   in terms of the Bloch theorem and a momentum of the photon $\vec{k}_{h\nu}$. The final state can be approximated to behave like a free electron with the energy

   $$E_f = \frac{\hbar^2 \vec{k}_f^2}{2m} \tag{5}$$
   $$E_f = h\nu - E_B - \Phi + V_0, \tag{6}$$

   with the material specific inner potential V_0.

2. Transport of the electron through the solid. The electron moves as a wave with a wave vector of the magnitude

   $$|\vec{k}| = \sqrt{\frac{2mE_k}{\hbar^2}} \tag{7}$$

   and undergoes inelastic scattering mainly via electron hole pair excitations and recombinations of electron-hole pairs. The exponential dampening is described by the inelastic mean free path λ [35] and under neglecting of scattering effects the initial intensity I_f reduced at the surface to $I_{f,s}$ can be written as:

   $$I_{f,s} = I_f \cdot \exp\left(-\frac{d}{\lambda \cdot \cos(\theta_i)}\right), \tag{8}$$

   with the depth d of the excited atom below the surface. θ_i is the angle between the surface normal and the electron trajectory in the solid.

3. Surface potential step and refraction step. The electron transmigrates from the solid surface to vacuum. The surface potential barrier V_0 causes a reduction of the perpendicular momentum $\vec{k}_\perp$ while the parallel component $\vec{k}_{||}$ is conserved and can be calculated as

$$\vec{k}_{||} = \frac{\sqrt{2mE_K} \cdot \sin(\theta)}{\hbar} \cdot \begin{pmatrix} \cos\phi \\ \sin\phi \\ 0 \end{pmatrix}, \tag{9}$$

   with the polar angle θ and the azimuthal angle ϕ with respect to the sample normal. The perpendicular momentum inside the solid can be obtained from the final state energy E_f and the inner potential V_0 that is a priori not known:

$$\vec{k}^s_\perp = \frac{\sqrt{2m(E_K + V_0)}\cos(\theta_i)}{\hbar} \cdot \vec{e}_z. \tag{10}$$

   This can be used to express Snell's law for electron refraction when escaping the surface:

$$\frac{\sin\theta^s}{\sin\theta} = \sqrt{\frac{E_k}{E_k + V_0}}. \tag{11}$$

Resonant Photoelectron Spectroscopy

The tunable x-ray photon energy in synchrotron facilities allows to take advantage of the increased cross section when the photon energy $h\nu$ is near the absorption edge of a core level [36] and the matrix element of Equation 2 increases, if initial state and final state are localized on the atom.

The core electron is excited into an unoccupied state in the valence band, at the same time as a valence electron, with a binding energy E_{B_1}, recombines with the core hole in an Auger process to deliver enough energy to excite a valence electron with a binding energy E_{B_2}.

While the solid is left behind with two electron-holes during the Auger process, no dipole selection rules apply for the excited and the recombining electron, as there is no necessity to couple to a photon. Nevertheless, the overall angular momentum has to be conserved in the process [37]. The Auger-excited valence electron has the same final state as if excited by direct photoemission, though carries the larger oscillating strength of the core hole.

Usually the MNN processes for the case of rare earths, as used in this thesis, show a broad amount of excitations, as described by Laubschat *et al.* [38] for several rare earths. In addition, the electrons with binding energy E_{B_2} are excited in a normal photoemission process and both final states are identical. The interference of both processes lead to a *Fano*-type lineshape [39] with an enhanced signal of more than one order of magnitude. Resonant Photoelectron Spectroscopy is a method of choice when small contributions (in the order of 1% coverage) of a sample are to be investigated. One of these processes is shown in Chapter 6.8.2.

2.2. Photoelectron Diffraction

A powerful tool to investigate crystalline structures in a chemically sensitive way is X-ray Photoelectron Diffraction (XPD) [30, 40, 41]. As the electron waves propagate through a sample, in step two of the *three-step model*, they can be elastically scattered at atomic sites. The resulting self-interference or diffraction patterns are reflected in the measured intensity distribution $I(\theta, \phi)$ above the hemisphere. The chemical sensitivity is obtained by the measurement of a core level of a given atomic species. If these emitter species have the same surrounding, like it is for example given in a crystal, the surrounding positions of the scattering atoms may be determined.
For kinetic electron energies above $E_K > 200$ eV forward scattering effects dominate and neighboring positions of an emitting atom are visible as dots allowing a direct read out of emitter-scatterer directions from the diffraction patterns. Patters created by higher order diffraction interferences can be simulated using single scattering cluster calculations (SSC) or multiple scattering cluster simulations (MSC, EDAC) [42–44]. By iterative variation of the clusters and comparison to the experimental data, structures under investigation can be determined.

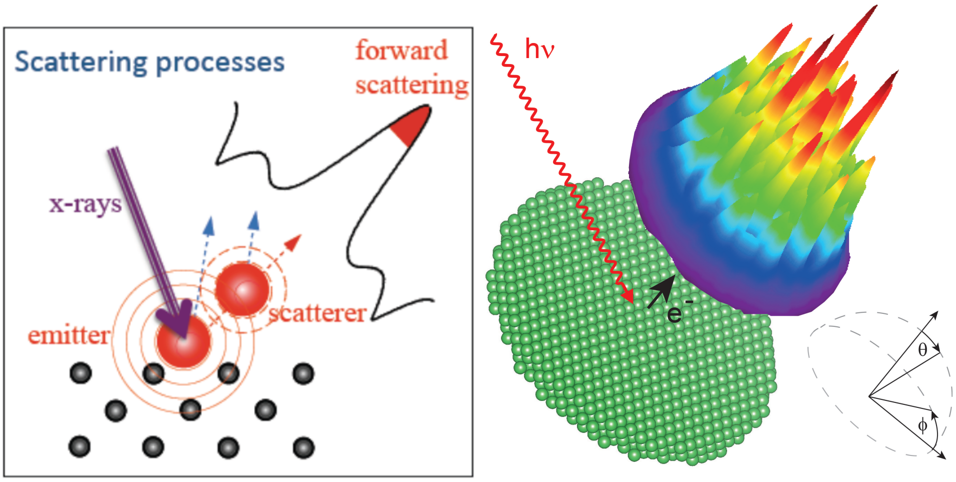

Figure 5: left side: Schematic view of the scattering process in a crystalline structure. An excited electron scatters at neighboring atoms creating an interference pattern with a forward scattering peak. Figure taken from [30]; right side: visualization of the stereographic projection in the hemisphere above the sample.

X-ray Photoelectron Diffraction patterns are usually displayed in a stereographic map where the center corresponds to normal emission angle ($\theta = 0°$) and a radius $r \propto \tan\left(\frac{\theta}{2}\right)$.

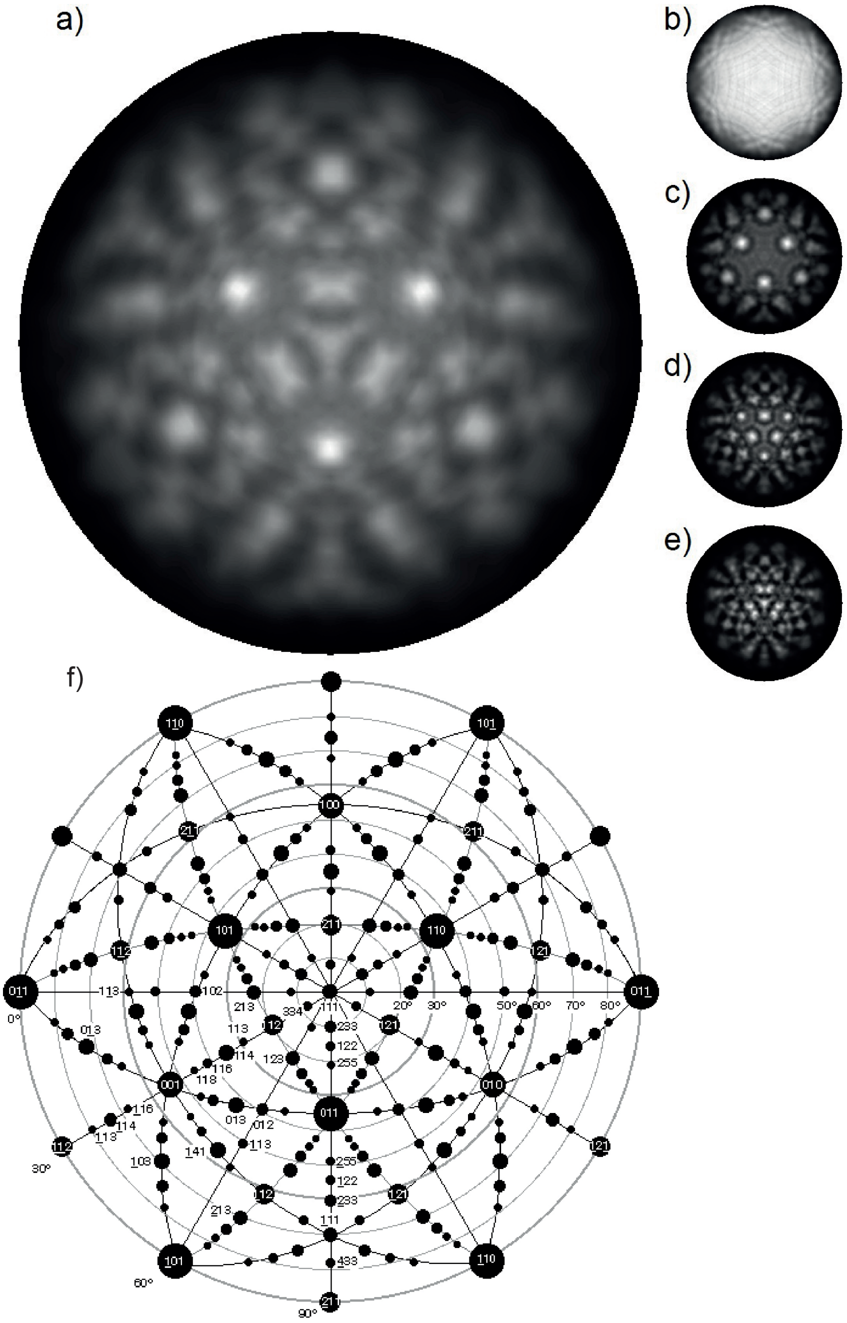

Figure 6: XPD forward scattering effects shown at the example of a simulation using the EDAC code [44]: (a) simulation of a Rh $3d_{5/2}$ pattern of an fcc(111) crystal structure (b)-(e) single layer simulations showing the influence of different emitter atoms inside the crystal; (f) stereographic projection of the the forward scattering positions of an fcc(111) single crystal. Figures a-e taken from [45]; Figure f taken from [46].

At grazing angles the photoemission intensity dies off due to refraction and transmission effects [47]. In order to make diffraction patterns at grazing angles better visible often a *phi averaged* procedure is done where each angular intensity $I = I(\theta, \phi)$ is divided by the average of all azimuthal angles at the given polar angle θ resulting in

$$I_{np}(\theta, \phi) = I(\theta, \phi) \cdot \left(\frac{\sum\limits_{i=0}^{N(\theta)} I(\theta, \phi_i)}{N(\theta)} \right)^{-1} , \tag{12}$$

where $N(\theta)$ is the number of points for one polar setting.
As one powerful application X-ray Photoelectron Diffraction can be done using resonantly excited electrons in order to investigate the structures containing minimal amounts of specific chemical elements like endofullerenes.

2.3. Low Energy Electron Diffraction

Low Energy Electron Diffraction (LEED) is a method to investigate the arrangement of atoms and structures at surfaces. An electron gun (usually using a LaB_6 filament / cathode) creates an electron beam of well defined energy and momentum. The electrons are backscattered from the sample and by interference of electron waves diffraction patterns are created which can be recorded by a phosphorous screen using a CCD camera. Here the relation between the energy of the electrons and the De-Broglie wavelength λ is given by

$$\lambda = \frac{h}{\sqrt{2m(E_K + V_0)}}. \tag{13}$$

Due to the elastic scattering and the extremely short mean free path of electrons at kinetic energies in the regime of $E_K \approx 100$ eV, the method is very surface sensitive and the electrons only have a penetration depth of $0.5 - 1$ nm.

2.4. Scanning Tunneling Microscopy

Scanning Tunneling Microscopy (STM) allows a direct access visualize the electronic density of states (DOS) up to atomic resolution of the top atoms. It uses an atomically sharp metallic tip (in our case Tungsten) to scan above the surface. A bias voltage V_B is applied between tip and sample surface and the tunneling current is measured. For the case of low bias voltages the tunneling current can be approximated by the density of states n, the distance between tip and sample d and the work functions of sample and tip Φ_S and Φ_T as

$$I_T \propto n(E_F) \cdot \exp\left(-2d \cdot \kappa\right), \tag{14}$$

with the *Gamov* factor

$$\kappa = \sqrt{\frac{2m(\Phi_T + \Phi_S)}{2\hbar^2}}. \tag{15}$$

For negative (positive) bias voltage the STM technique allows to map filled (unfilled) states in the electronic structure of the sample. While there are two different scanning modes (*constant height mode* and *constant current mode*) in this thesis only *constant current modus* was used where the distance d between tip and surface is adjusted basing on the changes in measured tunneling current by a piezo controlled feedback loop. The height is then mapped in form of a topographic image of the surface.

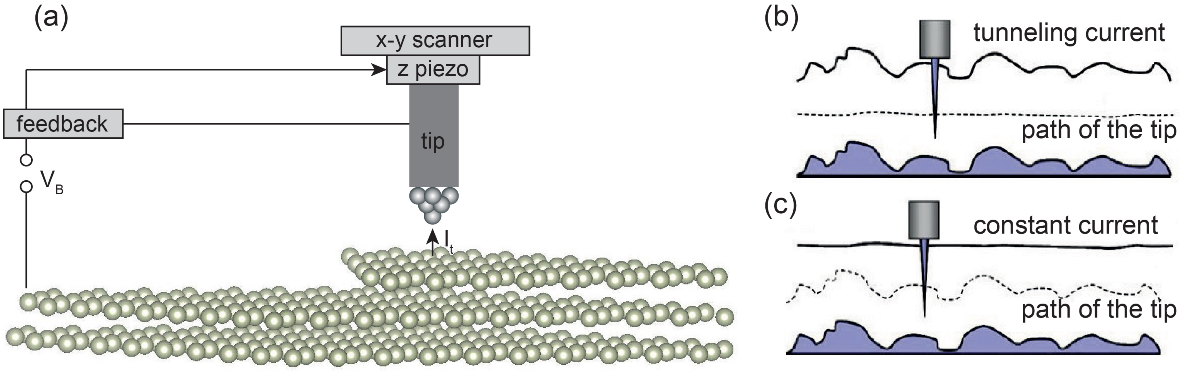

Figure 7: Schema of an STM: a) shows the setup of feedback loop controlling the z-scanner via piezo crystals. (b) and (c) the different modi for scanning: *constant height mode* (b) and *constant current mode* (c). Figures (b) and (c) taken from [48].

2.5. SQUID Magnetometry and AC susceptometry

Following Faraday's law, a time-dependent magnetic flux creates an electric field and forces charges to flow in closed circuits with a force

$$F \propto -\frac{d\Phi}{dt}. \tag{16}$$

This induced current can be measured by coils inductively coupled to a *Superconducting QUantum Interference Device* (SQUID) under usage from the flux quantization in a superconducting loop and a non-superconductive barrier in the SQUID ring, called a Josephson junction - where the Cooper pairs can tunnel. This allows to measure an extremely low magnetic flux.

AC susceptometry allows direct access to the magnetic susceptibility

$$\chi = \frac{\partial M}{\partial H}, \tag{17}$$

with the use of a two-coil setup inside a SQUID magnetometer as shown in Figure 8. Here the sample is positioned inside a primary coil with an applied alternating current, creating a small oscillating magnetic field. Usually the two secondary coils are winded in opposite directions, in order to reduce the induced voltage to zero in absence of a sample.

After inserting a sample, the ac field causes an oscillation of the magnetic moment and thus induces a measurable voltage in the secondary coil.
Having a static field H_0 parallel to the oscillating small field h results in

$$H = H_0 + h\cos(\omega t), \tag{18}$$

with the angular frequency ω of the oscillating field. This method is ideal to investigate the magnetic behavior of samples at a low applied static fields and allows to investigate the dynamics of magnetization by a variation of the angular frequency.

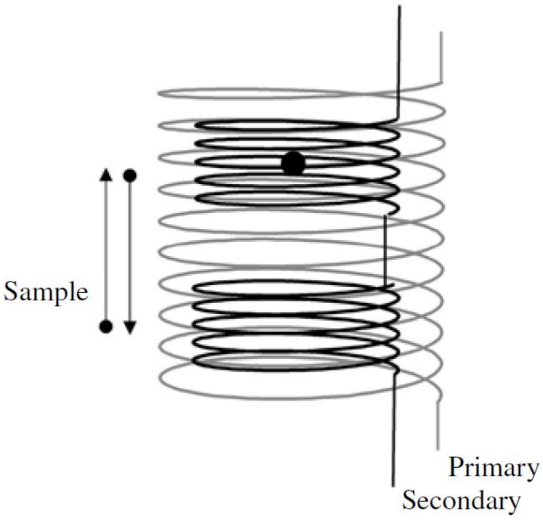

Figure 8: Schematic view of primary and secondary coil used in AC susceptometry. Figure taken from [18].

For the system to achieve thermal equilibrium a relaxation time τ is required. For the case of $\omega\tau << 1$ only the isothermal susceptibility χ_T is measured while for the opposing case of $\omega\tau >> 1$ no exchange energy can be transfered and thus only the adiabatic susceptibility χ_S can be measured.
For the case of $\omega\tau \approx 1$ the susceptibility can be interpreted as

$$\chi(\omega) = \chi_S + \frac{\chi_T - \chi_S}{1 + i\omega\tau}, \tag{19}$$

basing on Casimir and Du Pré [49]. For $\{\chi_S, \chi_T\} \in \mathbb{R}$ the real component χ' and imaginary component χ'' of the susceptibility become:

$$\chi' = \chi_S + \frac{\chi_T - \chi_S}{1 + \omega^2\tau^2} \tag{20}$$

$$\chi'' = (\omega\tau) \cdot \frac{\chi_T - \chi_S}{1 + \omega^2\tau^2} \tag{21}$$

While the imaginary part of the susceptibility goes to zero for the limits $\omega \to 0$ and $\omega \to \infty$ it reaches a maximum for the the condition

$$\omega\tau = 1, \tag{22}$$

and allows a direct determination of the relaxation time.

2.6. Chemical Vapor Deposition and Molecular Beam Epitaxy

In order to grow monolayers or submonolayers of adsorbate structures various approaches are possible. In this thesis we applied two methods: *Chemical Vapor Deposition* (CVD) in order to grow the monoatomically thin *hexagonal boron nitride* (h-BN) layers and *Molecular Beam Epitaxy* (MBE) to deposit the C_{80} endofullerenes.

CVD

In order to grow h-BN on transition metal surfaces it is often an advantage to first obtain a cleaned and flat surface to reduce the number of domains and defects. This is usually obtained by several cleaning cycles using Ar^+ ion bombardment, oxygen deposition and annealing - while the detailed parameters may vary depending on the substrate. To grow the h-BN layer by CVD borazine ($(HBNH)_3$) is used as a precursor (Figure 9a). Under standard conditions borazine is a liquid with high vapor pressure and due to it's sensitivity to temperatures above 40° C and the high reactivity on metal surfaces, stored outside the vacuum in a cooled glass container.

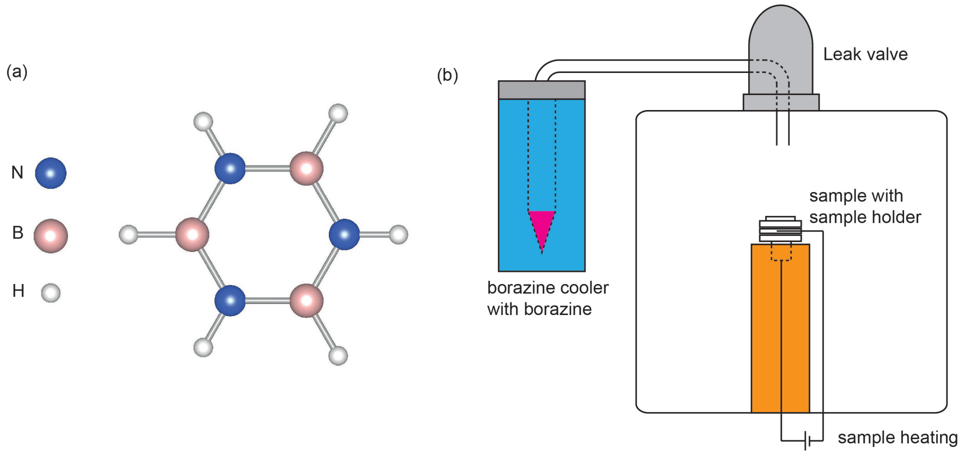

Figure 9: Borazine as a precursor: (a) Sketch of the $(HBNH)_3$ molecule; (b) Sketch of the preparation setup for CVD: The $(HBNH)_3$ molecule inside a cooling system can be admitted into the UHV chamber using a leak valve and focused onto the hot sample through a nozzle.

For growth of h-BN the borazine is directed over a leak valve into the UHV system, using a nozzle, and focused onto the hot sample surface as sketched in Figure 9b. While

h-BN growth on transition metals at pressures below $p = 10^{-3}$ mbar is a self-terminating process the exact growth conditions like pressure, sample temperature, time and pressure increment rate can vary a lot depending on the substrate.
The hot surface of the substrate acts as a catalyst, the $(HBNH)_3$ molecules decompose and the Nitrogen and Boron rearrange in *h*-BN layer. The alignment usually follows the substrate and may, for three-dimensional corrugated structures, match the lattice mismatch like in the case of *h*-BN/Rh(111) [13], *h*-BN/Ru(0001) [16] or *h*-BN/PtRh(111) [45] as discussed in Chapter 5.
Quality check of the *h*-BN layer usually is done performing measurements such as LEED (quality of the ordered lattice), UPS (detection/splitting of the σ- and π-bands), XPS (stoichiometry to determine the coverage) and STM (domain sizes, defects and alignment).

MBE

To deposit (sub)monolayers of molecules on surfaces the *LOw Temperature Nanogramm Evaporator* (LoTNE) [50] was used which allows the usage of tiny molecular amounts due to crucible-sample distance in the regime of 0.1 to 1 cm. The crucible is a modified *Knudsen* cell made of copper as sketched in Figure 11.

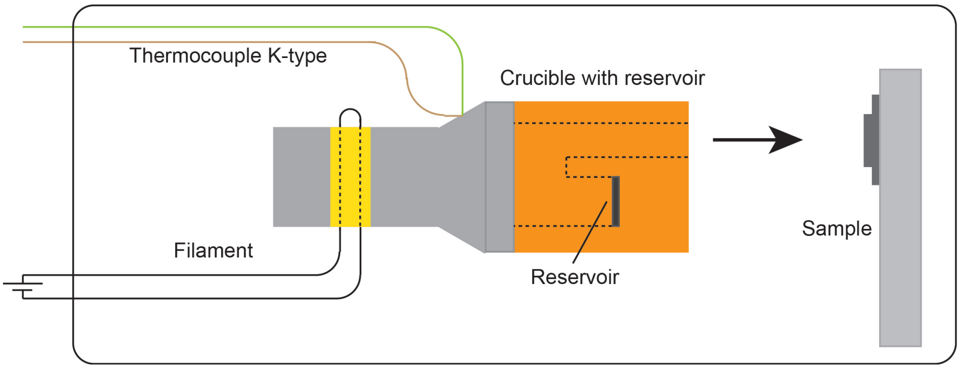

Figure 10: Schematic view of the MBE setup: a crucible with a reservoir for molecules is heated up to enable the molecular beam targeted at the sample surface. Temperature control is realized by thermocouples.

The *Knudsen* cell has a reservoir that can be filled by dropcasting in toluene (C_7H_8) dissolved molecules. After evaporation of the toluene only molecules remain and during baking and degassing procedures of the evaporator remaining toluene contaminations evaporate. The crucible can be heated using a one-sling filament in a ceramic of the crucible socket while temperature control is possible due to a K-type thermocouple point welded to the socket.
The short distances between crucible opening and sample surface ($d \approx 1$ cm) allow an optimized setup to minimize the amount of used molecules and contaminations on the sample from the evaporator. For the case of C_{80} temperatures around $T = 800$ K

turned tout to be optimized for a continuous beam of molecules directed on the sample surface. For other systems lower energies may be required depending on the stability of the molecules.
The amount, alignment and purity of deposited molecules then can be characterized using the same methods as discussed for the CVD section.
In order to obtain optimal growth conditions the temperature of the substrate surface may be controlled (LEED measurements to show the difference in structural ordering are shown in Appendix B.

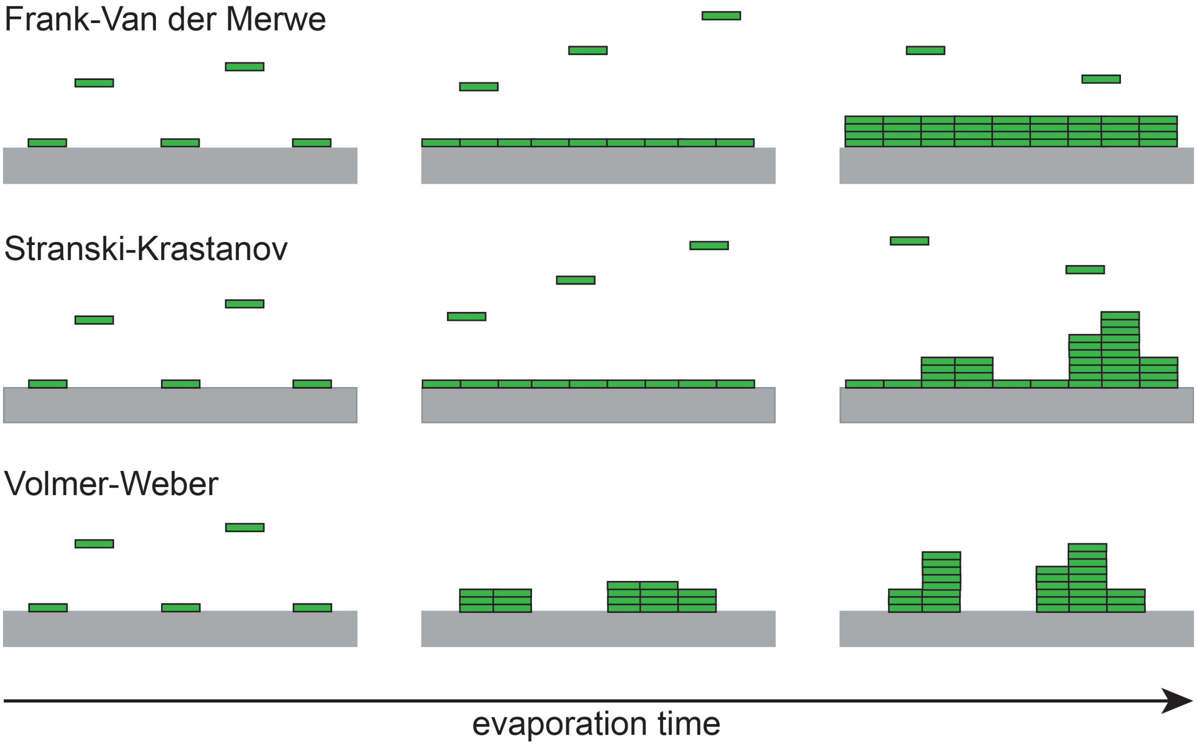

Figure 11: Sketch of the three different growth modes on substrates during MBE: Frank-Van der Merwe [51], Stranski-Krastanov [52] and Volmer-Weber [53].

Molecules tend to form systems of minimized free energy and thus follow surface tensions which may favor the growth in 3-dimension clusters (Volmer-Weber) instead of the formation of a filled monolayer. The potential barrier required to overcome in order to relax can vary a lot depending on the system. An increased sample temperature can help to overcome the energy barrier and support the growth type towards Stranski-Krastanov or Frank-Van der Merwe-type if the molecules obtain the activation energy to have enough mobility to disassemble the clusters and form single-molecule domains that merge at continuous evaporation time. One limitation of this option is the reactivity of the substrate with the molecules or, depending on the type of molecule, the energetic most favorable conformation might be clustering or desorption.

3. Laboratories

The data within the framework of this thesis was taken at several machines: The ESCA-, STM- and SQUID-laboratory of the Physics-Institute of the University of Zurich in addition to the PEARL, Material-Science and X-treme beamlines of the Swiss Light Source (SLS) synchrotron of the Paul Scherrer Institute. Though the major part of measurements focus on only two of those: The ESCA laboratory of the UZH and the PEARL beamline. Thus in the following only those will be covered.

3.1. ESCA laboratory of the University of Zurich

The ESCA laboratory of the University of Zurich is a five-chamber vacuum system with four VAT-valve controlled separable single-chambers at a base pressure of about $p = 2 \cdot 10^{-10}$ mbar. Heart of the machine is the Analysis chamber with a modified VG ESCALAB 220 photoemission spectrometer [54]. The Analyzer is a 6-channeltron based electron analyzer which enables to measure at 6 different electron energies simultaneously. This allows to setup a linear background subtraction for X-ray Photoelectron Diffraction measurements. In addition an Osterwalder-Type manipulator supports high resolution control of polar and azimuthal angle for hemispherical scans.

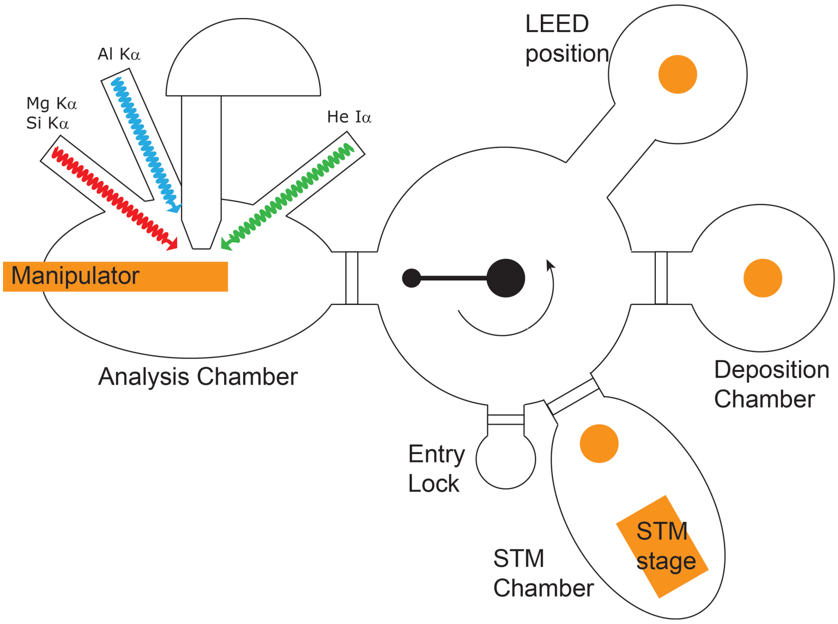

Figure 12: Schematic view of the ESCA vacuum system: Five chambers for different analysis methods and sample treatment are connected by a positioning chamber housing a 2π-rotational arm.

For chemical analysis five different light sources are available. A non-monochromatic twin anode housing a Mg Kα and a Si Kα source at $h\nu = 1253.6$ eV and $h\nu = 1740.0$ eV.

The high flux of the Mg Kα is optimal for measurements which require high signal to background ratio and thus often is used for XPD measurements. For high energy resolution measurements a monochromated Al Kα source is mounted with a photon energy of $h\nu = 1486.3$ eV to allow the resolution of surface core level shifts and to distinguish convoluted elastic lines. For the study of electronic properties a klystron-based helium discharge lamp with a silicon (Si) crystal monochromator which allows to select He Iα ($h\nu = 21.22$ eV) and He IIα ($h\nu = 40.8$ eV) radiation. To complete the excitation methods there are options for Ion beam scattering, electron loss spectroscopy and several viewports to introduce a laser source in order to study 2-photon photoelectron processes. A deposition chamber is dedicated to sample cleaning and therefore gives the options of sputtering, annealing and O_2 dosing. In addition there are several evaporator mounting ports. Highly reproducible temperature read out is possible using mantle thermocouples K-type (introduced into the sample holder) and a two-wavelengths Maurer pyrometer. *In-situ* relative work function measurements are possible using a Xe flash lamp [55] allowing precise control of growth for Frank-Van der Merwe growth type adsorbates and self-terminating mono layers in addition to a Pfeiffer Quadstar quadrupole mass spectrometer.

The vacuum system is completed by a transfer hub with a fast entry lock to allow sample transfer between all chambers without breaking the vacuum, a LEED chamber (directly connected to the positioning chamber) and a vibration-insulated STM chamber housing a Park Scientific Instruments VPII STM [56].

3.2. PEARL beamline at the swiss light source

The *Photo-Emission and Atomic Resolution Laboratory* (PEARL) is located at the X03-DA position of the Swiss Light Source synchrotron. It is installed at a 1.4 T bending magnet and supports a beam energy of 60 eV $< h\nu <$ 2000 eV. Monochromatic light is created using a plane-grating monochromator [57] with two different gratings (by choice 600 or 1200 lines/mm). The double-toroidal mirror allows a focused beam size of $A = 70 \times 190\ \mu\text{m}^2$ and can be defocused to $A = 1100 \times 1300\ \mu\text{m}^2$ at a maximum flux of $2 \cdot 10^{11}$ photons/s at a photon energy of $h\nu = 800$ eV and a resolution of $E/\Delta E = 7000$. The optical details were discussed by Oberta, *et. al.* [58].

The endstation is a 5-chamber UHV system similar to the discussed ESCA setup. The x-rays are lead into the X-ray Analysis chamber (XA) onto the sample. Sample manipulation in the XA is done using an in-house built *Complete Angle Resolved Variation for electron spectroscopy IN VilliGen* (CARVING) manipulator with 6 degrees of freedom: 3 translation movements (x, y and z direction) and 3 rotational movements in polar (θ), azimuthal (ϕ) and tilt (τ) direction with respect to the analyzer position. In addition controlled cooling down to $T \approx 30$ K is supported.

The photoelectrons excited by synchrotron radiation are detected in a hemispherical 2D analyzer (Omicron EW4000) as briefly presented in Chapter 4 and supports in this setup XPS measurements (including resonant XPS to increase the cross section), XPD, XAS and ARPES.

Sample preparation can be performed in two different preparation chambers (*X-ray*

Prepration chamber (XP) and *STM Preparation chamber* (SP)) both giving the option for annealing, sputtering and O_2 dosing. Both chambers also have the option to cool samples but only the XP chamber can reach temperatures below $T < 50$ K using a dedicated cooling stage. Sample preparation in XP is also supported with a mass spectrometer, an Auger LEED and a setup for *in-situ* measurements for relative work function changes. The CVD and MBE preparations used and discussed in Chapter 4 were all performed in the XP chamber.

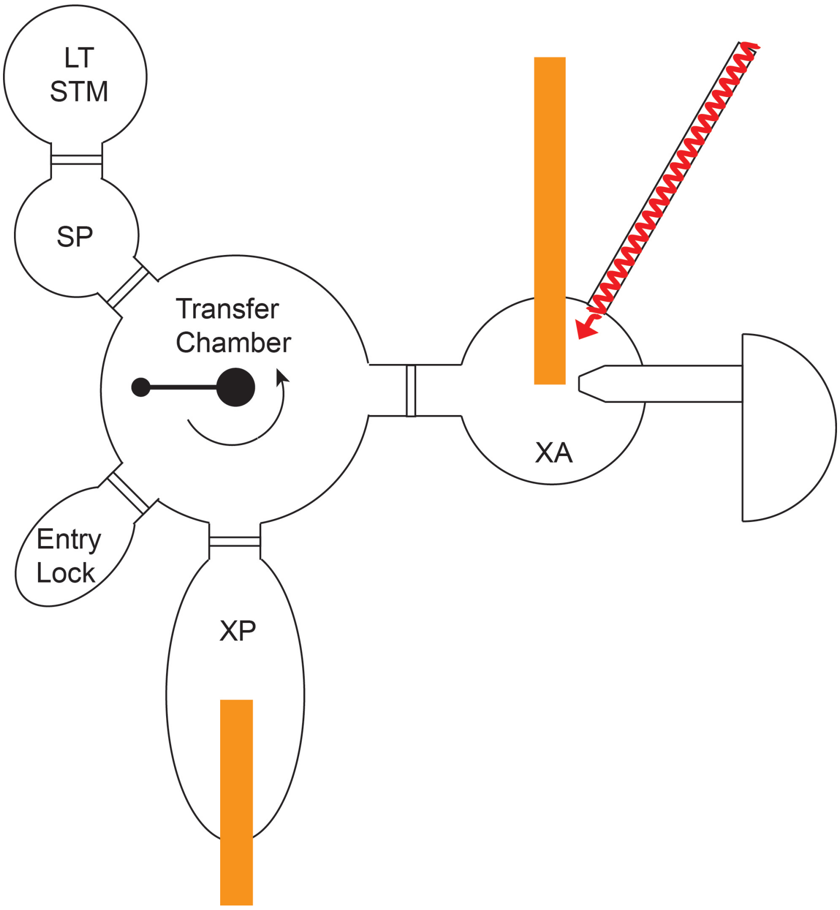

Figure 13: Schematic view of the PEARL vacuum system: Six chambers for different analysis methods and sample treatment are connected by a transfer chamber housing a 2π-rotational arm

As a surface investigation method complementary to XPD an Omicron low temperature STM is connected to the UHV system with active and passive dampening to support minimal vibrations as well as a fast entry lock to insert samples without breaking the vacuum.

4. XPD measurements using a hemispherical 2D electron analyzer EW4000

The 2D analyzer Scienta EW4000 installed at the PEARL beamline at the swiss light source is a hemispherical electron analyzer with a 200 mm mean radius using a 40 mm Micro-Channel Plate (MCP) detector monitored by a FireWire (IEEE 1394) Charge-Coupled Device (CCD)-camera with an acceptance angle $\alpha = 60°$ [59]. Compared to the older generation of channeltron analyzers (as for example installed in the ESCA laboratory of the University of Zurich) this acceptance angle enables to scan simultaneous different emission angles.At the present set up of PEARL the angle dispersion slit is parallel to the polar rotation axis of the CARVING manipulator.

At the PEARL beamline XPDs are measured in dependence of polar and azimuthal manipulator settings - in our case for one fixed azimuthal angle-setting each polar angle was measured before continuing at a different azimuthal angle, resulting in "azimuthal slices" over the hemisphere [60]. In this chapter we will give a brief introduction about transforming such XPD measurements to standard stereographic projections for further analysis (as done in Chapter 6).

While there are different approaches (including background subtractions and fitting procedures) here we will focus on one example to outline the technical details.

Fixed scan mode

The EW4000 analyzer has two different scan mode settings: *Swept mode* and *Fixed mode*. For the case of the *Swept mode* for each single manipulator setting in polar angle θ, azimuthal angle ϕ and tilt τ a spectrum is taken by scanning the energy range over the entire 2D detector area width and integrating over the sum of all channels. While step width and energy increment for the scanned area ΔE_{kin} is free of choice, a limiting factor is the optimization of statistical accuracy in dependence of measurement time.

The *Fixed mode* only allows an energy window depending on the set pass energy (energy range $\Delta E \approx \frac{E_{Pass}}{10}$). The maximum number of energy channels is limited by the CCD camera (in our case 992 channels in along the energy axis) but artifacts due to analyzer geometry, transmission function and detector efficiency variation [59] may occur. In the following we will focus on *Fixed mode* which also was used to measure X-ray Photoelectron Diffraction (XPD) patterns as shown in Chapter 6.

Raw data

We will document the procedure at the example of the N1s elastic line of h-BN/Ni(111). The current measurement geometry (as shown in Figure 15) causes an intrinsic effect on the transmission along the acceptence angle α which needs to be taken in account.

Figure 14b shows a single analyzer window of the N1s elastic line taken for one angular manipulator setting. The horizontal profile along the kinetic energy axis was averaged over an acceptance angle $-17° \leq \alpha \leq 17°$, as indicated with the red dashed lines in Figure 14b. This results in a typical XPS spectrum for the selected energy range. A parabolic background is visible over the entire spectrum originating from a weaker electron transmission at higher angles along the energy scale due to geometric reasons and a variation in detector efficiency [59].

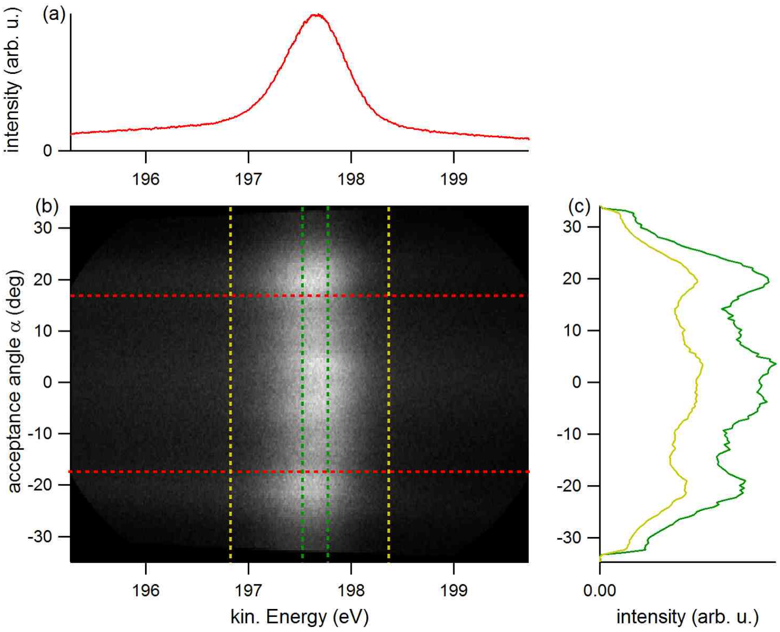

Figure 14: Fixed mode measurement for one angle setting of the manipulator: (b) shows the two dimensional detector frame (carpet) as recorded by the CCD camera; (a) horizontal average along the kinetic energy axis as indicated by the red dashed lines; (c) vertical averages along the acceptance angle α axis for two different areas (green, light green).

The profiles along the acceptance angle α (Figure 14c) reveal a pronounced non constant angular transmission, since the manipulator is set to a set of angles where no angular dependence should occur around $\alpha = \pm 20^\circ$ originating from the analyzer transmission function. Comparing two different energy profiles (averaging over a different width of the energy window as indicated with green and light green dashed lines in Figure 14b) reveals the same profile structure. The scaling depends on the different areas and the average intensities for a given energy.

For the typical XPD measurement taken for this thesis and as shown in Chapter 6, analyzer windows (as shown in 14a) are taken for 10 different azimuthal settings (in steps $\Delta\phi = 36^\circ$) in order to avoid the azimuthal slices to be a multiples of the crystal symmetry (in our case 3), and 45 polar angles (in steps of $\Delta\theta = 2^\circ$) - totaling up to a stack of 450 detector frames. With those settings the entire hemisphere above the sample is measured up to a polar angle of $\theta = 88^\circ$ as indicated in Figure 15.

Energy dependent background

In order to remove the background of the single spectra (for each acceptance angle α and manipulator setting θ, τ and ϕ) with a polynomial of second order. To ensure the measured signal (for example the elastic line) is not influenced we introduced a weighting function

$$f(E,\theta,\phi,\alpha) = \begin{cases} 0 & \text{, elastic line contributes to the signal} \\ 1 & \text{, background} \end{cases} , \qquad (23)$$

as indicated in Figure 16 with the blue line. After the fitted background is subtracted from the signal only the elastic line remains.

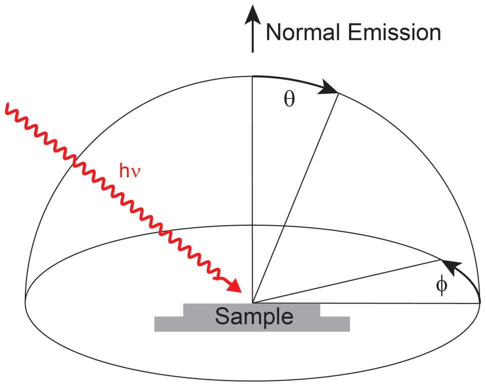

Figure 15: Geometry of the measurement setup: The horizontal polarized x-rays are at an incidence angle of 60° with respect to normal emission; polar angle θ and azimuthal angle ϕ are indicated with respect to the sample surface and normal emission angle $\theta = 0°$.

For more complex signals like convoluted signal structures, direct fitting functions including the parabolic background can be applied in order to obtain the intensities of the single components.

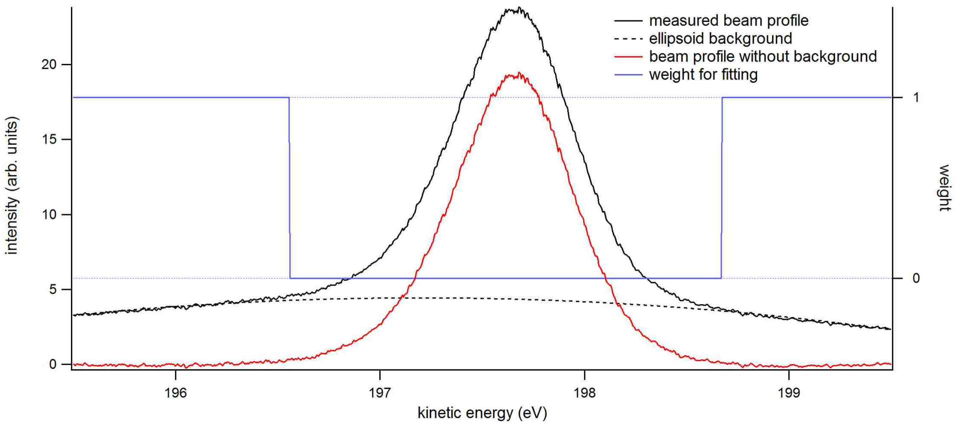

Figure 16: Removal of a parabolic background: The profile along the kinetic energy axis (black) was fitted using a weighting function (blue); red: background subtracted spectrum.

Intensity map

After background subtraction to obtain the intensities as a function of angular distribution and kinetic energy, integration along the energy axis results in the total counts of the signal as a function of the angular manipulator settings $I = I(\alpha, \theta, \phi)$.
Figure 17a shows all integrated values in a grid of acceptance angle α and 45 polar angles θ (from top to bottom) in blocks for all the ten azimuthal angle-settings ϕ. Scattering effects of the h-BN layer are already visible, though artifacts, as an influence of the transmission function along both, acceptance angle α and polar angle θ, are present and can dominate if the signal has a low anisotropy.
To visualize the artifacts caused by the analyzer transmission function consider Figure 17b which shows an excerpt of Figure 17a for $\phi = -165°$. A strong influence of the transmission function is visible along the acceptance angle α, as visualized by five horizontal profiles in Figure 17d: At $\alpha = \pm 20°$ and $\alpha = 0°$ an increased intensity is measured (as already observed in a single analyzer window and shown in Figure 14). A strong influence is visible especially for lower polar angles θ. Comparison of the cuts for different polar angles shows a non-linear behavior along the polar angle θ. The transmission function appears to be dependent on both angular directions: $T = T(\alpha, \theta)$, and also, the polar dependence does not show a typical distribution as (Figure 17c) that would be expected for an intensity distribution basing on emission angle influence since it doesn't follow the $\cos^2(\theta)$-rule.

Removal of the transmission function

To remove the transmission function $T = T(\alpha, \theta)$ and thereby the induced artifacts we first have to determine T in order to correct the raw data. We assume that averaging over all azimuthal angles results in a profile map that bases on all θ- and α-dependent transmission function influences. Since the average of all angles would correspond in the ideal case to the transmission function of a polycrystalline sample, no scattering effects of a crystalline structure should be visible, given the case that the number of azimuthal angle settings is not a multiple of the sample symmetry.

To remove the transmission function background from the intensity map we divide each point by the sum of all intensities with the same polar and acceptance coordinates as following

$$I_{NORM}(\alpha, \theta, \phi) = \frac{I_{Experiment}(\alpha, \theta, \phi)}{\sum\limits_{i=0}^{N} I_{Experiment}(\alpha, \theta, i)}, \tag{24}$$

where N is the number of azimuthal settings taken.

The normalization map (i.e. the sum at the denominator of Equation 24) is shown in Figure 18e. To further remove artifacts from the MCP edge and low statistics at the outermost acceptance angles the intensity map was reduced to $-25° \leq \alpha \leq +25°$.

The strong influence of the transmission function along both angular directions is well visible in Figure 18e. After normalization of the intensity map (Figure 17a) the acceptance angle and polar angle influence of the transmission function is clearly reduced as visible in Figure 18a for all polar and azimuthal angle setting and Figure 18b for the excerpt at an azimuthal angle manipulator setting of $\phi = -165°$, analogous to Figure 17.

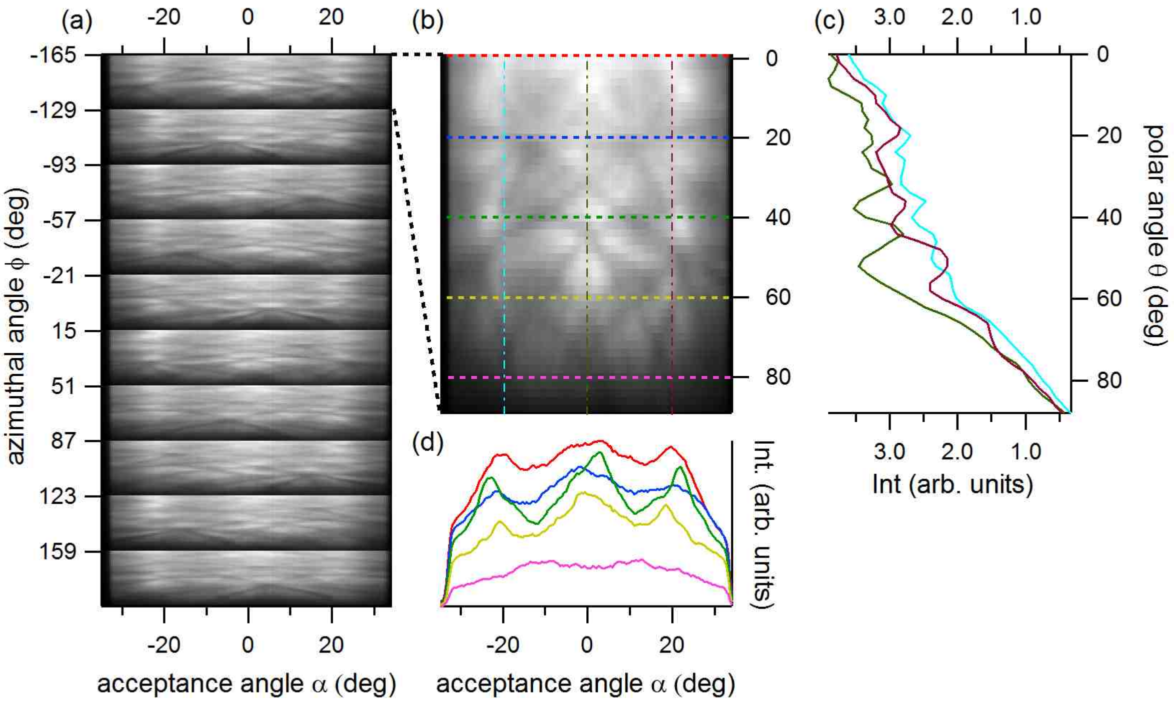

Figure 17: Intensity set after integration over the energy area: (a) all 450 intensity profiles along the acceptance angle α in sets of 45 polar angles θ for all 10 azimuthal angles; (b) intensity map for one azimuthal setting as except of (a) ($\phi = -165°$); (c) profiles along the polar angle θ of (b) for three different acceptance angles $\alpha = -20°, 0°, +20°$ in cyan, olive and purple, respectively, as indicated with the dash-dotted lines in (b); (d) profiles along the acceptance angle α in (b) at polar angle settings $\theta = 0°, 20°, 40°, 60°, 80°$ in red, blue, green, yellow and magenta, respectively, as indicated with the dashed lines in (b).

The scattering effects, which correspond a phi-average normalized intensity distribution, remain in the intensity map as demonstrated by cuts along the acceptance angle α and polar angle θ in Figure 18d and c, respectively. The profiles of the normalized intensity map (full lines) do not contain visible effects of the transmission function (plotted against left and top, respectively) compared to the unnormalized profiles (dashed lines).
As a drawback, the loss of forward scattering information along the normal emission direction at $\theta = 0°$, due the averaging over azimuthal distributions, has to be considered. Especially at lower polar angles ($\theta < 10°$) an increasing signal contribution may be lost as visible in Figure 18c.

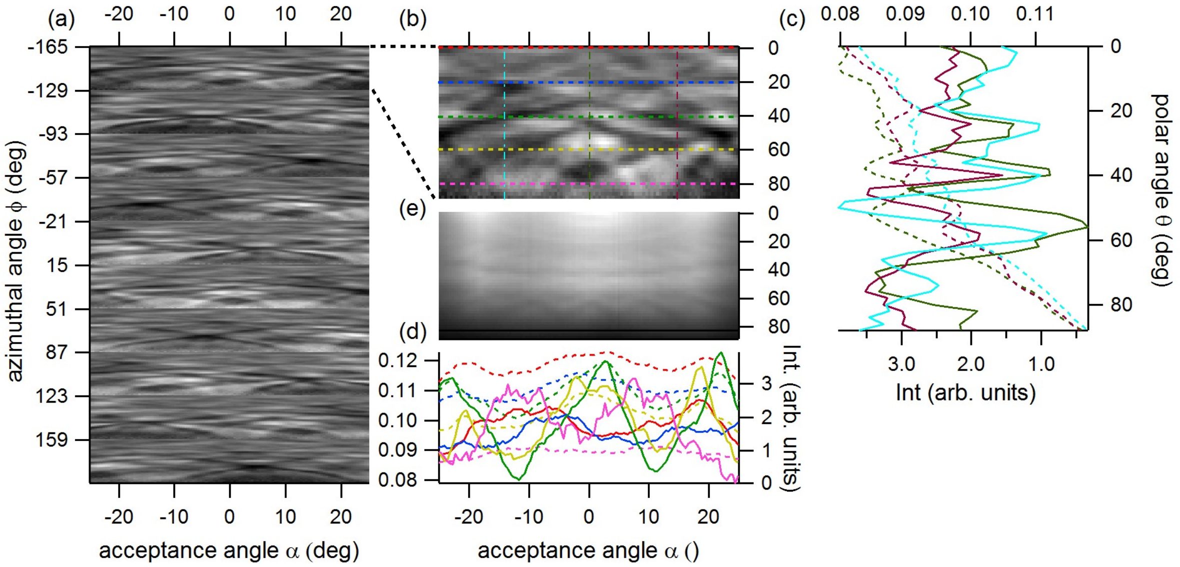

Figure 18: Data set after removal of the transmission function: (a) all 450 lines in sets of 45 polar angles θ for all 10 azimuthal angles settings; (b) polar angles for one excerpt for the case of $\phi = -165°$; (c) profiles along the polar axis of (b) for $\alpha = -20°, 0°, +20°$ in cyan, olive and purple, respectively, as indicated with the dash-dotted lines in (b) against top axis. In comparison the dotted lines in same color code for the case before removal of the transmission function (refer Figure 17d) against bottom axis; (d) profiles along the acceptance angle α in (b) with $\theta = 0°, 20°, 40°, 60°, 80°$ in red, blue, green, yellow and magenta, respectively, as indicated with the dashed lines in (b) against left axis, in comparison to the dotted lines (from Figure 17c) on the right axis; (e) normalization window as the sum over all polar angles ϕ.

Projection as stereographic map

As discussed before the common way to display XPD patterns are stereographic projections. Therefore a two step process is implemented. First the Cartesian detection coordinates are calculated basing on a coordinate transformation. Secondly the detection vectors are rotated according to the manipulator angles. This results in a standardized stereographic map of the XPD measurement as shown in Figure 19, which can be used for further structural analysis.

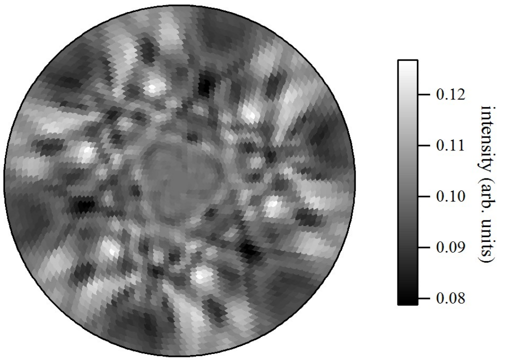

Figure 19: Projection of the N1s signal after mapping on a stereographic grid and 3-fold averaged.

5. h-BN/Pt$_{50}$Rh$_{50}$: A nanotemplate

5.1. Introduction

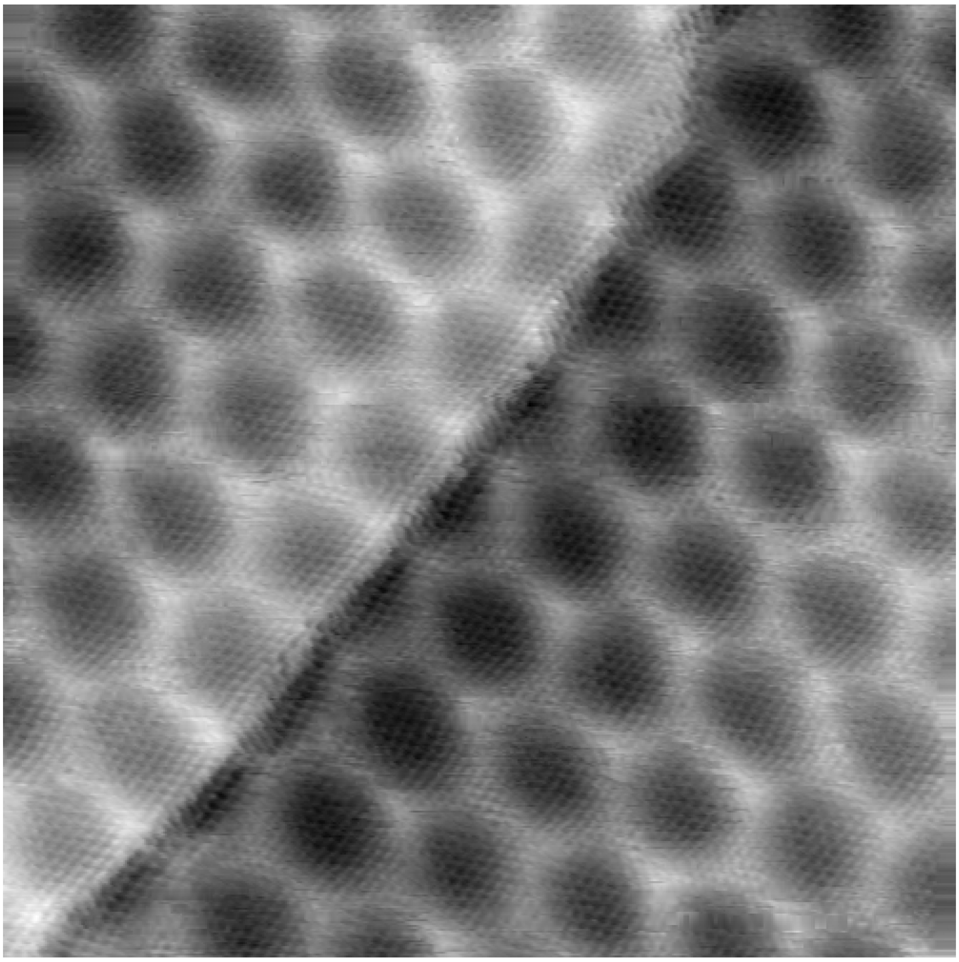

Figure 20: STM topographic image of h-BN/PtRh taken at room temperature - scan area $A = 10 \times 10$ nm^2, V$_B$ = 500 mV, I$_T$ = 1.5 nA; image contrast reversed.

This section covers the self-assembly of segregation profiles in a Pt$_{50}$Rh$_{50}$ single crystal, induced by the growth of hexagonal boron nitride (h-BN). The top layer of the substrate forms patches of Rh surrounded by Pt atoms, while this profile is inverted in the second layer of the substrate.

Since most of the data and conclusions are discussed rigorously in the publication *Self-assembly of nanoscale lateral segregation profiles* [45] here we will only present a more detailed version of the supplemental information followed by the publication itself.

Experimental

The experiments were performed in three different experimental chambers: (i) in the ESCA laboratory of the University of Zürich, housing a modified VG ESCALAB 220 photoelectron spectrometer [54] with a base pressure of 2×10^{-10} mbar as presented in Chapter 3.1. The photoemission experiments were done using a Mg Kα x-ray source (hν=1253.6 eV) for the XPS and XPD measurements, and a monochromatic Helium discharge lamp (hν=21.2 eV) for UPS and ARUPS.
The STM images were recorded with a variable temperature Omicron VT-STM in constant-current mode at room temperature, as described in [61]. Sample preparation for the STM investigations were performed *in-situ*.
The SXRD measurements took place at the Material Science beamline [62] of the Swiss Light Source of the Paul Scherrer Institute in Villigen, using a photon-beam energy of 10 keV at an incident angle of 0.39°. The base pressure during the measurements inside a Be-dome vacuum chamber was 10^{-9} mbar. Sample preparation and characterization was done in the ESCA laboratory of the University of Zurich - sample transfer was done using a *baby-chamber* transport setup to transfer the sample to the beamline without breaking the vacuum.
The PtRh(111) crystal was cut from an ingot with 47(±1) % Pt as determined by x-ray fluorescence analysis using standards [63].
The crystal was cleaned using standard cleaning procedures for Rh(111) [13] including Ar^+ bombardment and oxygen cleaning prior sputtering cycles. In addition annealing cycles up to T=1250 K [64] were performed.
The *h*-BN growth was done using chemical vapor deposition (CVD) dosing 150 L of borazine $(HBNH)_3$ at T=1225 K and a cooling rate of $\beta = -0.25$ K/s after 75 L. Preparation temperatures above 1150 K were required to obtain optimal growth conditions with a low domain rotation rate. The *h*-BN growth is well controlled and, at the given chemical vapor deposition (CVD) conditions, self terminating at one monolayer [65].

XPS Peak deconvolution

Figure 21 shows the four Mg Kα excited photoelectron spectra (as shown in Figure 1 of the publication) with the spin orbit split Rh $3d$ multiplet and the Pt $4d_{5/2}$ elastic line. The deconvolved components are shown in red for the Rh contribution and blue for the Pt contribution. In order to obtain the atomic composition within the probing depth of 1.25 nm for normal emission and 0.26 nm for grazing (θ=78 °) emission, the intensities have been normalized with atomic photoemission cross sections of 0.3210 Mb for Rh 3d and 0.1976 Mb for Pt $4d_{5/2}$, respectively [35]. The fitting procedure consisted out of 3 Doniach-Sunjic lineshapes [66] after Shirley background subtraction [67].
In order to minimize forward scattering influence on measured intensities, the grazing angle emission measurements were taken at $\theta = 78°$ at an azimuthal angle of 8° off $\langle 0\bar{1}1 \rangle$ towards the $\langle 001 \rangle$ diection where no forward scattering effects are expected for an fcc(111) lattice.

This results in Pt:Rh ratios for bare PtRh(111) of 59.8 : 40.2 for normal and 72.0 : 28.0 for grazing emission. For *h*-BN/PtRh(111) the corresponding ratios get 59.9 : 40.1 and 69.8 : 30.2 for normal and grazing emission, respectively.

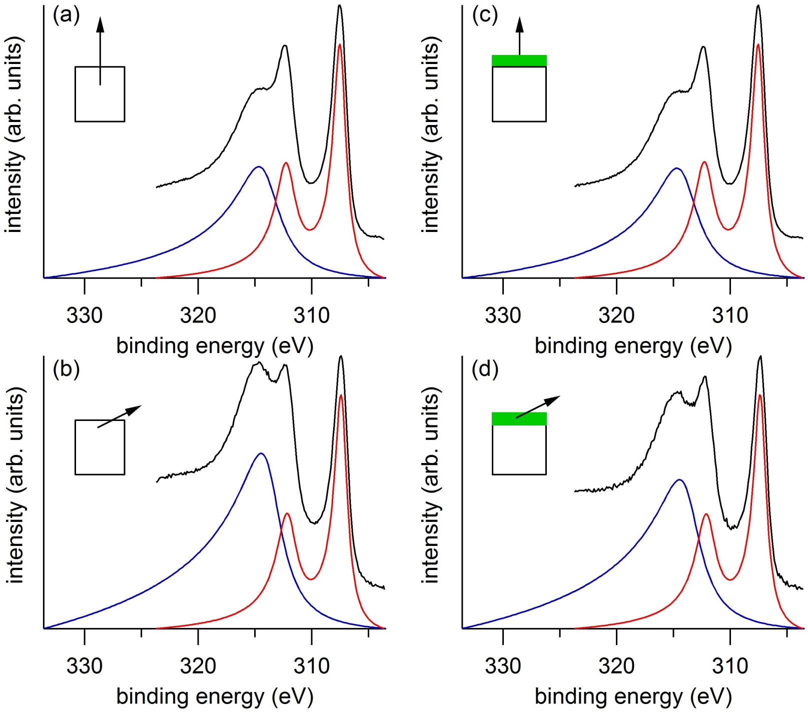

Figure 21: (Color online)Mg Kα excited Rh 3d and Pt 4d$_{5/2}$ x-ray photoelectron spectra of bare PtRh at (a) normal, (b) grazing and *h*-BN/PtRh at (c) normal and (d) grazing emission angles as shown in Figure 1 of the manuscript in black. The fits of the chemical components after Shirley background subtraction are offsetted for clarity (Pt 4d$_{5/2}$ in blue and Rh 3d in red).

ARUPS bandstructure

The bandstructure was investigated with ultraviolet photoelectron spectroscopy (ARUPS) using He $I\alpha$ excitation at an energy of $h\nu = 21.2$ eV, for both the bare PtRh(111) and for *h*-BN/PtRh(111). While in Figure 2 of the publication only the spectrum in the Γ point (normal emission) is shown the bandstructure was measured in ΓK and ΓM direction.

Figure 22 shows the ΓK direction for bare PtRh (left) and *h*-BN/PtRh (right). Here the normal emission PtRh band structure related feature at 3.9 eV binding energy has a dispersion distinct from that of the BN σ bands and can thus be easily discriminated. For the *h*-BN case both the π band (around $E_B = 8.1$ eV) and the σ bands with a splitting of $\Delta E \approx 0.9$ eV arise at the Γ point. The coincidence in binding energy between σ bands and the PtRh dispersion at $E_B = 3.9$ eV reduces the optic effect of the splitting.

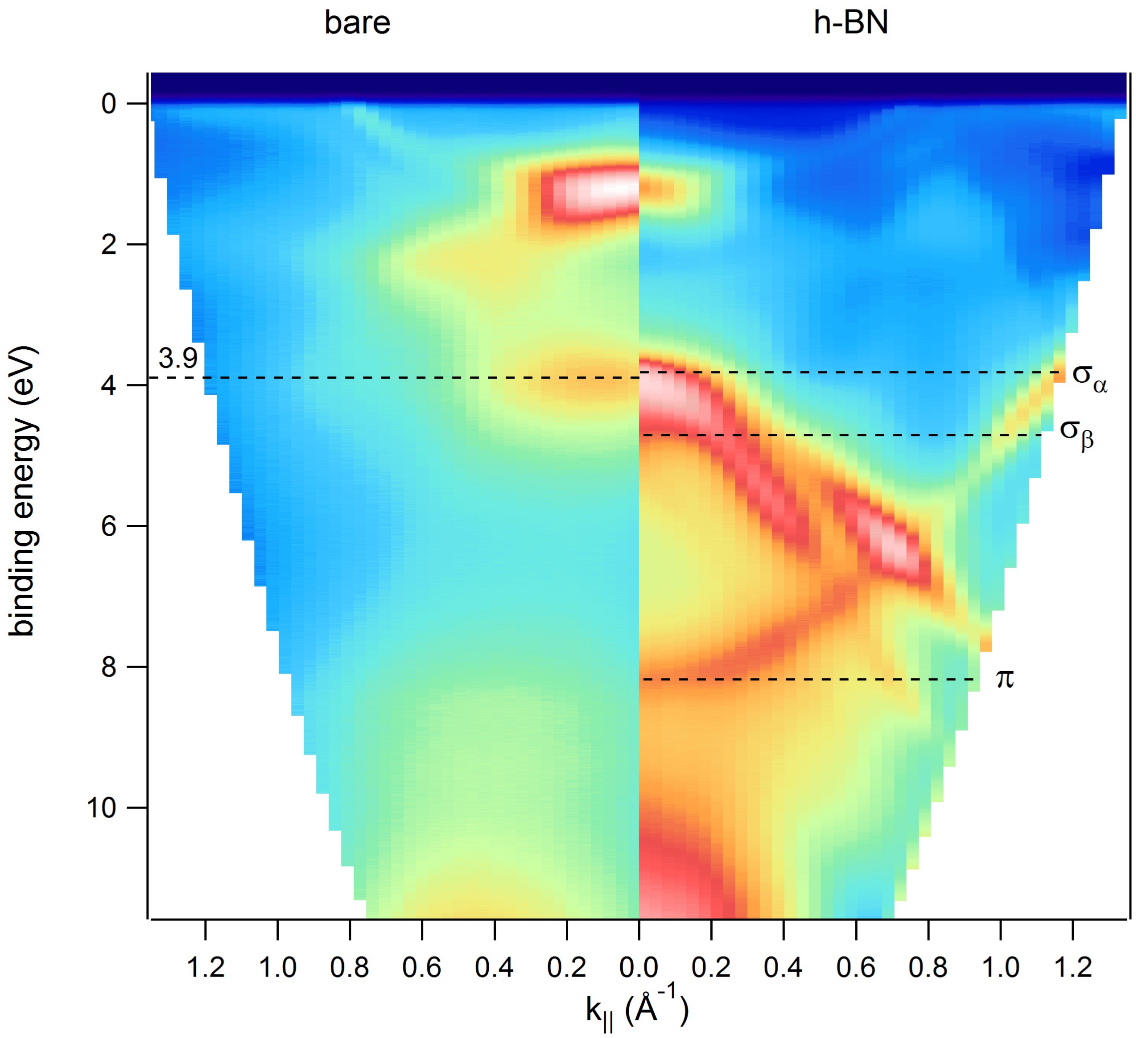

Figure 22: Angular resolved ultraviolet photoelectron spectroscopy (ARUPS) along the ΓK direction taken with a He discharge lamp at $h\nu = 21.2\ eV$. Left: bare PtRh, right: h-BN/PtRh. The dashed horizontal line in the bare PtRh panel indicates the position of the PtRh related state in comparison to the positions of the σ- and π-bands in the h-BN/PtRh panel.

Theory

Density Functional Theory (DFT) calculations were done in a collaboration with the *Hamburg University of Technology* in order to corroborate the experimental findings. The *ab initio* study combined DFT calculations by VASP [68, 69] with a cluster expansion [70] by UNCLE [71]. We used a PAW-PW91 [72–74] functional in order to be in line with our previous studies on PtRh [75–78]. For well-chosen structures, we had be-

forehand checked with a van-der-Waals (vdW) functional [79, 80] that vdW influence on the energetic hierarchy of the system can be neglected. Furthermore, the experimentally observed segregation is already in perfect accordance with our vdW-free approach.
For the calculations we used a lateral lattice constant of 0.2767 nm, corresponding closely to the experimentally determined values of PtRh.

VASP (Vienna *Ab initio* Simulation Package) input files

For the DFT calculations, we employed a $11 \times 11 \times 1$ Monkhorst-Pack [81] mesh for the Brillouin zone sampling. The plane wave basis cutoff has been set to 520 eV. In each unit cell the spatial positions of the 16 surface atoms as well as the z-positions of the 8 adsorbate atoms has been varied using a conjugate gradient algorithm until the forces on these unconstrained atoms were less than 5 meV/Å. We applied a dipole correction [82, 83] to compensate for the slab asymmetry and prevent undesired interaction of periodic images through the vacuum region, which in either case extends to at least 12 Å (a screenshot of the INCAR input file is shown in Figure 23).

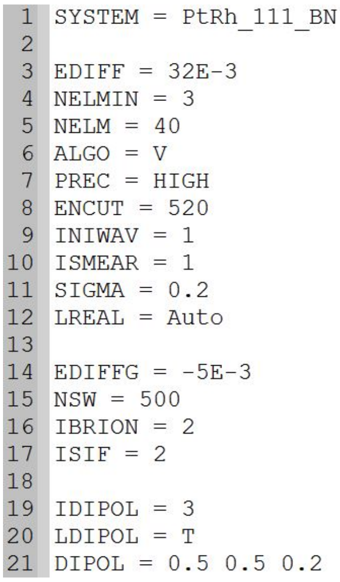

```
SYSTEM = PtRh_111_BN

EDIFF = 32E-3
NELMIN = 3
NELM = 40
ALGO = V
PREC = HIGH
ENCUT = 520
INIWAV = 1
ISMEAR = 1
SIGMA = 0.2
LREAL = Auto

EDIFFG = -5E-3
NSW = 500
IBRION = 2
ISIF = 2

IDIPOL = 3
LDIPOL = T
DIPOL = 0.5 0.5 0.2
```

Figure 23: Screenshot of the INCAR file.

XPD simulations

Figure 24 shows simulated x-ray photoelectron diffraction (XPD) stereographic maps of Rh fcc(111) using the 3d electrons at a kinetic energy of 939.8 eV as emitters. The simulations were done using the Electron Diffraction in Atomic Clusters (EDAC) code [44] with one emitter in each layer, (b) to (e) corresponding to layer 1 to 4. The sum of the four simulations result in Figure 24(a) and reflects the fcc(111) XPD patterns. Simulations for Pt result in the same patterns with slightly different peak widths and intensity ratios. Note the close resemblance of Figure 24(c) with the cross-ratio X in Figure 3(e) verifying the increase of Pt contribution in the second layer.

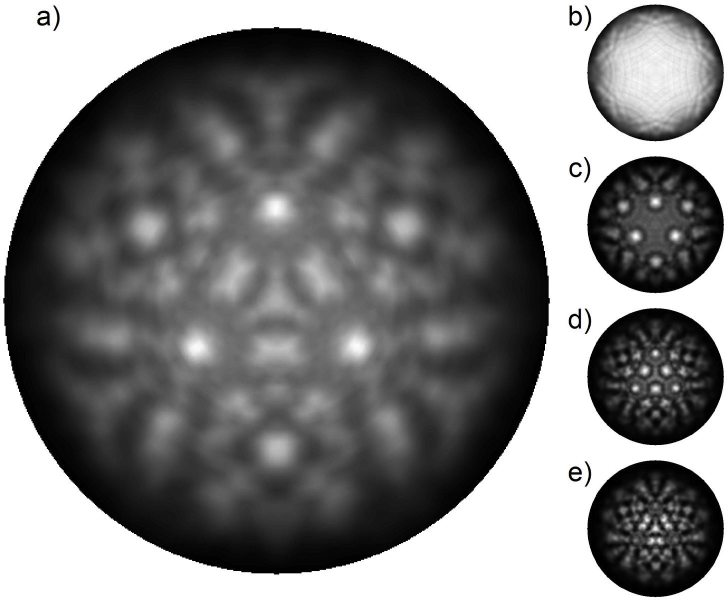

Figure 24: Simulation of the stereographic map of Rh(111) using the Electron Diffraction in Atomic Clusters (EDAC) code [44]. a) shows the sum of the single emitter calculations of the layers 1 to 4 being consistent with the experiment. b) to e) show the single emitter influence of the layers: b) top layer, c) 2nd layer, d) 3rd layer and e) 4th layer. Greyscale: White corresponds to the maximum intensity and black to zero intensity. Also shown in Section 2.2, Figure 6.

5.2. Self-assembly of nanoscale lateral segregation profiles

In the following publication the citations correspond to the citations [10–14, 16, 62, 64, 75–78, 84–97] in this thesis.

RAPID COMMUNICATIONS

PHYSICAL REVIEW B **93**, 161402(R) (2016)

Self-assembly of nanoscale lateral segregation profiles

R. Stania,[1,2,*] W. Heckel,[3] I. Kalichava,[2] C. Bernard,[1] T. C. Kerscher,[3] H. Y. Cun,[1] P. R. Willmott,[2] B. Schönfeld,[4]
J. Osterwalder,[1] S. Müller,[3] and T. Greber[1]
[1]*Physik-Institut, Universität Zürich, Winterthurerstrasse 190, 8057 Zürich, Switzerland*
[2]*Paul Scherrer Institut, 5232 Villigen PSI, Switzerland*
[3]*Hamburg University of Technology, Denickestraße 15, 21073 Hamburg, Germany*
[4]*Laboratory of Metal Physics and Technology, Department of Materials, ETH Zürich, 8093 Zürich, Switzerland*

(Received 27 November 2015; revised manuscript received 26 January 2016; published 7 April 2016)

The surface segregation profile of an intermetallic compound becomes vertically *and* laterally modulated upon epitaxial growth of a single-layer hexagonal boron nitride (h-BN) nanomesh. h-BN on PtRh(111) forms an 11-on-10 superhoneycomb, such as that on Rh(111) [Corso *et al.*, Science **303**, 217 (2004)], though with a smaller lattice constant of 2.73 nm. X-ray photoelectron diffraction shows that the h-BN layer reduces the Pt enrichment of the first layer by promoting site swapping of about 10 Pt-Rh pairs within the 10×10 unit cell between the first and second layers. This segregation profile is confirmed by density-functional-theory-based cluster-expansion calculations. Generally, a strong modulation of the h-BN bonding strength and a higher affinity to one of the constituents leads to self-assembly of top layer patches underneath the nanomesh pores.

DOI: 10.1103/PhysRevB.93.161402

Surface segregation is an important process in intermetallic compounds [1]. The surface enrichment of a certain atomic species has many practical applications, as in hydrogen storage [2] or nanocatalysis [3]. The deviation from the bulk composition is driven by strain release and different surface energies of the constituent elements [4]. Today's computational power may tackle the problem of surface segregation and ordering of alloy surfaces in the presence of adsorbates by a concerted effort of *ab initio* density functional theory, cluster expansion, and Monte Carlo simulations [5]. For PtRh, comparisons to experiments [6] show excellent agreement [7] and phenomena like carbon-induced segregation can be understood [8].

Lateral segregation on the micrometer scale was observed in heterogeneous catalysis in artificial heterostructures [9]. Here we report on lateral segregation profiles in the top layers of PtRh(111) on the nanometer scale. They are created during the growth of a single layer of hexagonal boron nitride (h-BN), which imposes the formation of a superhoneycomb "nanomesh." We show that the site- *and* species-selective interaction of the overlayer strongly affects the segregation profiles, both vertically *and* laterally.

h-BN grown on Rh(111) forms a corrugated monolayer with a 13-on-12 superhoneycomb structure known as the h-BN nanomesh [10,11]. In contrast, h-BN on Pt(111) forms a flat layer with an approximate 10-on-9 superstructure, due to weaker and less selective bonding than in the h-BN/Rh(111) nanomesh [12,13]. The growth of h-BN on PtRh(111) produces as well a nanomeshlike superstructure. Segregation distinct from the bare surface occurs in the topmost layers of the substrate during growth of h-BN, and Rh atoms form patches under the pores of the nanomesh, which are surrounded by Pt atoms underneath the wires. This overlayer-assisted segregation signifies a new tool for self-assembly in intermetallic compounds and has potential impact in intercalation chemistry [14–16], the production of nanometer-sized holes in h-BN [17], or in the formation of new magnetic structures, to name three potential applications. Experimental and calculating details are described in the Supplemental Material [18].

Figure 1 shows x-ray photoemission spectra (XPS) of the Rh $3d$ and the Pt $4d_{5/2}$ peaks from annealed PtRh and single-layer h-BN on PtRh(111). The platinum surface segregation can be directly seen by comparing normal and grazing emission spectra for both systems: The Pt:Rh ratio increases in going from normal ($\theta = 0^\circ$) to grazing ($\theta = 78^\circ$) emission. For grazing emission we chose an azimuthal emission angle away from any forward-scattering peaks. From the mean free path in PtRh at the given electron kinetic energy, the probing depths are 1.25 and 0.26 nm, respectively. The h-BN layer attenuates the photoelectron emission; however, this does not affect the observed Pt:Rh ratio, because the relative kinetic energy difference between the peaks in Fig. 1 is less than 1%.

From a comparison of the grazing emission spectra of bare and h-BN covered PtRh [Figs. 1(b) and 1(d)] it is seen that in the latter case the Pt:Rh ratio decreases, which indicates, given the small probing depth, Rh segregation to the top layer. If the peak areas are evaluated and normalized with the corresponding photoemission cross sections, the atomic concentrations for the given probing depth can be determined [18]. The four pie diagrams in Fig. 1 show that all spectra indicate excess of Pt with respect to the bulk stoichiometry. The Pt content is largest for the grazing spectrum of bare PtRh [Fig. 1(b)].

For a complete picture of the influence of h-BN on segregation, as suggested by the XPS data in Fig. 1, the structure has been studied with four more surface-science techniques. It was thereby found that the h-BN forms a commensurate superhoneycomb (nanomesh) structure, similar to the case of Rh(111) [11], but not to that of Pt(111) [12,37,38]. In addition, it induces Rh enrichment in the top layer. Figure 2(a) displays low-energy electron-diffraction data of h-BN/PtRh, where a perfect, highly ordered superstructure that is aligned to the substrate is observed. The superstructure dimensions are quantified using surface x-ray diffraction [39]. First, the unit cell size of the bimetallic bulk crystal was determined to be

---

[*] Corresponding author: rostania@physik.uzh.ch

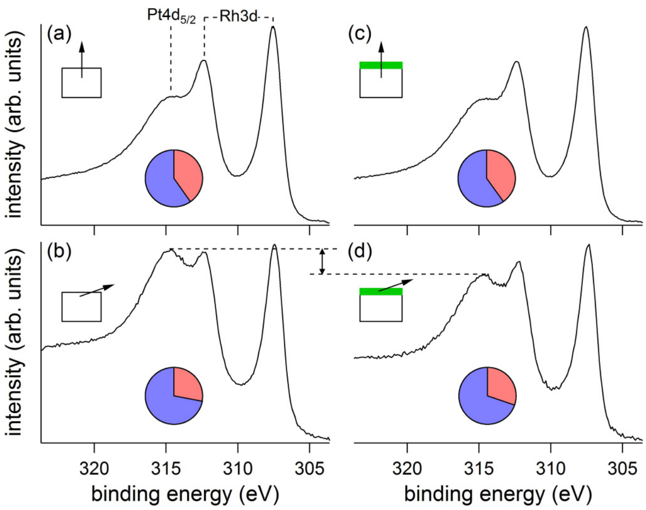

FIG. 1. Mg Kα excited Rh $3d$ and Pt $4d_{5/2}$ x-ray photoelectron spectra of bare PtRh at (a) normal, (b) grazing and h-BN/PtRh at (c) normal and (d) grazing emission angles. The spectra are normalized to the Rh $3d_{5/2}$ intensity. The relative increase of the Pt $4d_{5/2}$ signal at 315 eV in going from normal to grazing emission indicates Pt surface segregation. The decrease of the grazing Pt signal for h-BN/PtRh indicates h-BN-induced Rh segregation to the top layer. The pie diagrams represent the Pt (blue) and the Rh (red) atomic concentrations for the respective probing depths.

within 0.1% of that expected from Vegard's law for a 50:50 atomic mixture. Figure 2(b) shows an in-plane diffraction scan in units of the PtRh surface lattice (h,k,l), at $l = 1.2$ and $k = 0$, and along h. In addition to the bulk crystal truncation rod at $h = 1$, the superstructure signal is seen at $h = 9/10$ and $11/10$. The superstructure unit cell thus consists of (11×11) h-BN units on top of (10×10) PtRh units, with a superlattice constant of 2.729 ± 0.001 nm. The $\frac{11}{10}$ rod mainly reflects scattering off the BN lattice and would also be expected for noninteracting h-BN. The presence of the $\frac{9}{10}$ rod, however, proves commensurability and a periodic strain between PtRh and h-BN [40]. Therefore, the lattice mismatch between the two (1×1) unit cells of -8.4% is relaxed by the superstructure to $+0.8\%$, which indicates that the h-BN in the 10×10 structure undergoes weak compressive strain, as is the case for h-BN/Rh(111).

The electronic structure of h-BN/PtRh(111) shows a σ band splitting, as also observed for the h-BN/Rh(111) nanomesh [10,11]. In Fig. 2(c) normal emission He Iα spectra for bare PtRh(111) and h-BN/PtRh(111) are shown. For h-BN/PtRh(111) the spectrum is dominated by the σ band that appears split by 0.9 eV into σ_α and σ_β components. The σ band features coincide with the PtRh band structure related feature at 3.9 eV binding energy that has, however, a distinct dispersion [18]. The σ band splitting is a strong indication of the formation of a nanomesh structure with two distinct electronic regions defined by the wires and pores [11]. A further influence of the h-BN overlayer on the surface electronic structure is observed in the photoemission intensity at the Fermi level. The spectral density increases upon h-BN layer growth. Since h-BN has no states at the Fermi level, this must be due to changes in the top layer of the PtRh.

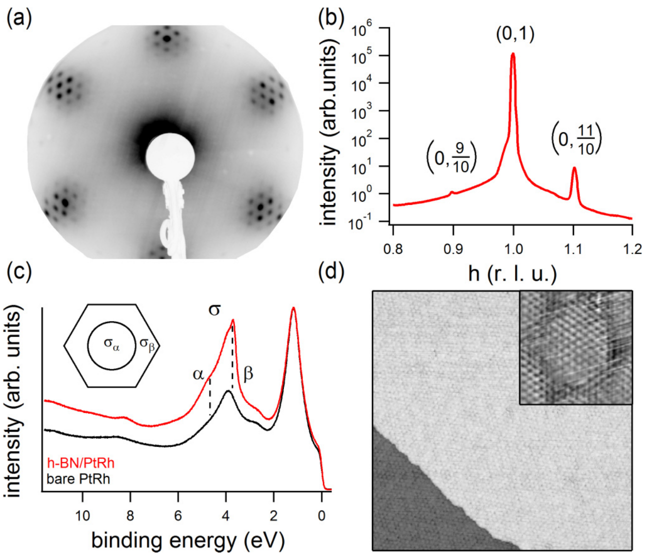

FIG. 2. Identification of the nanomesh superstructure of h-BN/PtRh(111). (a) Low-energy electron diffraction (LEED) pattern ($E = 70$ eV). The 1×1 PtRh(111) principal spots are surrounded by h-BN-induced superstructure spots. (b) Surface x-ray diffraction (SXRD) along the h direction showing the crystal truncation rod and h-BN-derived $11/10$ and $9/10$ superstructure rods. (c) Normal emission angular resolved He Iα spectra for bare PtRh (black) and h-BN/PtRh(111) (red). The spectra are normalized to the intensity of the valence band peak at $\sim$1 eV. The dashed lines indicate the positions of the σ bands of the h-BN layer corresponding to the pores (α) or wires (β) as shown in the inset. (d) Scanning tunneling microscopy images taken in constant current mode (150×150 nm^2, $I_t = 1$ nA, $U_t = 5$ mV, drift corrected). The inset (3.7×3.7 nm^2, $I_t = 1.5$ nA, $U_t = 0.5$ mV) reveals, after subtraction of the corrugation, the superhoneycomb unit cell with atomic resolution.

The structure of the unit cell was further investigated with scanning tunneling microscopy. Figure 2(d) shows large terraces of an ordered hexagonal structure similar to h-BN/Rh(111) [10,11]. The inset shows atomic resolution after subtraction of the superhoneycomb corrugation and exhibits the 11×11 superstructure of the h-BN. In contrast to the h-BN/Rh(111) nanomesh where the superhoneycomb is imaged with pores surrounded by wires, here the contrast of the image is inverted. This is not found to systematically depend on the tunneling voltage, although certain tip conditions produced images with reversed corrugation. We propose that the imaged corrugation in h-BN/PtRh(111) has its origin in the higher local density of states of Rh as compared to Pt [1].

To quantify the Rh enrichment in the top layer we applied angle scanned x-ray photoelectron diffraction (XPD) [41]. Figures 3(a)–3(d) show XPD patterns of the Pt $4f_{7/2}$ ($E_{\text{kin}} = 1175.5$ eV) and the Rh $3d_{5/2}$ ($E_{\text{kin}} = 939.8$ eV) XPS lines of bare PtRh and h-BN/PtRh. The stereographic maps display patterns as observed for fcc(111) structures [42]. Thus, Rh and Pt atoms share the same lattice sites and any preferential ordering is not obvious. To visualize the changes in the substrate upon growth of h-BN the cross ratio X of the four XPD maps is displayed in Fig. 3(e) with

$$X(\theta,\phi) = \frac{I_{\text{Rh}(h\text{-BN})}}{I_{\text{Pt}(h\text{-BN})}} \cdot \frac{I_{\text{Pt(bare)}}}{I_{\text{Rh(bare)}}}, \tag{1}$$

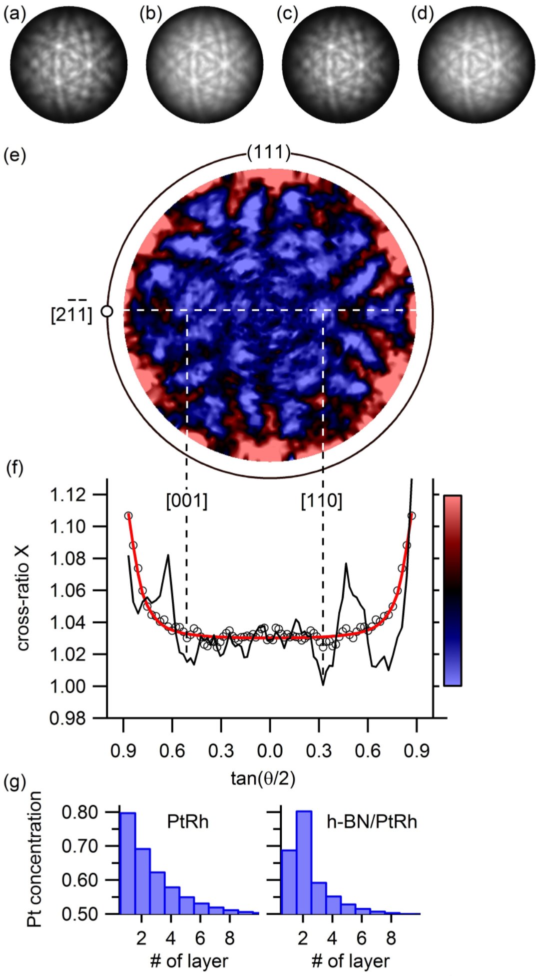

FIG. 3. Mg Kα excited x-ray photoelectron diffraction (XPD) patterns for Rh $3d_{5/2}$ ($E_{\rm kin} = 939.8$ eV) and Pt $4f_{7/2}$ ($E_{kin} =$ 1175.5 eV) emission. (a) Rh bare, (b) Pt bare, (c) Rh h-BN, and (d) Pt h-BN. (e) Cross-ratio X [Eq. (1)]. (f) Polar dependence of X on the azimuths containing ⟨110⟩ and ⟨001⟩ (solid line) and the azimuthal average (open circles). The red line is X as obtained from the Pt profiles in (g). (g) Pt concentrations as a function of the layer number. Note the swap of about 10% between the first and second layers.

where I is the intensity for given polar and azimuthal emission angles θ and ϕ. The cross ratio eliminates systematic errors due to the angular transmission or photoemission cross sections and allows very accurate quantitative statements on changes in the structure. High (low) X values indicate an increased relative Rh (Pt) contribution to the XPD patterns after growth of h-BN, and are shown in red (blue). The Rh contribution increases toward high polar angles, consistent with the XPS data in Fig. 1. Furthermore, X displays anisotropy in the azimuthal angles. The patterns resemble those of emitters in the second layer, where ⟨110⟩ and ⟨001⟩ forward-scattering directions are most prominent [18]. Figure 3(e) thus indicates that upon nanomesh formation, Rh atoms in the second layer swap sites with Pt atoms in the top layer, where no forward scattering is expected for polar emission angles smaller than 80°.

Figure 3(f) shows the polar cut of X containing the ⟨110⟩ and ⟨001⟩ directions, and the ϕ-averaged values for a given polar angle (black circles). These average values may be fit to cross ratios from a model of the Pt and Rh concentration in each layer, where the mean free path of the Pt $4f$ (1.47 nm) and the Rh $3d$ (1.25 nm) electrons enter, though the cross sections and the instrument transmission cancel in X. In the model, we adopt an exponential decrease of the excess Pt to the bulk value, and for the h-BN covered case, we allow a distribution deviating from the exponential decrease in the first two layers. The red line in Fig. 3(f) is the result of the two Pt concentration profiles in Fig. 3(g). We see that 80% of the top layer of bare PtRh consists of Pt atoms compared to 69% of Pt atoms in the second layer. After growth of h-BN the fit indicates 69% Pt in the top layer and 81% Pt in the second layer, which confirms the swapping of Pt and Rh in the first two layers and quantifies the amount to about 10 swaps per 10 × 10 unit cell. The fit results in a slightly larger (1.8 and 2.3 layers) decay constant of the excess Pt for the bare surface, which indicates that the h-BN influences the segregation profile beneath the second layer.

The swap of Rh and Pt atoms in the first two layers must be driven by an energy gain due to a stronger bonding of h-BN to Rh than to Pt [43]. Given the experimental fact that PtRh adopts a nanomesh structure, we propose a model where the

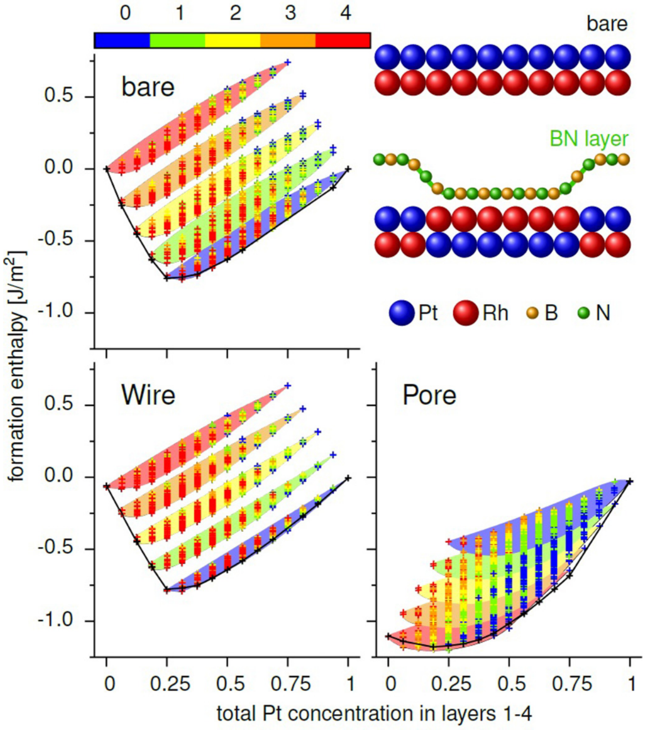

FIG. 4. Cluster-expansion energies (+) of approximately 13 000 different substrate structures each for the bare PtRh(111) surface (top left), for one of the h-BN wire regions (bottom left), and for the h-BN pore region (bottom right) as a function of Pt concentration. Information about the segregation profile in the two topmost substrate layers is color-coded by the number of Pt atoms per layer. The filled areas code for the topmost layer, and the colored + for the second layer (blue denoting an all-Pt, red an all-Rh layer). The energy scale in all plots is given with respect to the bare case. The top right panel summarizes the lateral segregation scenario where the first two PtRh layers in the unit cell are represented by chains of 10 atoms.

number of rhodium atoms accumulates in the pore regions of the first layer, and that this effect is fairly pronounced.

This lateral segregation picture is corroborated with an *ab initio* study that combines density functional theory (DFT) calculations with a cluster expansion, as has also been applied for bare PtRh surfaces [7,8,18,44,45]. Our surface-slab model is a 2×2 PtRh(111) substrate cell with four substrate layers (on top of fixed bulklike PtRh layers) and one (or none) h-BN layer on top of the substrate [18]. The total of 16 substrate sites can be arbitrarily occupied by Pt or Rh. The h-BN layer on top was placed in different positions in order to mimic locally the pore (α) and the wire (β) regions of the superhoneycomb lattice. For each region, the energetics of more than 350 fully relaxed DFT input structures was used as *ab initio* input for the cluster expansions, which then gave access to the energies of all possible Pt and Rh configurations in the substrate layers (roughly 13000 per region). This comprehensive scan enables us to directly see the influence of BN on the substrate's segregation profile at $T = 0$ K.

Figure 4 shows the formation enthalpies for bare PtRh, and for h-BN/PtRh with wire and pore registry for all atomic configurations in the first (color-coded filled areas) and the second (color-coded crosses +) layer. For example, the lowest energy configuration for bare and wire h-BN/PtRh has 0 Rh atoms in the first and 4 Rh atoms in the second layer, while this situation inverts for pore h-BN/PtRh, and lowers its energy. The energy difference between the different regions is the driving force for the laterally modulated segregation profile. The color-filled areas clearly demonstrate that the first-layer occupation dominates the energetics. For the bare case and the wire regions of h-BN/PtRh, Pt segregates to the topmost layer while the second layer is Pt depleted. The pore region, however, favors Rh segregation in the first and Rh depletion in the second layer. These results are sketched in the top right panel in Fig. 4, where the theoretical PtRh segregation profile with and without h-BN is shown for the first two layers. This is in perfect qualitative agreement with the lateral segregation model drawn from the experiments. The quantitative difference is assigned to the fact that the PtRh diffusion and thus the segregation freeze at finite temperatures, where entropy maintains Rh in the top layer of the bare surface.

In conclusion we present direct evidence that the top layer of PtRh is enriched with Rh, while the second layer is depleted of Rh, when a single layer of h-BN is grown on top. This swap imposes a lateral surface segregation profile, which is corroborated by (i) the h-BN displaying a nanomeshlike structure with two distinct BN bonding regimes, *and* (ii) by the fact that BN binds more strongly to Rh than to Pt. The lateral segregation scenario, where hexagonally packed Rh patches with a diameter of about 2 nm are formed, will have an impact on confined catalysis beneath a single layer of hexagonal boron nitride, or its use as a molecular template with an electronic structure modulation that exceeds those of nanomesh templates grown on pure metals. The findings are general and we expect lateral segregation profiles on the nanometer scale also for magnetic intermetallic alloys such as FePt. If one should succeed in removing the boron nitride without affecting the PtRh structure beneath, very high reactivities of these surfaces will be at hand.

Calculations were performed on the Vienna Scientific Cluster (VSC2). The surface diffraction measurements were performed at the Materials Science beamline of the Swiss Light Source, Paul Scherrer Institut, Villigen. This work was supported by the Swiss National Science Foundation.

---

[1] M. Schmid and P. Varga, Chem. Phys. Solid Surf. **10**, 118 (2002).

[2] H. C. Siegmann, L. Schlapbach, and C. R. Brundle, Phys. Rev. Lett. **40**, 972 (1978).

[3] K. J. Mayrhofer, V. Juhart, K. Hartl, M. Hanzlik, and M. Arenz, Z. Angew. Chem., Int. Ed. **48**, 3529 (2009).

[4] F. F. Abraham, Phys. Rev. Lett. **46**, 546 (1981).

[5] B. C. Han, A. V. der Ven, G. Ceder, and B.-J. Hwang, Phys. Rev. B **72**, 205409 (2005).

[6] E. Platzgummer, M. Sporn, R. Koller, S. Forsthuber, M. Schmid, W. Hofer, and P. Varga, Surf. Sci. **419**, 236 (1999).

[7] P. Welker, O. Wieckhorst, T. C. Kerscher, and S. Müller, J. Phys.: Condens. Matter **22**, 384203 (2010).

[8] T. C. Kerscher, W. Landgraf, R. Podloucky, and S. Müller, Phys. Rev. B **86**, 195420 (2012).

[9] F. Esch, S. Günther, E. Schütz, A. Schaak, I. Kevrekidis, M. Marsi, M. Kiskinova, and R. Imbihl, Surf. Sci. **443**, 245 (1999).

[10] M. Corso, W. Auwärter, M. Muntwiler, A. Tamai, T. Greber, and J. Osterwalder, Science **303**, 217 (2004).

[11] S. Berner, M. Corso, R. Widmer, O. Groening, R. Laskowski, P. Blaha, K. Schwarz, A. Goriachko, H. Over, S. Gsell *et al.*, Z. Angew. Chem., Int. Ed. **46**, 5115 (2007).

[12] E. Ćavar, R. Westerström, A. Mikkelsen, E. Lundgren, A. Vinogradov, M. L. Ng, A. Preobrajenski, A. Zakharov, and N. Mårtensson, Surf. Sci. **602**, 1722 (2008).

[13] A. Preobrajenski, M. Nesterov, M. L. Ng, A. Vinogradov, and N. Mårtensson, Chem. Phys. Lett. **446**, 119 (2007).

[14] P. Sutter, J. T. Sadowski, and E. A. Sutter, J. Am. Chem. Soc. **132**, 8175 (2010).

[15] E. Grånäs, M. Andersen, M. A. Arman, T. Gerber, B. Hammer, J. Schnadt, J. N. Andersen, T. Michely, and J. Knudsen, J. Phys. Chem. C **117**, 16438 (2013).

[16] A. Nierhoff, C. Conradsen, D. McCarthy, T. P. Johansson, J. Knudsen, and I. Chorkendorff, Catal. Today **244**, 130 (2015).

[17] H. Y. Cun, M. Iannuzzi, A. Hemmi, J. Osterwalder, and T. Greber, ACS Nano **8**, 7423 (2014).

[18] See Supplemental Material at http://link.aps.org/supplemental/10.1103/PhysRevB.93.161402 for experimental and calculating details. References [19–36] appear therein.

[19] T. Greber, O. Raetzo, T. Kreutz, P. Schwaller, W. Deichmann, E. Wetli, and J. Osterwalder, Rev. Sci. Instrum. **68**, 4549 (1997).

[20] H. Cun, M. Iannuzzi, A. Hemmi, S. Roth, J. Osterwalder, and T. Greber, Nano Lett. **13**, 2098 (2013).

[21] C. Steiner, B. Schönfeld, M. J. Portmann, M. Kompatscher, G. Kostorz, A. Mazuelas, T. Metzger, J. Kohlbrecher, and B. Demé, Phys. Rev. B **71**, 104204 (2005).

[22] K. D. Sattler, *Handbook of Nanophysics* (CRC, Boca Raton, FL, 2010).

[23] J. J. Yeh and I. Lindau, At. Data. Nucl. Data Tables **32**, 1 (1985).

[24] G. Kresse and J. Furthmüller, Phys. Rev. B **54**, 11169 (1996).
[25] G. Kresse and J. Furthmüller, Comp. Mat. Sci. **6**, 15 (1996).
[26] J. M. Sanchez, F. Ducastelle, and D. Gratias, Physica A **128**, 334 (1984).
[27] D. Lerch, O. Wieckhorst, G. L. W. Hart, R. W. Forcade, and S. Müller, Model. Simulat. Mater. Sci. Eng. **17**, 055003 (2009).
[28] P. E. Blöchl, Phys. Rev. B **50**, 17953 (1994).
[29] G. Kresse and D. Joubert, Phys. Rev. B **59**, 1758 (1999).
[30] J. P. Perdew, J. A. Chevary, S. H. Vosko, K. A. Jackson, M. R. Pederson, D. J. Singh, and C. Fiolhais, Phys. Rev. B **46**, 6671 (1992).
[31] J. Klimeš, D. R. Bowler, and A. Michaelides, J. Phys.: Condens. Matter **22**, 022201 (2010).
[32] J. Klimeš, D. R. Bowler, and A. Michaelides, Phys. Rev. B **83**, 195131 (2011).
[33] H. J. Monkhorst and J. D. Pack, Phys. Rev. B **13**, 5188 (1976).
[34] G. Makov and M. C. Payne, Phys. Rev. B **51**, 4014 (1995).
[35] J. Neugebauer and M. Scheffler, Phys. Rev. B **46**, 16067 (1992).
[36] F. J. García de Abajo, M. A. Van Hove, and C. S. Fadley, Phys. Rev. B **63**, 075404 (2001).
[37] F. Müller, K. Stöwe, and H. Sachdev, Chem. Mater. **17**, 3464 (2005).
[38] A. B. Preobrajenski, A. S. Vinogradov, M. L. Ng, E. avar, R. Westerström, A. Mikkelsen, E. Lundgren, and N. Mårtensson, Phys. Rev. B **75**, 245412 (2007).
[39] P. Willmott, D. Meister, S. Leake, M. Lange, A. Bergamaschi, M. Böge, M. Calvi, C. Cancellieri, N. Casati, A. Cervellino *et al.*, J. Synchr. Rad. **20**, 667 (2013).
[40] D. Martoccia, P. R. Willmott, T. Brugger, M. Björck, S. Günther, C. M. Schlepütz, A. Cervellino, S. A. Pauli, B. D. Patterson, S. Marchini *et al.*, Phys. Rev. Lett. **101**, 126102 (2008).
[41] C. Fadley, Progr. Surf. Sci. **16**, 275 (1984).
[42] J. Wider, F. Baumberger, M. Sambi, R. Gotter, A. Verdini, F. Bruno, D. Cvetko, A. Morgante, T. Greber, and J. Osterwalder, Phys. Rev. Lett. **86**, 2337 (2001).
[43] R. Laskowski and P. Blaha, Phys. Rev. B **81**, 075418 (2010).
[44] S. Müller, M. Stöhr, and O. Wieckhorst, Appl. Phys. A **82**, 415 (2006).
[45] S. B. Maisel, T. C. Kerscher, and S. Müller, Acta Mater. **60**, 1093 (2012).

6. Temperature induced changes of the conformation of $TbSc_2N@C_{80}$ on h-BN/Ni(111)

6.1. Introduction

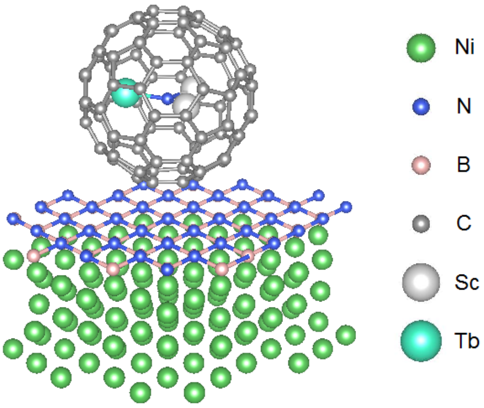

Figure 25: Sketch of $TbSc_2N@C_{80}/h$-BN/Ni(111) : A tri-metal nitride consisting out of 1 Tb, 2 Sc and 1 N acts as an endohedral unit being encapsulated by a C_{80} cage - as a substrate acts a Ni(111) crystal covered with a hexagonal boron nitride layer which acts as an insulating interdistance spacing layer (curtsy A. Seitsonnen), visualization by VESTA [98].

The letter on C_{60}: Buckminsterfullerene [99] in 1985 opened a new field of research. Stable carbon-fullerenes and the synthesis of rare-earth fullerenes [100] in combination with their magnetic properties make them interesting candidates for quantum computing and spintronics. This applies for the single molecule magnet (SMM) or single ion magnet (SIM) candidates, with their high stability and their carbon-shielded structure. Individual orientation ordering of the magnetic moments makes them promising candidates for data storage on the nanometer scale. While a lot of investigations focus on the magnetic properties, here we show temperature dependent investigations of the structural behavior and changes of the endofullerene $TbSc_2N@C_{80}$ as sketched in Figure 25. As a base structure $TbSc_2N@C_{80}$ consists of a tri-metal nitride cluster with one terbium (Tb) atom and two scandium (Sc) atoms bond to a nitrogen (N) atom. The Tb atom has an open f shell and thus following the Hund's rules, the trivalent ($4f^8$) Tb has a total angular momentum quantum number of $J = 6$. The ligand field induces a splitting of the Hund ground state and thus the magnetic moment of the Tb is directed along to the Tb-N axis [101].

In its most stable form, the tri-metal nitride cluster is encapsulated by a carbon cage consisting of 80 atoms of icosahedral form (there are also other, less stable, isomers), following the *Isolated Pentagon Rule* (IPR) in order to form the most energetic favorable structure [102]. Structurally that means that two different carbon species can be distinguished: 20 carbon atoms that border to three hexagons, the so-called (6,6) sites, and 60 carbon atoms where two hexagonal faces merge one pentagonal face, the (6,5) sites, as shown in Figure 27.

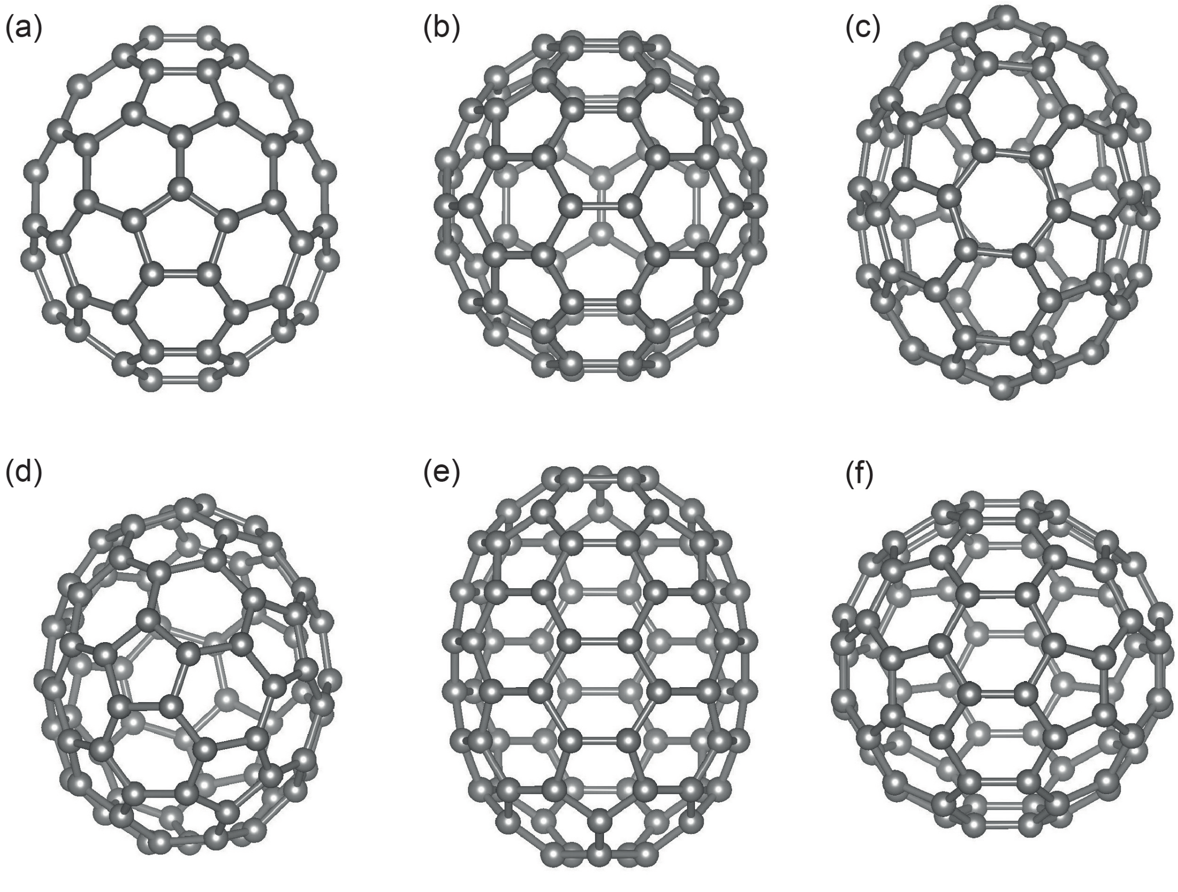

Figure 26: The six other isomers of C_{80}: (a) C_{2v}a; (b) C_{2v}b; (c) D_2; (d) D_3; (e) D_{5d}; (f) D_{5h}; taken from [103].

Seven different isomers were identified for the C_{80} which follow the *isolated pentagon rule* [104] as shown in Figure 26. In this thesis the icosahedral isomer $C_{80}I_h$ was used (as shown in Figure 25).

While $C_{80}I_h$ itself is instable as a fullerene, the inclusion of $TbSc_2N$ leads to a charge transfer of six electrons to the carbon cage [105]. This results in the valency of the system being $Tb^{3+}Sc_2^{6+}N^{3-}@C_{80}^{6-}$, which causes very high stability of the molecule (thermal stability for $T < 1000$ K).

As a substrate we are using a Ni(111) face centered cubic (fcc) single crystal. Nickel, as a strong ferromagnetic metal, may allow to switch the magnetic direction of $TbSc_2N@C_{80}$ by controlling the substrate [106]. While the carbon cages of endofullerenes are often immobilized and strongly bond to metallic surfaces after evaporation [50] we introduce an atomically sharp insulating spacing layer of hexagonal boron nitride (*h*-BN) [6]. The molecules should be decoupled from the catalytic influence of the transition metal surface and maintain translational and rotational degrees of freedom. Also the top layer of an *h*-BN/Ni(111) system is expected to have a reduced but nevertheless strong magnetic moment [107] and should reduce - but not cancel out - the interaction between $TbSc_2N@C_{80}$ and surface.

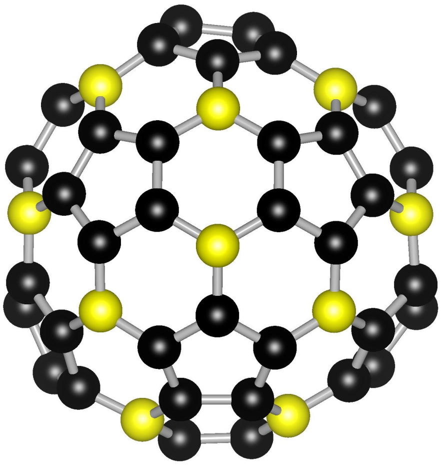

Figure 27: Sketch of the different species of carbon atoms within an icosahedral C_{80} cage: (6,5) (black) and (6,6) (yellow) carbon atoms, where 5 (6) stands for a pentagon (hexagon) face that coincides with two other hexagon faces in the vertices that constitute the atom sites.

6.2. Previous structural investigations on fullerenes and endofullerenes on surfaces

A lot of prior research was done in order to understand the structural behavior and alignment of fullerenes and endofullerenes with respect to surfaces. In 1996 Fasel, *et al.* [108] found the orientation of adsorbed C_{60} on metallic surfaces to depend on the surface cut. For both, Cu(111) and Al(111) substrates, the molecule was positioned on a hexagon with the carbon bonds of the bottom hexagon being aligned perpendicular to the $\langle 10\bar{1}\rangle$ direction for the case of Cu(111) but parallel to the $\langle 10\bar{1}\rangle$ direction for Al(111). Different absorption sites for C_{60} on substrates with a different surface cut were found: For Cu(110) the molecule was positioned on a (6,5) bond, aligned along the $\langle 001\rangle$ direction while a single edge atom was facing to the substrate when adsorbed on Al(001).

Investigations whether the C_{60}/Cu(111) would undergo an orientation flip, as observed for the case of C_{60}/Ir(111) [109], if heated above the sublimation temperature ($T_s = 575$ K), showed that even for temperatures $T = 720$ K no structural change was observed [110]. In 2005 Muntwiler, *et al.* [111] added a single monolayer of hexagonal boron nitride between C_{60} and a Ni(111) substrate. Temperature dependent measurements showed an increased unit cell size (from a 4 × 4 at room temperature to a $4\sqrt{3} \times 4\sqrt{3}R30°$ at $T = 160$ K). At the same time a change in binding energies of the molecular orbitals of C_{60} and in work function was observed. This can be explained with with a charge transfer between the C_{60} LUMO and the h-BN layer, due to a *rocking motion* with a change in alignment where the thermal energy changes the conformation.

Two years later Leigh, *et al.* [112] observed self assembled island formation for $Er_3N@C_{80}$ and $Sc_3N@C_{80}$ endofullerenes on different surfaces. While the self-assembly was possible on Ag/Si(111) at room temperatures, temperatures around $T = 250 - 300°$ C were required for monolayer formation on Au(111). Temperature dependent experiments lead to the picture of a molecular rotation around the z-axis at room temperature and a frozen conformation at liquid nitrogen temperature. Contrary, the covalent bonding between the molecules and Si(111) or Si(001) surfaces prevented the free motion. Also, bias-dependent contrast abnormalities for $Er_3N@C_{80}$ were found, interpreted as an electronic effect with different electronic densities of states [113].

The structural behavior of the endohedral units in the vicinity of a surface was investigated in 2009 by Treier, *et al.* [50] for the case of icosahedral isomer I_h $Dy_3N@C_{80}$/Cu(111). While the carbon cage was found to be aligned with the hexagon on bottom (similar to the case of C_{60}/Cu(111)) a slight tilt was observed with respect to the surface. The endohedral unit was found to be influenced by the presence of a surface and not align isotropically. The position of the nitrogen atom could be determined to be close to the center of the molecule. While the exact alignment of the Dy atoms inside the cage could not be determined, a single-orientation within a monolayer of molecules could not explain the data satisfactory.

The investigations of multilayer of $Ar@C_{60}$ by Morscher, *et al.* in 2010 [114] revealed also a centered position for the Ar atom within the molecule. In addition a strong coupling and hybridization between the endohedral unit and the carbon cage could be verified.

STM investigations on $Sc_3N@C_{80}$/Cu(110)-(2 × 1)O by Huang, *et al.* in 2011 [115] showed that the alignment of the endohedral unit, inside a cage position with a (6,5) site towards the substrate, can be switched by voltage pulses. Here the Sc_3N cluster can adopt three different pairs of conformations. Similar to thermal influence a second way to trigger the endohedral motion was verified.

Incidence angle dependent x-ray absorption experiments on $Dy_2ScN@C_{80}$/Rh(111) by Westerström, *et al.* [116] also found an influence of a metallic surface on the endohedral alignment in submonolayers of endofullerenes. Besides faster magnetic relaxation times, a preferred orientation of the Dy 4f orbitals parallel to the surface was found. The molecules were found not only to order structurally but also magnetically on the surface at $T = 4$ K.

6.3. Synthesis of the molecules

The $TbSc_2N@C_{80}$ molecules were synthesized in the Nanoscale Chemistry former group of Lothar Dunsch at the Leibniz-Institut for solid state and materials research Dresden (IFW). The molecules are synthesized using the Krätschmer-Hofmann method [117] as sketched in Figure 28. Here two carbon rods of a diameter of roughly $d \approx 10$ mm with an cylindric hole ($d_i \approx 6$ mm) are filled with fine carbon powder, desired metals (in our case terbium and scandium) and melamine ($C_3H_6N_6$) as the source of the nitrogen atoms [118]. The rods are cleaned in a vacuum environment by direct current heating. For the synthesis the rods are separated in a background pressure of $p = 200$ mbar He and a current of $I = 100$ A is alternatively applied to the rods. Arc discharge results in evaporation of the components and as a result the molecules combine amongst a vast variety of other products.

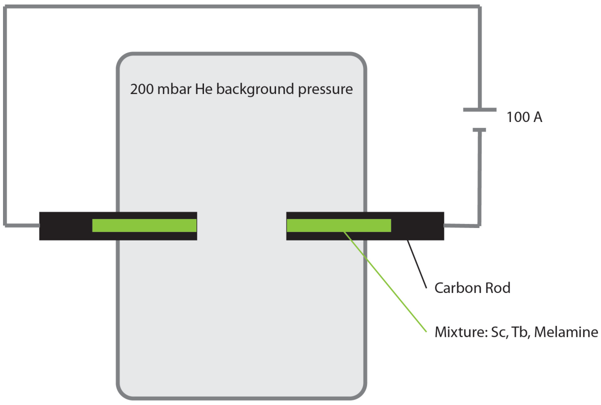

Figure 28: Sketch of a synthesis setup: Two carbon rods filled with a mixture out of Sc, Tb and melamine; arc discharge method is applied at a background pressure of 200 mbar He.

A large variety of molecules is formed: Mainly C_{60}, C_{70} and other stable fullerenes with a small amount of $Tb_xSc_{3-x}N@C_{80}$ (containing also $TbSc_2N@C_{80}$ in the order of $m = 50$ μg per synthesis cycle). In a first cleaning cycle organic contaminations are removed by acetone (C_3H_6O) extraction before using carbon disulfide (CS_2) to extract the fullerenes from the mixture of carbon products. Those cleaning cycles are repeated until only fullerenes and endofullerens remain.

In a further step the remaining mixture of molecules is dissolved in toluene (C_7H_8) and filtered before being purified in several cycles of high-performance liquid chromatography (HPLC) with mass spectrometry investigations inbetween.

6.4. Preparation of $TbSc_2N@C_{80}$/h-BN/Ni(111)

The Ni(111) single crystal was cleaned in repeated cycles of Ar^+ sputtering to remove residual contaminations and remaining surface oxides. In a second step O_2 dosing with $D = 1$ L at room temperature was performed to form an O_2 surface coverage in order to remove carbon contaminations during annealing cycles. The following annealing cycles were ramped up to $T = 1000$ K to allow the O_2 to react with the carbon contaminations and to remove excessive O_2 residues. During the last cleaning cycle prior preparation the O_2 dosing was skipped and $D = 70$ L of $(HBNH)_3$ (borazine) were dosed at a sample temperature of $T = 1100$ K to grow a monolayer of hexagonal boron nitride (h-BN),

following the recipe of Nagashima, *et al.* [6, 56].
The quality of the h-BN/Ni(111) preparation was confirmed using LEED (Figure 29a), XPS and XPD after growth of the h-BN layer. XPS (Figure 29b) reveals no C1s or O1s contamination above background. All signals could be accounted to be either elastic lines or Auger signals of nickel, nitrogen or boron (as shown in Figure 29b).

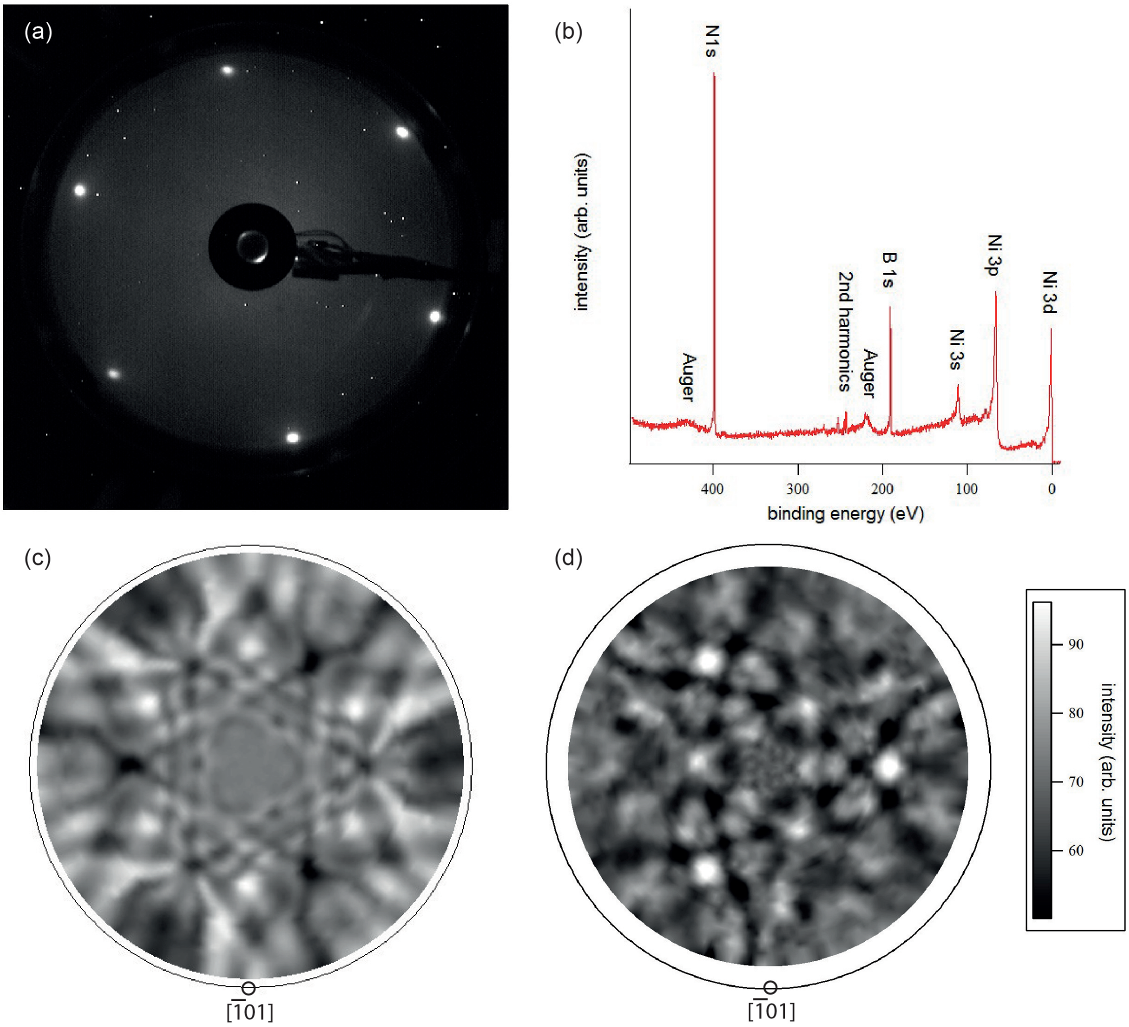

Figure 29: h-BN/Ni(111) after h-BN preparation: (a) LEED taken at room temperature, $E = 60$ eV; (b) XPS of the clean substrate h-BN/Ni(111), $h\nu = 600$ eV; (c) XPD N1s of h-BN/Ni(111) - 3-fold symmetry averaged and phi averaged, $h\nu = 600$ eV; (d) resonant excited Ni MNN - 3-fold symmetry averaged, $h\nu = 852.5$ eV.

Integrating the B1s, N1s and Ni 3s signals and normalizing them by cross sections [35, 119] allows to calculate the coverage which results in one monolayer of nitrogen and boron with respect to the Ni(111) single crystal surface. XPD measurements taken at

$h\nu = 600$ eV of the N1s elastic line (Figure 29c) show a well ordered structure without domains or rotations (a simulation is shown in Appendix C). This indicates that the preparation resulted in single domain h-BN with a three fold symmetric pattern because of the absence of a Ni atom in the second Ni layer below the fcc site of the h-BN layer [56].
This picture is consistent with LEED measurements taken at an electron energy of $E = 60$ eV (Figure 29a) [120] with no signs of azimuthally rotated h-BN units [15]. Also here the three fold symmetric pattern of the diffraction spots is visible.

Comparison to the substrate alignment of the Ni(111) fcc single crystal was done using resonant excited XPD on the Ni MNN auger transition as shown in Figure 29d. The fcc(111) structure of the substrate can be verified [121] and the adsorbate alignment can be determined. This results in an h-BN layer that follows the substrate's structural directions.
Evaporation of $TbSc_2N@C_{80}$ was performed using a Low Temperature Nanogramm Evaporator (LoTNE) [50]. The evaporator was positioned at an evaporation distance of $d \approx 1$ cm (refer Figure 30) between the Knudsen cell crucible and sample surface to obtain an optimization between homogeneity of the molecular beam at low and controllable evaporation temperature. The crucible holder was heated up, using a tungsten filament, to about $T = 800$ K for $t = 480$ s while keeping the temperature of the h-BN/Ni(111) sample at $T = 470$ K.
The quality of the preparation was directly checked with LEED. Further checks were performed using Scanning Tunneling Microscopy (STM), X-ray Photoelectron Spectrocsopy (XPS) and X-ray Absorption Spectroscopy (XAS) to verify the atomic compositions.

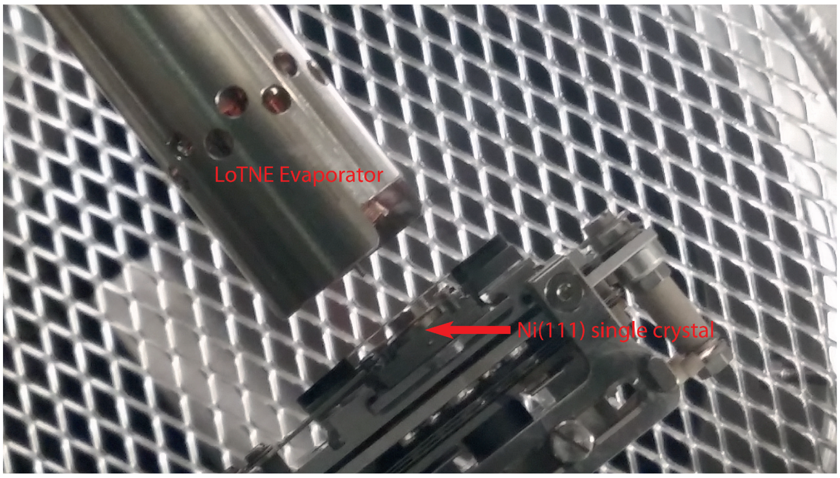

Figure 30: Photo of the evaporator during preparation. The distance between crucible opening and sample surface is $d \approx 1$ cm.

6.5. Characterization

6.5.1. Unit Cell and Superstructure at room temperature

A 4x4 superstructure was found to form on top of the 1x1 *h*-BN/Ni(111) by evaporated $TbSc_2N@C_{80}$ molecules, as indicated by LEED investigations (shown in Figure 31). The 4x4 superstructure was determined after evaporating a submonolayer of $TbSc_2N@C_{80}$ and by comparison to the 1x1 of the *h*-BN/Ni(111) substrate. The poor quality, as shown in Figure 31b, bases on the complication that the 1x1 refraction spots of the substrate cannot be resolved anymore when the molecular coverage approaches one complete monolayer [122].

Compared to C_{60} [111], the same superstructure was found for room temperature measurements, despite a different molecular diameter of about 8.3 Å [123] compared to 7.1 Å for C_{60} [124].

This is consistent with the inter-molecular distance of roughly $d = 1$ nm found by STM investigation of $Er_3N@C80$ [113] and corresponds to a unit cell of one $TbSc_2N@C_{80}$ per 16 *h*-BN units.

The adsorption of $TbSc_2N@C_{80}$ on *h*-BN/Ni(111) at a substrate temperature of $T = 480$ K leads to a well ordered superstructure with a low rate of disorder rings as shown in Figure 31a. This indicates a well ordered system with low domain rate [112] where the molecular ordering follows the substrate as visible in Figure 31b.

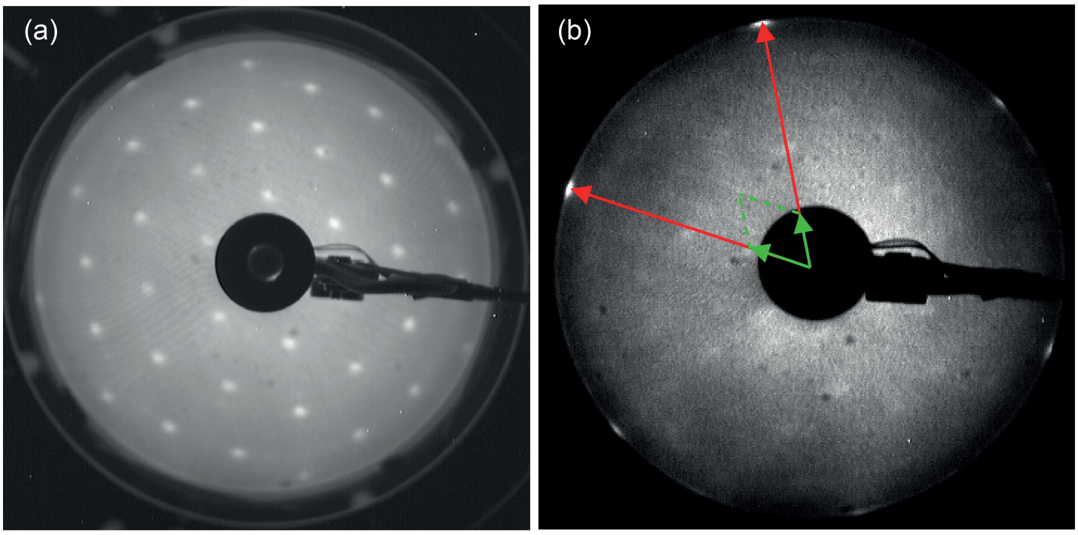

Figure 31: LEED measurements of $TbSc_2N@C_{80}$/*h*-BN/Ni(111) : (a) $E = 30$ eV, coverage $c \approx 1$ ML; (b) $E = 55$ eV: *h*-BN/Ni(111) 1x1 principal spots (unit cell indicated in red) and the arise of the 4x4 of $TbSc_2N@C_{80}$ (indicated in green), submonolayer coverage.

A strong disorder ring, as indication for a high amount of domains rotated with respect to each other, is visible if the substrate was held at room temperature $T = 300$ K during evaporation of the molecules (shown in Appendix B). This can be taken as an indication for a preferred three dimensional Volmer-Weber growth type [53] at room temperature. Thus we can assume that the system requires a higher energy for the molecules on the substrate to relax in a wetting layer of Frank-van-der-Merwe growth type [51] and shows consistency to the findings of Leight, *et al.* [112].

Large homogeneously ordered areas at a low rate of rotated domains were found using room temperature scanning tunneling microscopy (RT STM) on the surface after preparation (Figure 32b) indicating the Frank-van-der-Merwe growth type and being consistent with LEED investigations after adsorbing molecules at substrate temperatures $T > 450$ K. The dark spots in the STM image are vacancy sites where no molecule is positioned, the bright spots most likely molecules that appear to have a different DOS at the measurement conditions [113] than contaminations.

Higher resolution images as shown in Figure 32a reveal round molecules without intramolecular structure. A cut along the imaged topographic maxima (indicated with the red line in the top of Figure 32a and shown below the image) can be fitted with a sine and results in an intermolecular distance of approximately $d = 1$ nm.

Considering the substrate being h-BN/Ni(111) with a lattice constant of $a_{[110]} = 2.49$ Å the molecular ordering is accurately 4 times higher which is in good agreement with the 4x4 superstructure observed using LEED (Figure 31), thus one unit cell is verified to contain one $\mathrm{TbSc_2N@C_{80}}$ and 16 h-BN/Ni(111) units, as well as the molecules appear to follow the h-BN/Ni(111) lattice.

No intra-molecular structure could be resolved in the measurements at room temperature which can be taken as an indication for molecular carbon cage motion in form of a rotation around the z-axis as found for $\mathrm{Er_3N@C_{80}}$ at room temperature [113]. Since the molecules are resolved at $T = 300$ K and no translation movement beyond drift effects were observed in subsequent mapping of the same topographic area. The molecules are assumed to be fixed in their lattice positions and the degree of motion is limited to sole rotations.

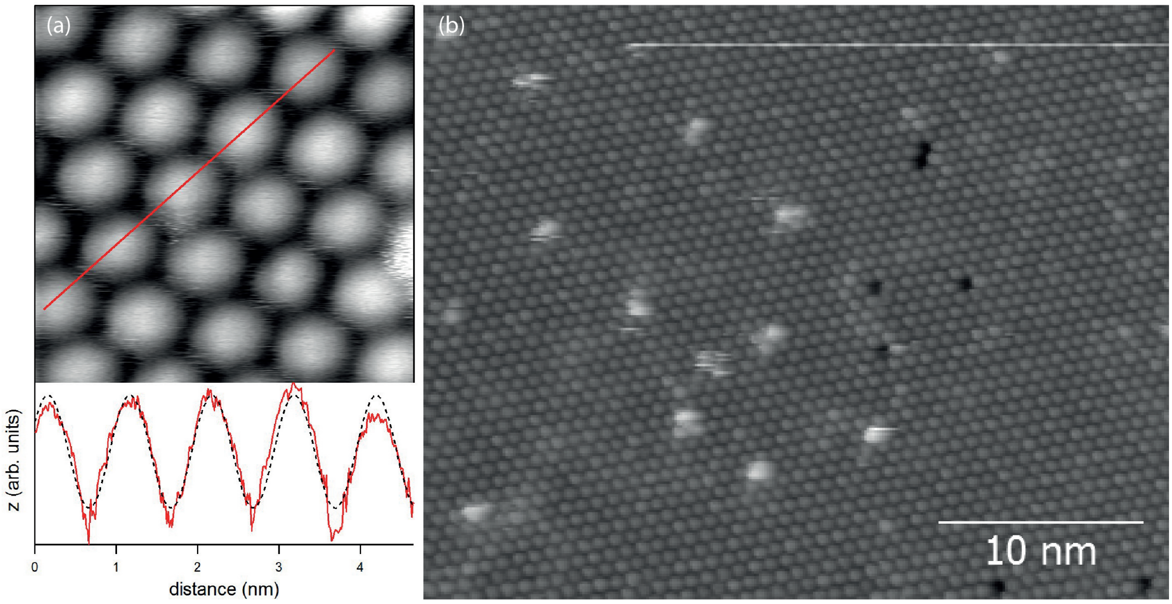

Figure 32: RT STM: (a) Area: $A = 4.4\text{x}4.4\ \text{nm}^2$ $V_B = -4$ mV, $I_t = 1$ nA; (b) larger area scan: $A = 30\text{x}40\ \text{nm}^2$.

6.5.2. Characterization of the molecular composition

Analysis of the chemical composition was performed using XPS at different photon energies to eliminate misinterpretation due to higher harmonic effects of the plane grating monochromator and to determine auger lines.

Characterization of $TbSc_2N@C_{80}/h$-BN/Ni(111) after $TbSc_2N@C_{80}$ evaporation with XPS only revealed elastic lines at expected binding energies for all molecular components in addition to the clean h-BN/Ni(111) as shown in Figure 29c. Clearly visible is the relative intensity decrease of the substrate components and the rise of the molecular components C1s, Sc 2p and N1s. The absence of any additional components verifies a high purity of the molecules in the evaporator.

The spectrum is dominated by a broad C1s signal (Figure 33b). The line displays a double peak structure with an additional shoulder which could origin from slight carbon contamination during the evaporation process. The structure arises due to the 80 different single binding energies of the carbon atoms in dependence on the bonding position (triple-hexagon and double-hexagon-pentagon) and the influence of the endohedral unit with the Tb and Sc pointing to the (6,5) sites of the carbon cage. Recent calculations corroborate that the 80 C1s eigenvalues are displayed as a multiplet spread over a binding energy of about $\Delta E \approx 1$ eV [123].

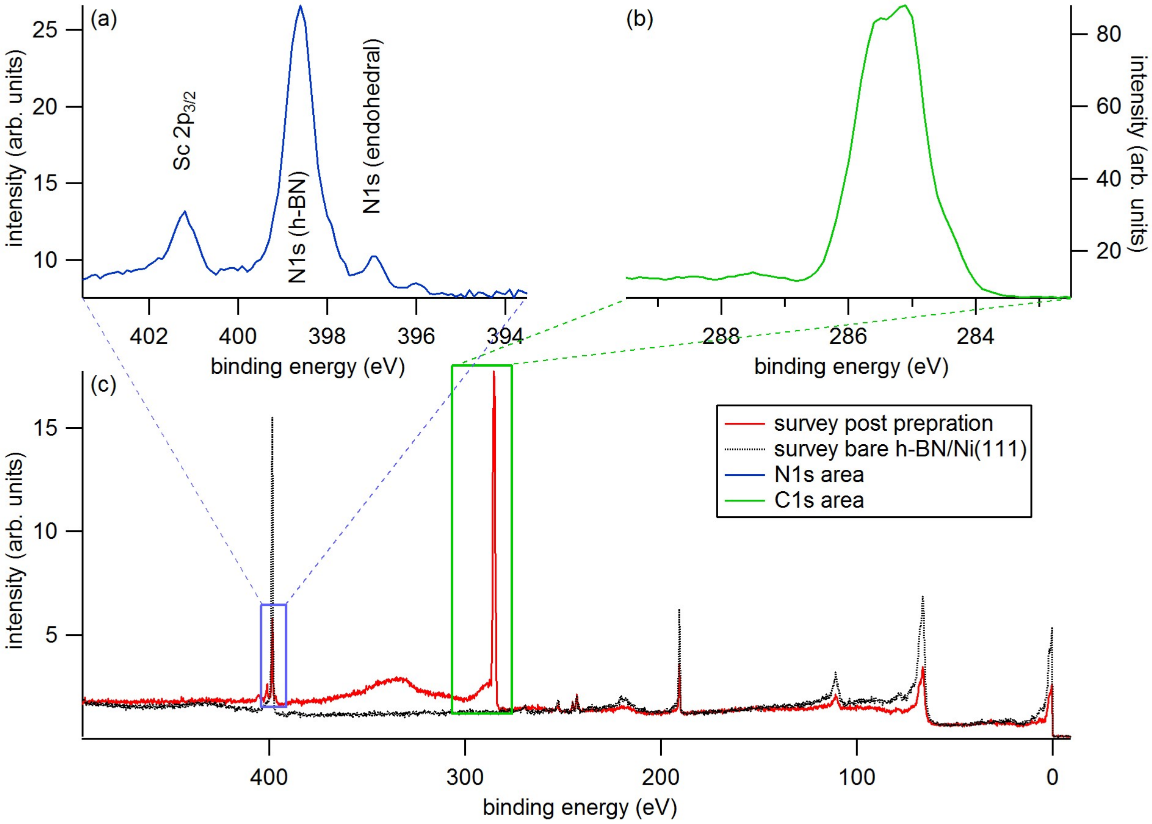

Figure 33: XPS spectra taken $h\nu = 600$ eV after TbSc$_2$N@C$_{80}$ preparation; detail scans of the N1s area (a) and the C1s area (b); (c) survey compared to bare h-BN/Ni(111): Note the elastic lines of the molecular components in the post preparation scan compared to the decreased signals from the substrates in the scan of the bare h-BN/Ni(111) shown as black dotted line.

The N1s elastic line of the h-BN layer dominates the spectrum in the binding energy range of 401 eV $> E_B >$ 394 eV as shown in Figure 33a. The N1s elastic line of the endohedral unit of TbSc$_2$N@C$_{80}$ at a binding energy of $E_B \approx 397$ eV and a valency of -3 is clearly separated from the h-BN signal with a nominal valency of -1. Additionally, the Sc 2p$_{3/2}$ elastic line appears at a binding energy of $E_B = 401.5$ eV. The constellation of the elastic lines of two molecular components in addition to a reference elastic line of the substrate allows this energetic range to be a good reference for preparation comparison. In the electronic structure, measured using a photon energy of $h\nu = 70$ eV, the occupied molecular orbitals are visible in addition to the h-BN/Ni(111) electronic states (Figure 34). Comparison to h-BN/Ni(111) measurements verifies the Highest Occupied Molecular Orbital (HOMO) of TbSc$_2$N@C$_{80}$/h-BN/Ni(111) at a binding energy of $E_B = 2.37$ eV, at a sample temperature of $T = 30$ K and a coverage of about 1 monolayer.

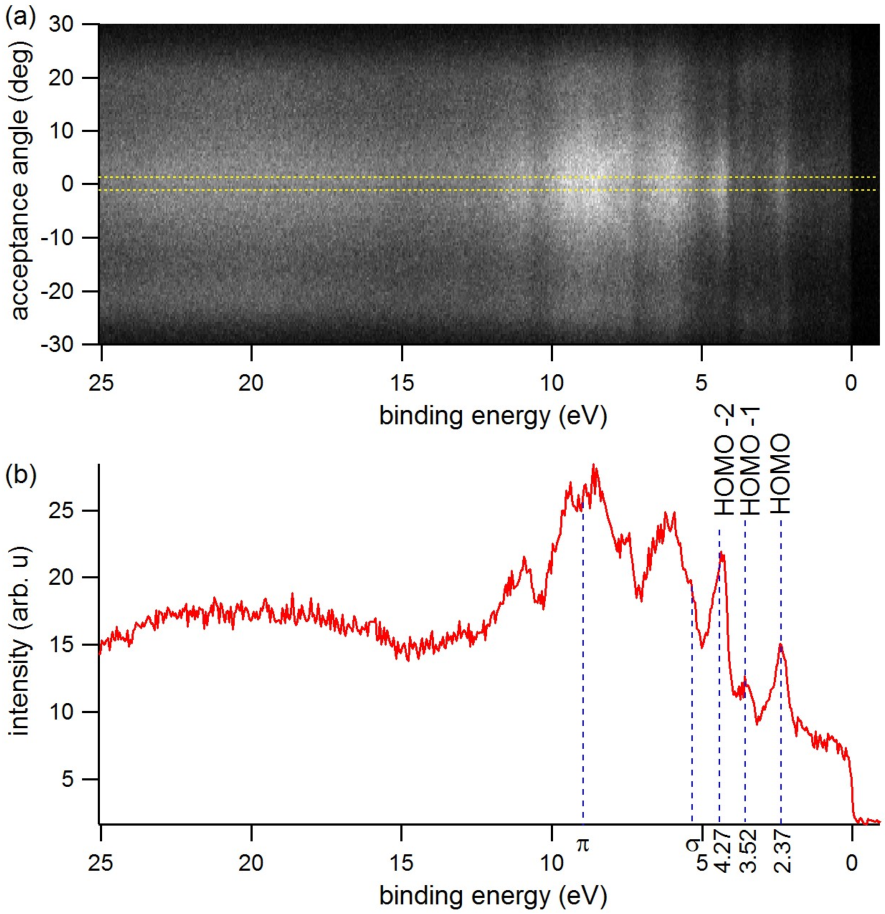

Figure 34: UPS measurement taken at a poton energy of $h\nu = 70$ eV at a temperature $T = 30$ K after $TbSc_2N@C_{80}$ preparation; (a) the molecular orbitals are visible in addition to the h-BN bandstructure with the typical signatures of π and σ band. (b) spectrum integrated over an acceptance angle of 5° ($-2.5° < \alpha < 2.5°$) as indicated with the yellow dashed lines in (a). At the Γ point the occupied states are visible in addition to the valence bands of Ni and the σ and π bands of the h-BN layer.

6.5.3. Magnetic Properties

Investigation of the magnetic properties of $TbSc_2N@C_{80}$ was done using a Superconducting QUantum Interference Device (SQUID) to measure the magnetic moment in dependence of temperature (Figure 35). For temperatures $T \leq 3.0$ K an opening of the magnetization curve (Figure 35a) could be found. While there is no remanence at zero field, a butterfly-like shape of the hysteresis curve was observed for low temperatures as shown in the inset of Figure 35a. The slope of the hysteresis curve at higher magnetic field origins from the diamagnetic background of the sample holder. This can be taken as a strong indication of $TbSc_2N@C_{80}$ being part of the single-molecule magnet

family [125, 126].
To visualize the temperature dependent effect of the opening of the magnetization curve we integrated the encapsulated area of the magnetization curves as shown in Figure 35b. The strong increment of the area for lower temperatures serves as a clear signature of the SMM character. The encapsulated area here does not reach zero due to the superconducting magnet with a remanence at zero field, which shows a false hysteresis of about 40 Oe at zero field.

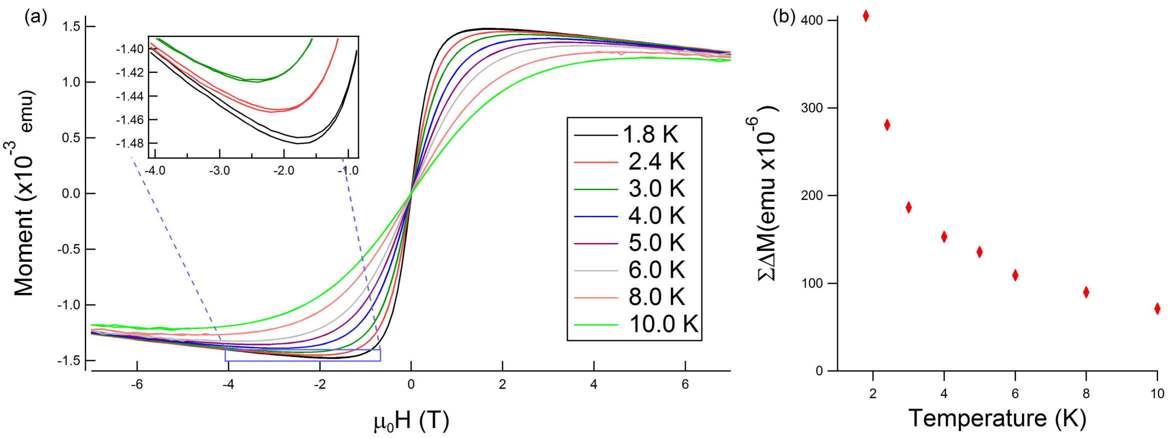

Figure 35: SQUID data of a dropcasted $TbSc_2N@C_{80}$ powder sample at a field scan rate of 700 Oe/minute: (a) magnetization curves of $TbSc_2N@C_{80}$ measured at different temperatures. Inset shows the hysteresis opening for temperatures $T \leq 3$ K; (b) areas enclosed by the magnetization curve in dependence of the temperature.

As a complementary proof for the SMM character of $TbSc_2N@C_{80}$ we measured the relaxation time using AC susceptometry. This method allows to investigate the dynamics of the magnetization by a variation of the AC frequency ω in one of the two coils inbetween which the sample is positioned. For SMMs that causes an induced voltage in the second coil. For the intermediate regime where the relation

$$\omega\tau \approx 1, \tag{25}$$

is valid for the relaxation time τ, the susceptibility χ can be approximated with

$$\chi(\omega) = \chi_S + \frac{\chi_T - \chi_S}{1 + i\omega\tau}, \tag{26}$$

based on Casimir and Du Pré [49] where χ_T is the isothermal susceptibility and χ_S the adiabatic susceptibility. For the case that $\{\chi_S, \chi_T\} \in \mathbb{R}$, the real and imaginary parts of the susceptibility follow as:

$$\chi' = \frac{\chi_T - \chi_S}{1+\omega^2\tau^2} + \chi_S \tag{27}$$

$$\chi'' = \frac{(\chi_T - \chi_S)\,\omega\tau}{1+\omega^2\tau^2}. \tag{28}$$

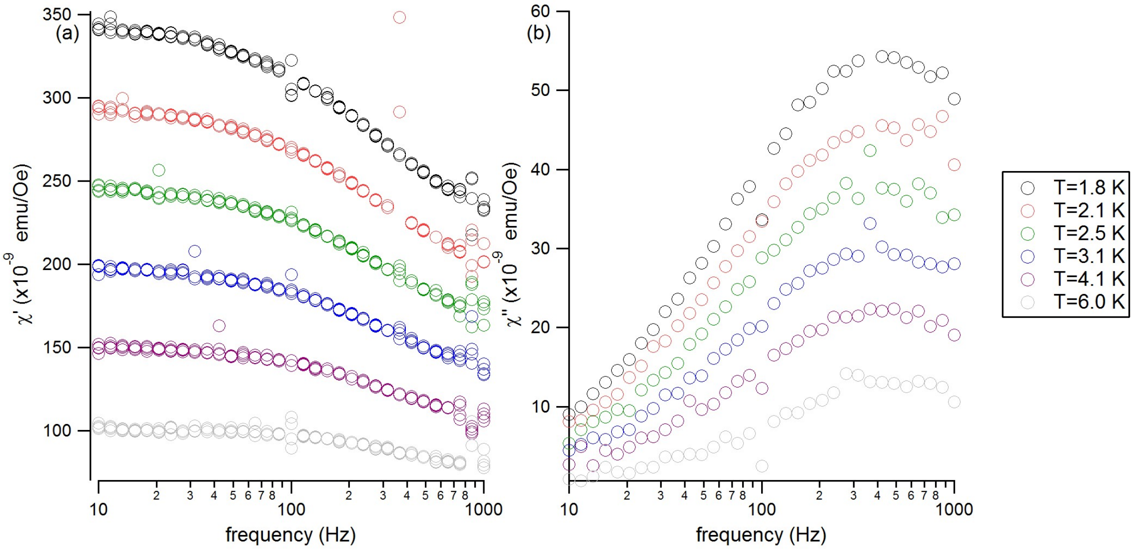

Figure 36: SQUID data: Measured susceptibility a dropcasted poweder sample of $TbSc_2N@C_{80}$ at different temperatures at zero field and an amplitude of the oscillating field of $\mu_0 H = 2.5$ Oe; a) real part χ'; b) imaginary part χ''.

Figure 36 shows the measured real part χ' (Figure 36a) and imaginary part χ'' (Figure 36b) of the susceptibility at 6 different temperatures ranging from $T = 1.8$ K to $T = 6.0$ K. For the condition

$$2\pi \cdot f \cdot \tau = 1, \tag{29}$$

the imaginary part has a maximum which we use to determine the relaxation time $\tau \approx 0.4$ ms (for a frequency $f \approx 380$ Hz). Even though the relaxation time is a lot shorter than the several hours found for $Dy_2ScN@C_{80}$ [101] we can conclude that also $TbSc_2N@C_{80}$ clearly fits into the family of SMMs.

6.5.4. The C1s core level splitting

The unusual broad C1s elastic line, with a width of about $\Delta E \approx 1.2$ eV, measured on all preparations of $TbSc_2N@C_{80}$/h-BN/Ni(111) will be discussed in this section. A good comparison are DFT calculated C1s eigenvalues and positions of $YSc_2N@C_{80}$ [123] to allow an interpretation. Except the difference in magnetic properties, where Yttrium is not paramagnetic like Terbium, both elements are quite close related and only differ slightly in ionic radius ($R_Y = 0.9$ Å for Yttrium compared to $R_{Tb} = 0.923$ Å for Terbium [127]).

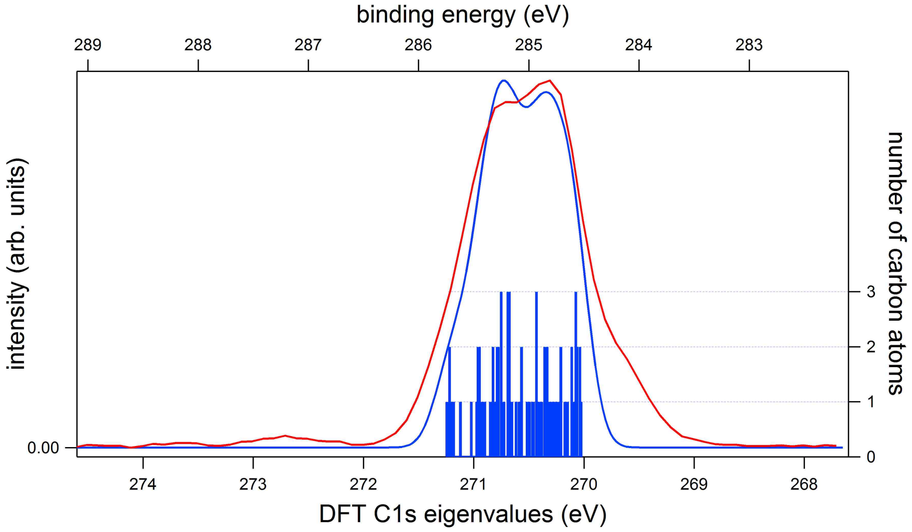

Figure 37: Comparison of the C1s spectrum taken at $h\nu = 800$ eV as shown in Figure 33 in red with a FWHM$\approx$ 1.3 eV, sum of 80 Gaussian peaks with a FWHM$\approx$ 1.1 eV and centered on the experimental data, calculated for the corresponding DFT C1s eigenvalues (blue bars).

DFT calculations for each C1s position within $YSc_2N@C_{80}$ yield different C1s eigenvalues, which spread over a width of $\Delta E \approx 1.2$ eV, as shown in the blue histogram in Figure 37. Calculated Gaussian distributions for each single C1s eigenvalue with the same weight and broadening ($\sigma = 0.16$ eV), result in a sum for all 80 distributions that reproduces the measured width of the C1s elastic line (as already shown in Figure 33 b - here: Figure 37 as blue line: the sum of calculated Gaussian distributions and red as the measured C1s elastic line). Despite an expected difference between the curves, originating from one endohedral component being Yttrium instead of Terbium, also the splitting can be reproduced. The shake-up satellite around $E_B \approx 287$ eV is neglected in this comparison.

In addition, in our idealized calculation only one molecule was considered, thus, in comparison to the experiment, also the neighboring molecules and the influence of the h-BN/Ni(111) surface is missing, that may contribute to the difference between calculated C1s eigenvalues and binding energy of about $\Delta E = 14.5$ eV.

Contrary to C_{80}, the binding energies of the carbon core levels for the case of C_{60} are less separated [128], thus the source of the broad spreading could origin from an influence of the endohedral unit in the C_{80} complex.

When plotting the calculated coordinate points of the endofullerene and color coding the carbon position in dependence of the DFT calculated C1s eigenvalue, as shown in Figure 38a, a strong influence of the distance between Carbon position and endohedral position on the binding energy becomes obvious. The higher C1s eigenvalues (dark color code) are close to the trivalent rare earth ions inside the cage. Since no obvious differences can be observed between calculated eigenvalues in vicinity of Sc and Y, we conclude that neither for Tb a more pronounced effect should be expected for the same C_{80} isomer. Here the endohedral components are plotted as blue (green) stars for tripple positive (negative) charged ions and all positions are size-coded for the third dimension (y).

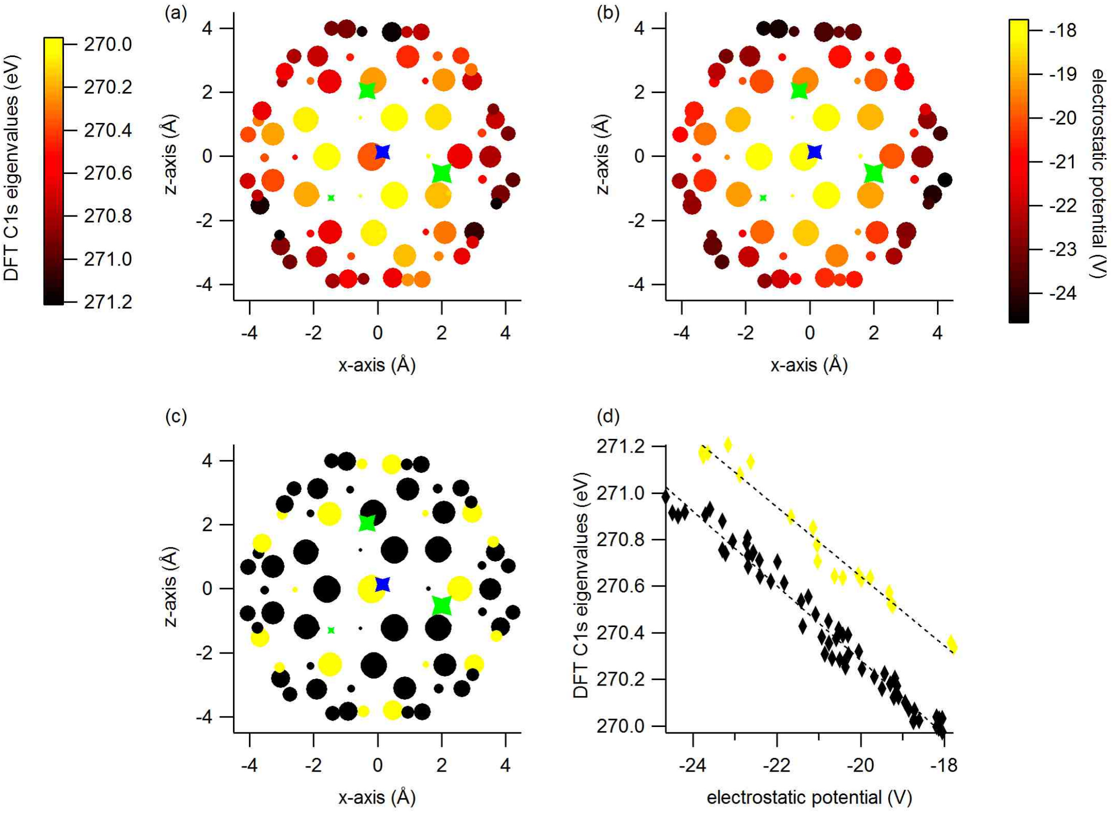

Figure 38: Influence of the position of the endohedral unit on the carbon cage, endohedral components in blue (green) for negative (positive) charge, cage components in black-red-yellow color code (third dimension indicated by marker size); (a) binding energy of the carbon components; (b) electrostatic potential at the positions of the carbon atoms; (c) carbon types: corner of three hexagons (6,6) in yellow, corner of two hexagons and one pentagon (6,5) in black; (d) binding energy versus electrostatic potential, carbon type color corresponding to (c).

The reason for the different binding energies can be backtraced to the Coulomb potential, of the endohedral components. Under negligence of the influence of the other carbon atoms (only a charge of $Q = 6e$ is shared by 80 atoms) we can approximate the electrostatic potential at each carbon position as

$$V_c = \frac{1}{4\pi\epsilon_0}\sum_i \frac{Q_i}{|\vec{r}_c - \vec{r}_i|}, \tag{30}$$

where c is the index of the carbon atom, Q_i is the charge of the endohedral component and index i corresponds to the endohedral component. Clearly visible is the strong correlation between DFT calculated C1s eigenvalues and electrostatic potential. The discrepancy for some atomic sites can be explained with different binding positions in the C_{80} network. The 20 binding positions to three hexagon (6,6) sites, as shown in Figure 38c in yellow, clearly show a higher C1s eigenvalue than the 60 double-hexagon-pentagon (6,5) sites (in black).

The linear correlation between calculated C1s eigenvalues and electrostatic potential for both (6,6) and (6,5) sites is visible in Figure 38d. Assuming a linear fitting function for the (6,5) and the (6,6) type carbon positions reveals slopes of $b = -0.15 \pm 0.12\ e$ and $b = -0.16 \pm 0.07\ e$, respectively. The slope is identical within error bound and results in an average of $\langle b \rangle \approx -0.155\ e$. The difference in offset of the DFT C1s eigenvalues between the (6,5) and the (6,6) lines is $\Delta a \approx 0.4$ eV which corresponds to the chemical shift between the two different carbon species of a Y_3@C_{80} molecule.

Polar angle dependent measurements reveal that the behavior of the different components changes in dependence of emission angle. The energy shift against polar angle, as shown in Figure 39, originates from a transmission function effect of the sample-analyzer geometry and the double peak structure as shown in Figure 37 is not visible due to higher pass energy and front end opening of the beamline, at a loss of resolution.

Fitting the double peak structure with two Gaussians is possible, based on the splitting results from high resolution XPS and the constraint of same width: Shown for the case of $T = 30$ K in normal emission angle in Figure 39b. The intensity I_1 corresponds to that of the Gaussian component with higher binding energies and clearly dominates the component I_2, resembling the lower binding energies.

For comparison, the intensity ratios $Q = I_1/I_2$, in dependence of polar emission angle, for $T = 30$ K and $T = 300$ K are shown in Figure 39d. Here the ratio for $T = 30$ K shows a decreasing slope towards higher polar emission angles. This may indicate that the stronger bond carbon atoms are located statistically closer to the substrate and are less likely to be detected due to the decreasing probing depth for emission angles $\theta > 40°$. Contrary, the ratio for the $T = 300$ K case shows a strong tendency to be around $Q \approx 1$, indicating a different conformation at room temperature and a can be interpreted as a more isotropic distribution of the differently bond carbon atoms.

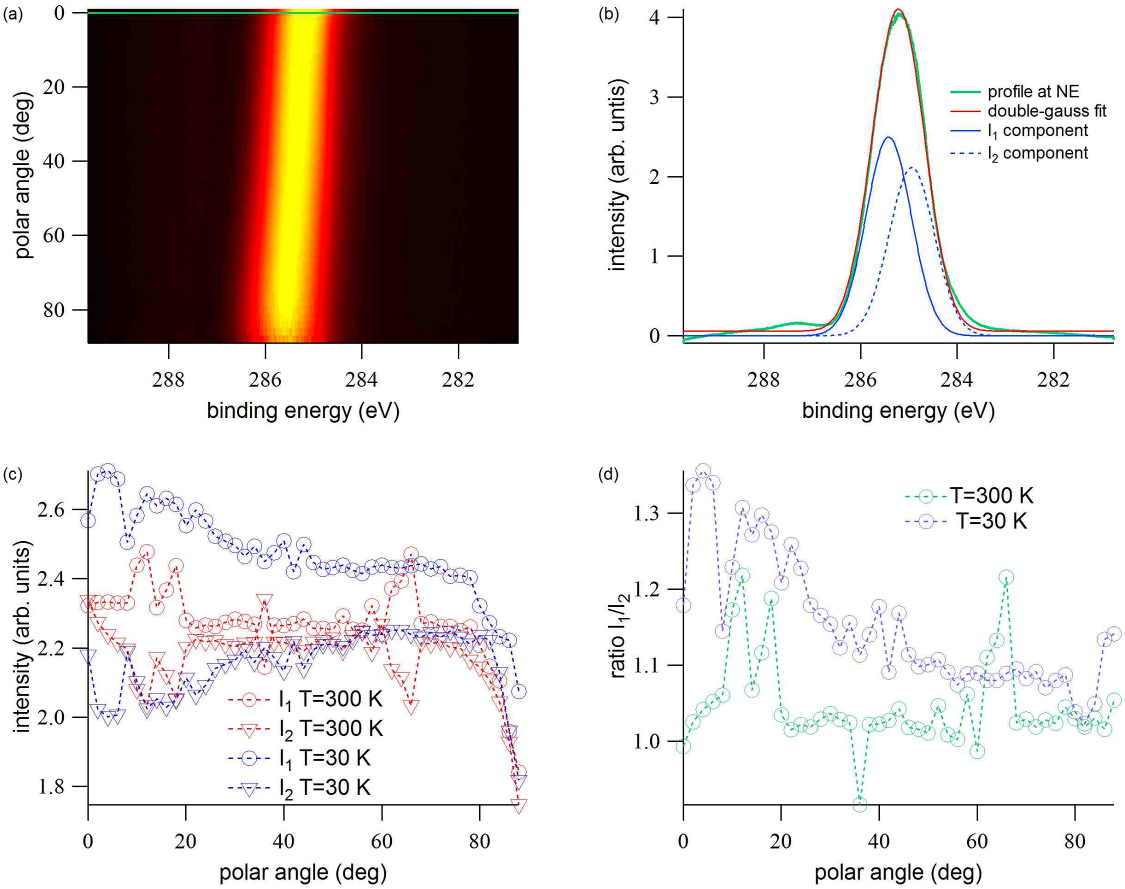

Figure 39: Polar angle dependence of the C1s components, $h\nu = 800$ eV; (a) intensity map for polar angle θ versus binding energy ($T = 30$ K); (b) two component fit of the C1s elastic line, the data profile in green corresponds to normal emission (as indicated with the green dashed line in (a)), the two different Gaussian components in blue: I_1 (I_2) for higher (lower) binding energy; (c) intensity of the two components against polar angle for $T = 30$ K ($T = 300$ K) in blue (red) and for the component with higher (lower) binding energy as circles (triangles); ratio of the intensities I_1/I_2 against polar angle.

6.6. Temperature dependence of endohedral and carbon cage motion

6.6.1. LEED: Temperature dependence of the size of the unit cell

LEED investigation of submonolayers of $TbSc_2N@C_{80}/h$-BN/Ni(111) taken at different sample temperatures show that the 4x4 superstructure (refer Section 6.5.1) at room temperature changes to an 8x8 superstructure at lower temperatures. Showing a clear difference to the C_{60}/h-BN/Ni(111) rocking motion [111] where a $(4\sqrt{3}\text{x}4\sqrt{3})$R30° was observed.

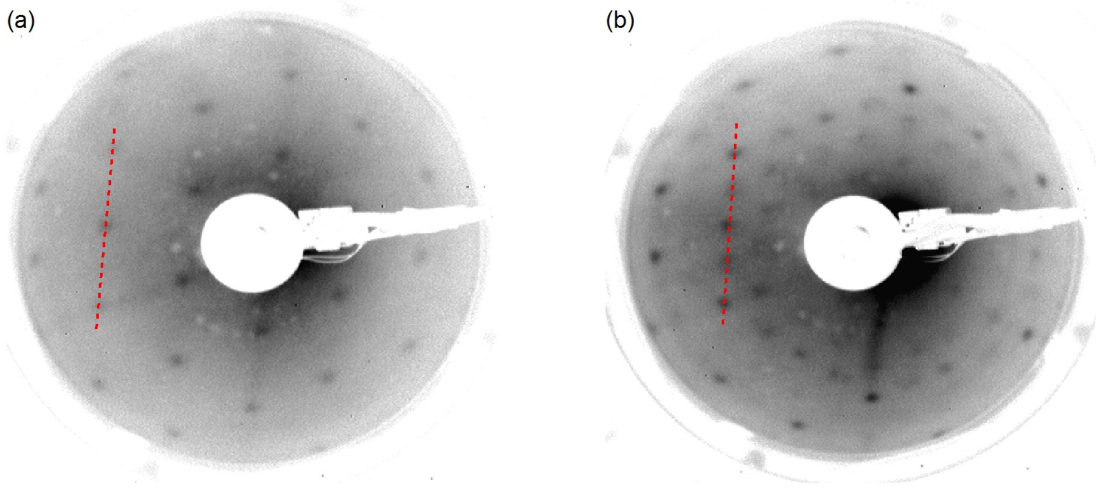

Figure 40: LEED images taken at an electron energy of $E = 30$ eV: (a) a 4x4 structure of $TbSc_2N@C_{80}$ is visible at T=300 K, (b) additionally to the 4x4 structure an 8x8 superstructure appeared at T=70 K.

Comparing the LEED images at $T = 300$ K (Fig. 40a) and $T = 70$ K (Fig. 40b) shows the clear change from 4x4 to 8x8. The position change of the LEED structure with respect to the electron gun and camera here is due to a slight bending of the manipulator and the sample holder during the cooling process.

To find an indication for the transition point from the 4x4 to the 8x8 superstructure, temperature dependent LEED investigations were done using a cooling ramp from room temperature to $T = 55$ K. To visualize the transition, cuts through three main spots of the 4x4 are shown (cut position is indicated with a red dashed line in Figure 40) of LEED measurements in steps of roughly $\Delta T = 30$ K as shown in Fig. 42a. The appearance of the additional spots of the 8x8 structure around $T \approx 210$ K indicates a change in the unit cell size where 4 C_{80} units combine to one.

Considering the 2-fold symmetry of the C_{80} molecules due to consideration of the I_h isomer and that hexagons are both oriented towards the top and the *h*-BN/Ni substrate (shown in Section 6.8.2), gives a possible explanation for the 8x8 symmetry due to the pentagon-orientation. Knowing that the molecules arrange following the substrate, allows us to conclude that 3 possible directions exist for the symmetry plane of the molecules. While the molecules are in rotational motion those symmetries can be neglected resulting in the 4x4 superstructure. At lower temperatures when the molecules are immobilized and aligned, groups of four molecules can form the same *alignment set* for neighboring groups and thus increase the unit cell to an 8x8 superstructure with respect to the substrate as sketched in Figure 41. This picture would explain both the 8x8 superstructure as well as the decreased spot intensity for the additional superstructure as there are three different orientation settings.

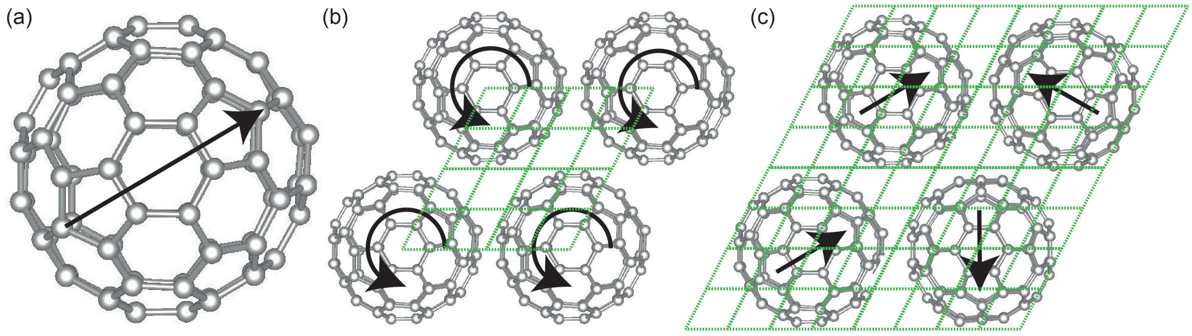

Figure 41: Schematic view of the changes in superstructure: (a) Sketch of the C_{80} cage with the arrow indicating the symmetry plane; (b) 4x4 superstructure: the molecules are in rotational motion forming a 4x4 superstructure - unit cell of the *h*-BN/Ni(111) substrate is indicated with the green dotted lines; (c) four molecules arrange to a set forming an 8x8 superstructure with respect to the substrate.

To determine the intensities the intensity distribution of LEED profiles (shown in Figure 42a) fits with a multiplet of convoluted Gauss distribution functions were done. To decrease the noise the two visible (8x8) superstructure spots were averaged.

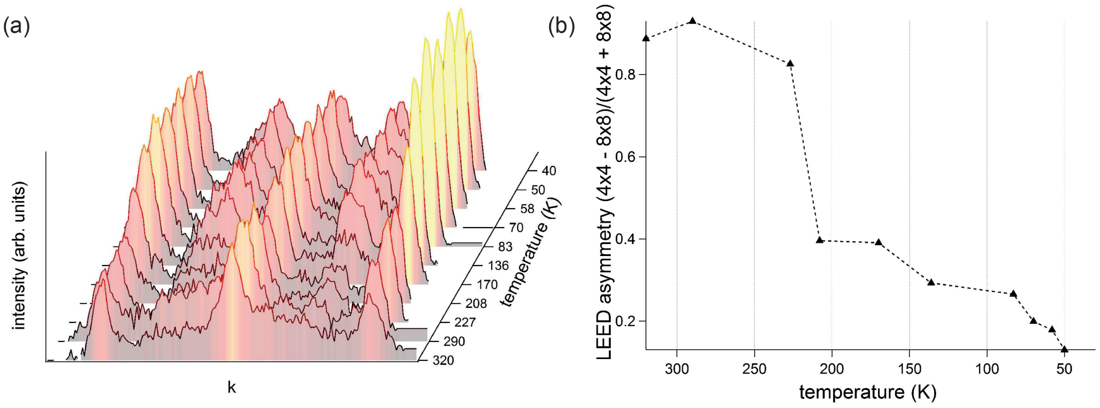

Figure 42: (a) LEED cuts as indicated along the red dashed line in Fig. 40 taken at different temperatures. Clearly visible is the rise of an additional superstructure (8x8) for $208\ K > T > 170\ K$; (b) Asymmetry of the intensity of the 8x8 and 4x4 superstructure spots in dependence of the temperature.

The effect can be visualized further by taking the asymmetry of the intensities of the

4x4 and the 8x8 superstructure spots following

$$A = \frac{I_{4x4} - I_{8x8}}{I_{4x4} + I_{8x8}}. \tag{31}$$

The asymmetry as shown in Formula 31 has the advantage of minimizing Debye-Waller effects at low temperatures compared to a simple division of intensities. Nevertheless, the Debye-Waller influence still shows influences for temperatures below $T < 100$ K, where, in combination with a slight tilt of the sample normal position due to cooling, the asymmetry of the intensities appears to change again.

This effect of a temperature dependent appearance of the $\left(\frac{1}{8}\right)$ spots additionally to the $\left(\frac{1}{4}\right)$ spots show a similar behavior like the findings of Benning, *et. al.* [129] and Goldoni, *et. al.* [130] and thus can be interpreted as an order-disorder transition similar to the case of C_{60} but at a lower temperature than the $T \approx 230$ K as found for C_{60}. Thus we can conclude that a transition from a rotational motion around the z-axis to the starting cage-immobility of the $TbSc_2N@C_{80}$ molecules on the *h*-BN layer takes place.

6.6.2. STM: temperature comparison

As an additional approach to verify the freezing of the C_{80} cage with respect to the substrate STM investigations at room temperatures and liquid helium (LHe) were performed. The comparison of the different measurements at room temperature $T = 300$ K and low temperature $T = 4.3$ K (shown in Figure 43 a and b, respectively) shows a vast difference in molecular resolution.

At room temperature no structure of intra-molecular resolution could be obtained and the molecules, though well ordered, are only mapped as spheres (Figure 43a). In comparison at LHe temperature ($T = 4.3$ K) the topography shows a resolution with filled states in molecular detail: A 6-protrusion structure is visible, as observed by Nörenberg *et al.* [113] (at LN temperature: $T = 78$ K) which slightly differs from the findings of Treier, *et al.* who resolved a 4-protrusion structure.

The different findings for $R_xSc_{3-x}N@C_{80}$ for different substrates like Ag/Si(111) and *h*-BN/Ni(111) compared to Cu(111), may be due to the different choice of the substrate and thus could explain the slight tilt of the $Dy_3N@C_{80}$ molecules on Cu(111). Nevertheless, the fact that intra-molecular structure can be resolved for different $R_xSc_{3-x}N@C_{80}$ on different substrates verifies the immobility of the cage at temperatures $T < 80$ K.

Low temperature STM experiments on $Sc_3N@C_{80}$ on Cu(110)-O [115] verified the immobilization of the carbon cage in addition to a frozen orientation of the Sc_3N complex in an energetical favorable position. Here the nitride complex could be switched between six different conformations using voltage pulses. Also thermal influence is known to enable endohedral motion [131, 132].

The effect of differently filled states as formerly been observed for $Er_3N@C_{80}$/Ag/Si(111) and $Sc_3N@C_{80}$/Au(111)/mica [112,113] can also be found for $TbSc_2N@C_{80}$/*h*-BN/Ni(111) as there are 'brighter' and 'darker' molecules (as visible in Figure 43a,b) which may change from image to image. Comparing measurements taken at $T = 78$ K and $T = 4.3$ K the effect of the 'brighter' molecules seems to be less pronounced if the temperature is reduced. As this effect may trigger single molecules during scans we suggest that the influence of the electron transfer between molecule and STM tip excites the molecule similar to voltage pulses [115]. A transition into a rotational motion of the cage though can be excluded since excited molecules still show the 6-protrusion intra molecular structure as visible in Figure 43b for two molecules.

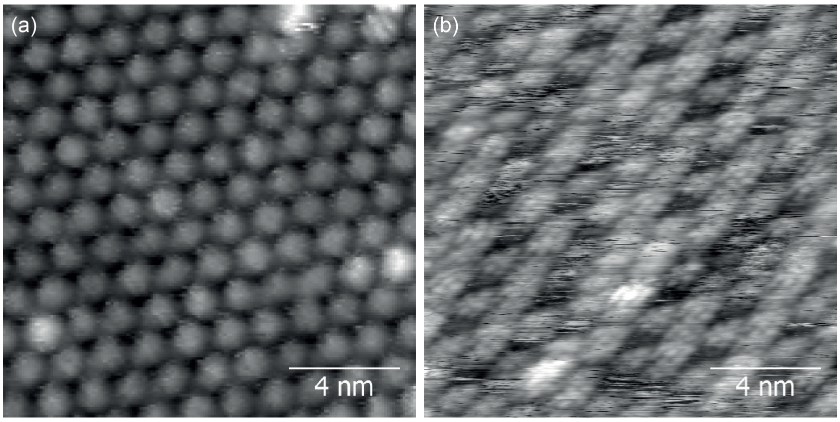

Figure 43: STM images of $TbSc_2N@C_{80}/h\text{-}BN/Ni(111)$ (no drift correction, $16\times16\ nm^2$): a) room temperature measurements, $V_B = -0.5$ V, $I_T = 10$ pA; b) LT measurements taken at LHe ($T = 4.3$ K, $V_B = -2.0$ V, $I_T = 100$ pA).

6.6.3. Temperature dependent XPD: Changes in the molecular conformation

Peak intensity changes in x-ray photoelectron diffraction (XPD) originates from forward scattering and interferences [40]. In XPD measurements this effect can be used to determine structural properties. These effects also have to be accounted for when measuring x-ray photoelectron spectroscopy (XPS) at different emission angles. A change in peak intensity can be interpreted as an indication for a changed likelihood of an atomic scatterer being positioned between emitter and detector and thus may increase or decrease the forward scattering.

In order to determine transitions in molecular motion we are taking advantage of this effect. The 2D Analyser with an acceptance angle of $\alpha = 60°$ in combination with the tilt angle τ of the CARVING manipulator was used to measure the elastic lines of the molecular components as a function of temperature and polar angle. The CARVING manipulator was set to a sample tilt angle of $\tau = +20°$ in order to allow the acceptance angle to map a cut of the polar hemisphere. The azimuthal angle ϕ was chosen such that the cut covered the spherical coordinates of enhanced and decreased forward scattering positions. The cut position is indicated with the red dashed line on the stereographic map of the C1s XPD signal as shown in Figure 44 and is the same (shown in Figure 62a). The XPD patterns are discussed in Section 6.8.2ff.

At the lowest reachable temperature in the CARVING manipulator we expect the $TbSc_2N@C_{80}$ system to be frozen and immobilized. LEED and STM measurements have shown that it is well ordered on the h-BN/Ni(111) substrate. XPS spectra were taken for the range of 60° acceptance angle continuously while increasing the temperature at a rate of $\beta = 1$ K/min.

A change in the forward scattering intensity was observed for all elastic lines in the temperature dependent XPS signal what suggests a change in the forward scattering cone positions and thus in the structural configuration. For the case of the resonantly excited Tb MNN and the C1s signals, Figure 45 visualizes the angle dependent and temperature dependent changes.

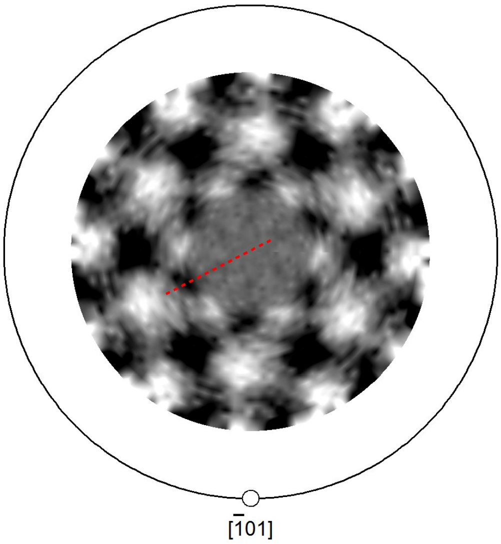

Figure 44: Stereographic map of the XPD signal of the C1s elastic line taken at a photon energy of $h\nu = 600$ eV. The red dashed line indicates measured angle settings of the temperature ramps.

To obtain comparable data for the different polar angles, the effects of the transmission function along the acceptance angle α needs to be removed, due to influences of the acceptance angle dependent transmission function (discussed in Chapter 4 and shown in Figure 17). The spectra were fitted and the background subtracted for each spectrum. In order to remove the transmission function, the spectrum for each acceptance angle was divided by the average value for all temperatures following

$$I_{\alpha,T} = \frac{\sum\limits_{i=0}^{n} I_{\alpha,i}}{n}, \tag{32}$$

where I is the integral over the signal peak after background subtraction, α the acceptance angle, n the number of different measurement temperatures. This allowed to obtain comparable intensity profiles for the different polar angles. The resulting intensity values are plotted as map points in a temperature-polar angle raster. Red corresponds

to higher values, blue to lower values.
For the Tb MNN transition map (shown in Figure 45a) a major decrease in the likelihood of forward scattering is apparent for the inner polar angles of $\theta < 20°$ in a temperature regime between 50 K $< T <$ 130 K is visible. Also an increasing forward scattering effect for $30° < \theta < 45°$ above 200 K can be observed. As the normalization method does not influence the temperature ramp for one given acceptance angle α, two different effects, at different temperature regimes, to influence the conformation, can be expected. The effects are not sudden, the transition in structural change and thus a supposed mobility onset appears to be smeared over a broad temperature regime.

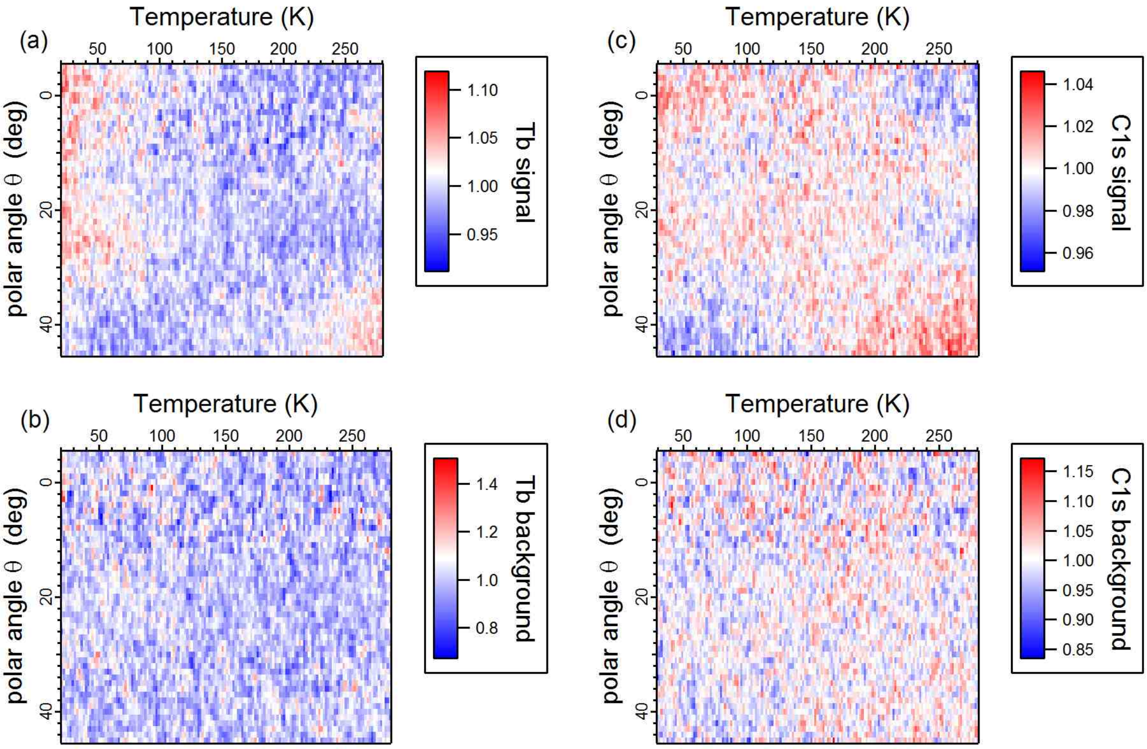

Figure 45: Normalized intensities plotted in a grid of temperature ($\Delta T \approx 1$ K) against polar angle ($\Delta\theta \approx 1°$) : (a) Tb MNN signal, (b) Tb MNN background, (c) C1s signal, (d) C1s background; red are higher values, blue are lower values.

This observation is supported by analogous measurements of the C1s elastic line. The same temperatures range shows changes in the signal intensity of C1s (Figure 45c) though at different polar angles of this polar cut. Here a decrease in the signal intensity is observed for $T >$ 210 K for $-5° < \theta < 5°$ and $20° < \theta < 30°$ and increased intensities for $T >$ 180 K at $35° < \theta < 45°$.
Considering the XPD structure of the C1s signal as shown in Figure 44, where no clear structure is visible for polar angles around $\theta = 40°$, the increase supports the suspected onset of cage motion in form of a rotation around the z-axis and supports the conclusions

obtained by LEED investigations as discussed in Section 6.5.1 and the comparison of RT and LT STM.

Following this argumentation, the changes in forward scattering likelihood, which are visible between 50 K $< T <$ 130 K, may show two different degrees of freedom for the endohedral unit with respect to the C_{80} cage and thus an onset in motion within.

Comparing the intensity maps with corresponding background maps for Tb MNN and C1s allows us to exclude an influence that is not based on the molecular behavior itself since the background does not show clear changes above background noise (Figures 45b,d) which appears to have some noise spikes and a broader range due to normalization over a lower signal.

The same transition temperatures can also be observed for the other elastic lines (N1s, Sc $2p_{3/2}$). Here a clear interpretation is more difficult due to signal to noise ratio being lower and thus a too high noise to visualize it in an angle-temperature dependent map as done for the more dominant signals (Tb MNN, C1s) above. The angle-averaged lines are shown in Figure 46 and coincidence with the same temperatures.

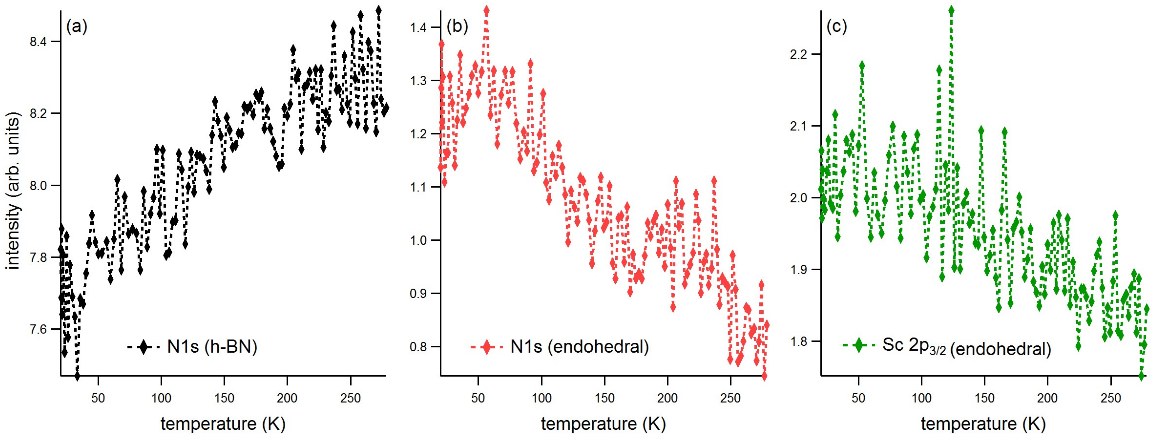

Figure 46: Temperature dependent intensity maps integrated over the entire acceptance angle α with the same manipulator setting as shown in Figure 45 for Tb and C: (a) N1s (h-BN), (b) endohedral N1s, (c) endohedral Sc $2p_{3/2}$.

The endohedral N1s (Figure 46b) intensity trend, integrated over all acceptance angles, also shows distinct areas of intensity (and thus forward scattering): For $T <$ 50 K an increase can be found, followed by a decreasing behavior up to $T =$ 150 K and a plateau of low changes up to $T =$ 230 K. The slopes of the h-BN N1s (Figure 46a) and Sc $2p_{3/2}$ (Figure 46c) show less distinguishable behavior though for both cases a plateau for temperatures $T >$ 210 K can be found.

In all intensity versus temperature measurements the same temperature ranges for changes can be observed and two temperatures remain of particular interest: $T_1 \approx$ 50 K and $T_2 \approx$ 210 K.

Additionally a clear trend between 80 K $< T <$ 140 K can be observed indicating constant change in motion for all endohedral components. As a characteristic temperature for this process we can determine the position of maximized slope, being $T_{\text{char}} \approx 41$ K. Comparing two different profiles along the temperature axis of the temperature dependent and polar angle dependent intensity map in Figure 47a, indicated with the blue and red line for the case of $\theta = 2°$ and $\theta = 42°$, reveals the main areas where a trend is visible and thus changes in motion of the $\mathrm{TbSc_2N@C_{80}}$ complex are expected as shown in Figure 47b. For 280 K $> T >$ 220 K the signal intensities decrease for both angles. The LEED asymmetry (as discussed in Section 6.6.1) shows the formation of the 8x8 superstructure at the same temperature. Hence we can conclude that the temperature point for immobility of the carbon cage with respect to the substrate is around $T \approx 220$ K.

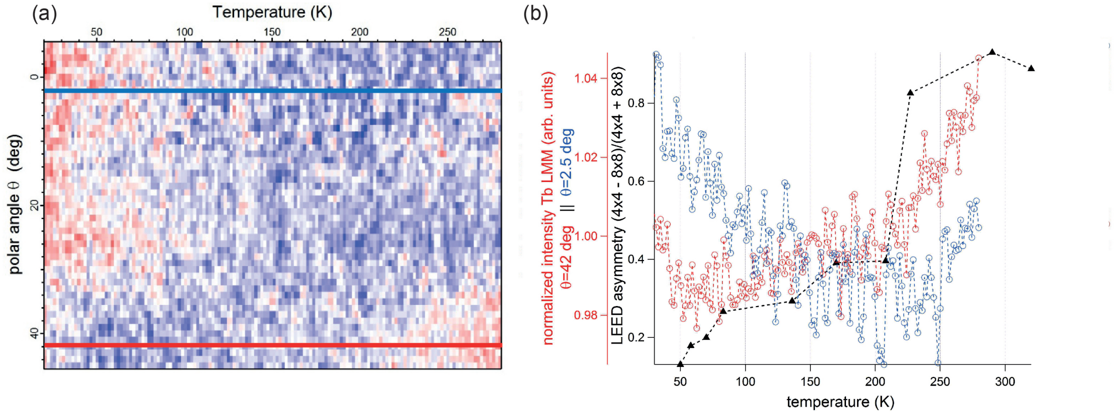

Figure 47: (a) XPD intensity cut of the Tb MNN signal in dependence of the polar angle and temperature as shown in Figure 45a.; (b) cuts at two different polar angles (blue at $\theta = 2.5°$, red at $\theta = 42°$) as indicated by the blue and red line in (a) - in black the LEED asymmetry for comparsion as shown and discussed in Section 6.6.1 and shown in Figure 42b.

Both profiles show a plateau for 210 K $> T >$ 150 K indicating that no changes in the mobility occurs in this temperature regime. For temperatures $T <$ 150 K changes in both intensity profiles suggest a further mobility-immobility transition. Since the $\mathrm{C_{80}}$ cage already is immobilized around $T = 210$ K, as discussed in Section 6.6.2 and 6.6.1 these intensity changes in dependence of temperature support the picture of a changing mobility of the endohedral unit.

This picture is in context with the findings of Huang, *et al.* [115] where voltage pulse induced motion was found to increase with the magnitude of the voltage pulse. Both thermal and voltage induced motion is expected to be a similar *hopping* between positions of potential minima with an increasing hopping rate for a ”faster” motion.

6.7. Chemical Shifts arising from Work Function changes

To investigate the temperature dependence of $\mathrm{TbSc_2N@C_{80}}/h$-BN/Ni(111) measurements at binding energy regimes of the molecular components were taken during a temperature ramp of $\beta = 1$ K/min from $T = 30$ K to $T = 280$ K. Figure 48 shows the resulting intensity maps in dependence of temperature and binding energy. All molecular components (C1s in Figure 48(a), N1s and Sc $2p_{3/2}$ in 48(b), resonant excited Tb MNN in 48(c)) shift alike in the same temperature regime of $70\ \mathrm{K} < T < 170\ \mathrm{K}$ and within the same binding energy range ($\Delta E \approx 300$ meV). The energy regime of N1s and Sc $2p_{3/2}$ in Figure 48b shows the difference in behavior compared to the substrate: The N1s elastic line of the *h*-BN layer remains at constant binding energy between the shifting endohedral N1s and Sc $2p_{3/2}$.

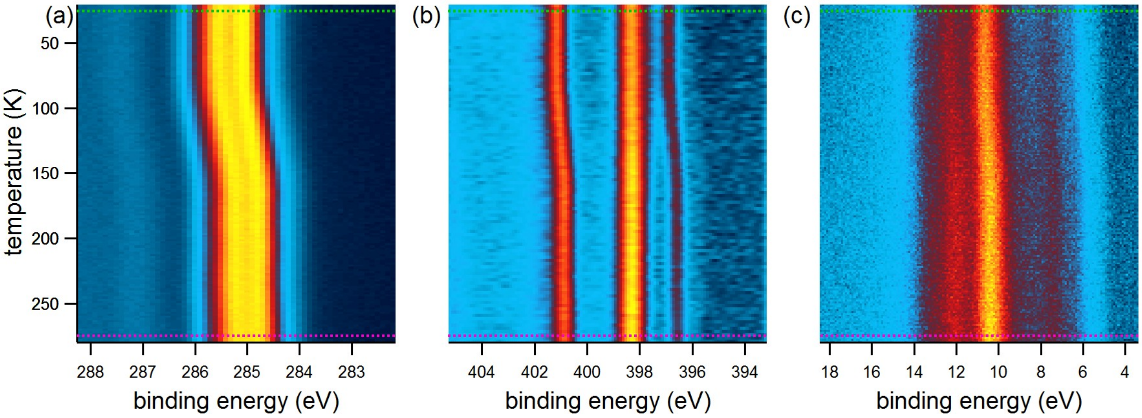

Figure 48: Heat ramps revealing chemical shifts, the dashed lines correspond to profiles shown in Figure 49 for $T = 30$ K and $T = 280$ K, normal emission angle: (a) C1s region (b) Sc $2p_{3/2}$, (c) Tb MNN - temperature ramped $\beta = 1$ K/min steps and measured binding energy.

The magnitude of the energy shift is clearly demonstrated by comparing profiles of the heat ramp maps at low temperature ($T = 30$ K) and close to room temperature ($T = 280$ K) as indicated with the dashed lines in Figure 48 and shown with corresponding color code in Figure 49.

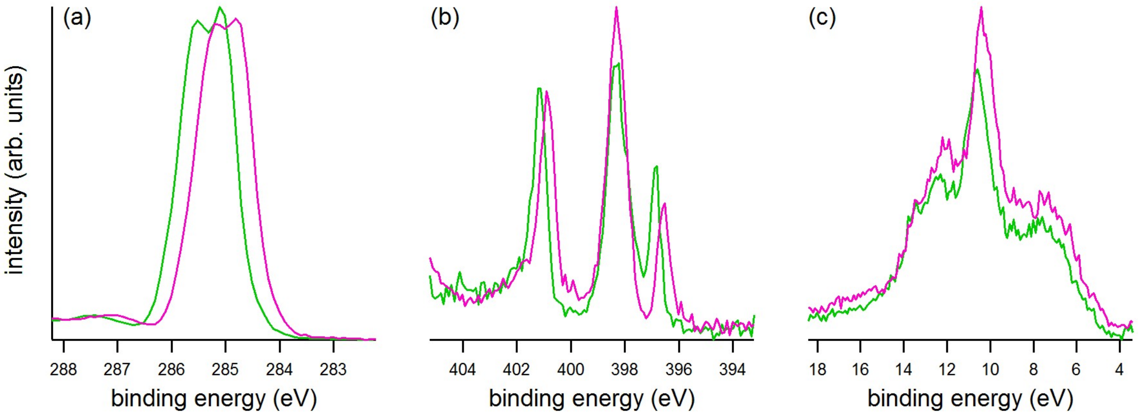

Figure 49: Profiles of Fig 48 - green corresponding to $T = 30$ K, magenta to $T = 280$ K (as indicated in the dashed lines in Fig. 48).

Comparing the signature of the C1s elastic line between room temperature and low temperature ($T = 30$ K) shows a clear shift of about $\Delta E \approx 280$ meV as shown Fig. 49a. The change in binding energy here occurs over a temperature range of approximately $\Delta T = 90$ K between $T = 80$ K and $T = 170$ K from $E_B = 285.0$ eV to $E_B = 284.7$ eV as indicated in a fitted maximum position plot in Figure 50a. Minor changes in the double peak structure can be distinguished and accounted to forward scattering effects. The carbon components of the C1s elastic lines, corresponding to the (6,5) and (6,6) positions, shift consistently as clarified with the double-Gaussian fit to approximate the double-peak shape of the C1s signal.

In comparison the behavior of the other molecular components Tb, N and Sc reveals a similar behavior (Figures 48, 49, 50 b for Sc $2p_{3/2}$ and endohedral N1s - c for the resonantly exited Tb MNN).

Figure 48b shows the endohedral N1s and Sc $2p_{3/2}$ elastic line at binding energies of 396.7 eV and 401.2 eV, respectively, flanking the N1s elastic line of the h-BN layer at 398.2 eV. Due to a different valency as discussed in Chapter 6.1 (3- for the case of the endohedral nitrogen in comparison to the 1- of the h-BN nitrogen) both N1s elastic lines are well separated by about 1.5 eV at room temperature. Thus a direct comparison between endohedral and substrate components is possible.

While all molecular components shift alike within the same temperature regimes, no such shift occurs for the case of the N1s elastic line of the h-BN as visible in Figure 49b. Thereby we can exclude the nature of this effect to originate from the entire sample and conclude that the effect is limited to the molecule.

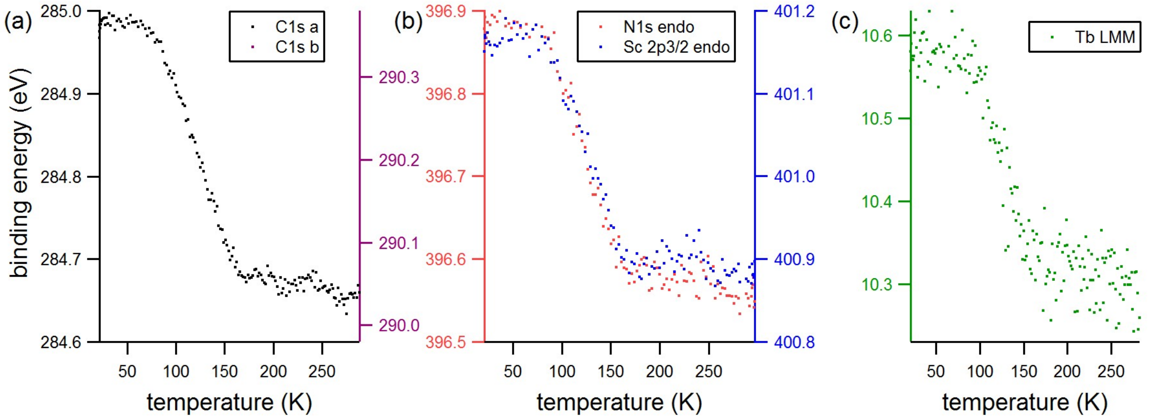

Figure 50: Fitted peak positions from Fig. 48 - the axis colors correspond to the colors of the graphs - (a) the 2 distinguishable C1s maxima, (b) the endohedral components of N1s and Sc $2p_{3/2}$, (c) the endohedral resonant Tb MNN.

Since all measured binding energies depend on the molecular work function, we investigated the dependence of the secondary cut-off for measurements taken within the ultra violet regime $h\nu = 70$ eV. Knowing that the position of the Fermi edge is temperature independent and only influenced by a thermal broadening this is sufficient to determine the temperature dependence of the work function.

Figure 51a shows the intensity map of the secondary cut-off of the spectrum in dependence of the temperature at the same rate as the measurements shown in Figure 48 but using a photon energy of $h\nu = 70$ eV. The sample was biased with $V_B \approx -9$ V to measure the secondary cut off. To determine the work function ϕ the position of the secondary cut-off was compared to the position of the Fermi-edge using

$$\phi = C_{Analyzser} \cdot [h\nu - (E_F - E_{sec})] \, , \tag{33}$$

where $C_{Analyzer}$ is the analyzer correction factor which was calibrated using h-BN/Ni(111) and resulted to be $C_{Analyzer} = 0.998$.

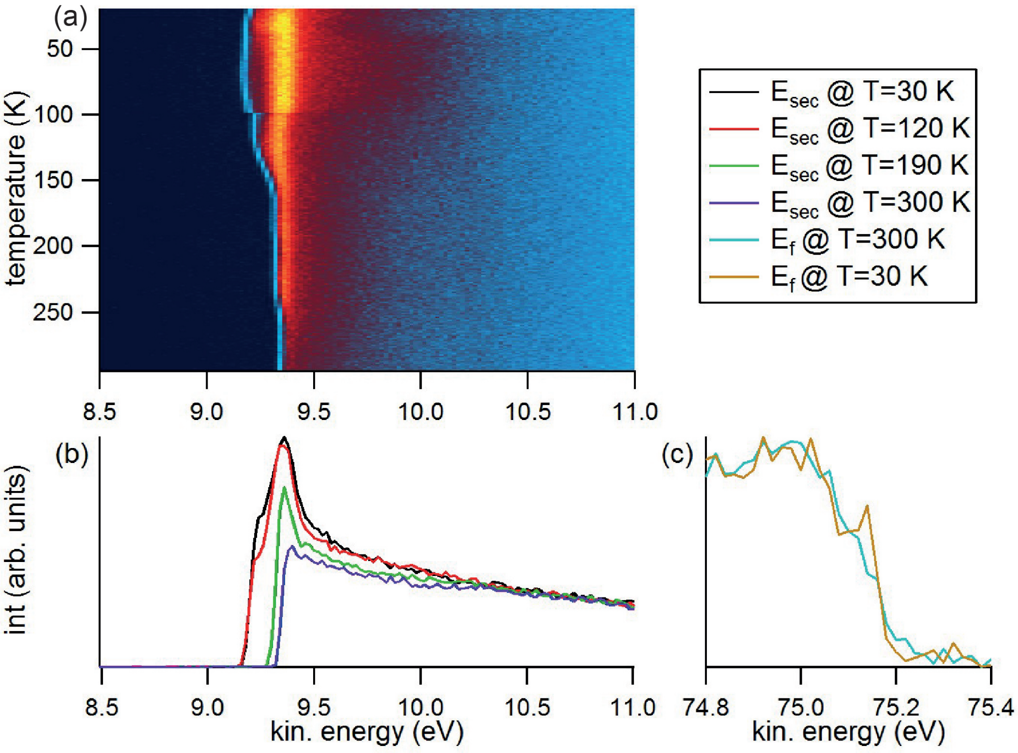

Figure 51: Temperature dependence of the work function of about 1 ML TbSc$_2$N@C$_{80}$ on h-BN/Ni(111), all measurements biased with $E_b \approx 9$ V and taken at $h\nu = 70$ eV: (a) secondary cut-off after applying a bias voltage in dependence of temperature and kinetic energy; (b) secondary cut offs at four different temperatures ranging from $T = 30$ K to $T = 300$ K; (c) Fermi edges taken at $T = 300$ K and $T = 30$ K.

For illustration four spectra at different temperatures are shown in Figure 51b. They indicate a shift of the work function between $T = 120$ K and $T = 190$ K. During the temperature ramp a core level signal disappears which could be identified to be the Ni $2p_{3/2}$ elastic line located around $E_B = 66.2$ eV. This elastic line does not follow the core level shift in dependence of the temperature as all components of the substrate.
Comparing measurements of the Fermi edge performed at $T = 300$ K and at $T = 30$ K, hints a possible electronic state at a binding energy of about $E_B \approx 30$ meV for low temperatures. Though reproducible with different preparations this peak is not observed for room temperature and might be explainable with an unoccupied state of TbSc$_2$N@C$_{80}$ shifting below the Fermi energy, though the energy resolution is too low to support clear statements. A more detailed analysis can be found in Appendix E.
The work function increases during the warm-up process from $\phi = 3.95$ eV to $\phi = 4.2$ eV which is in good agreement with the observed shifts in molecular binding energy of $\Delta E \approx 250 - 280$ meV (Figure 52).

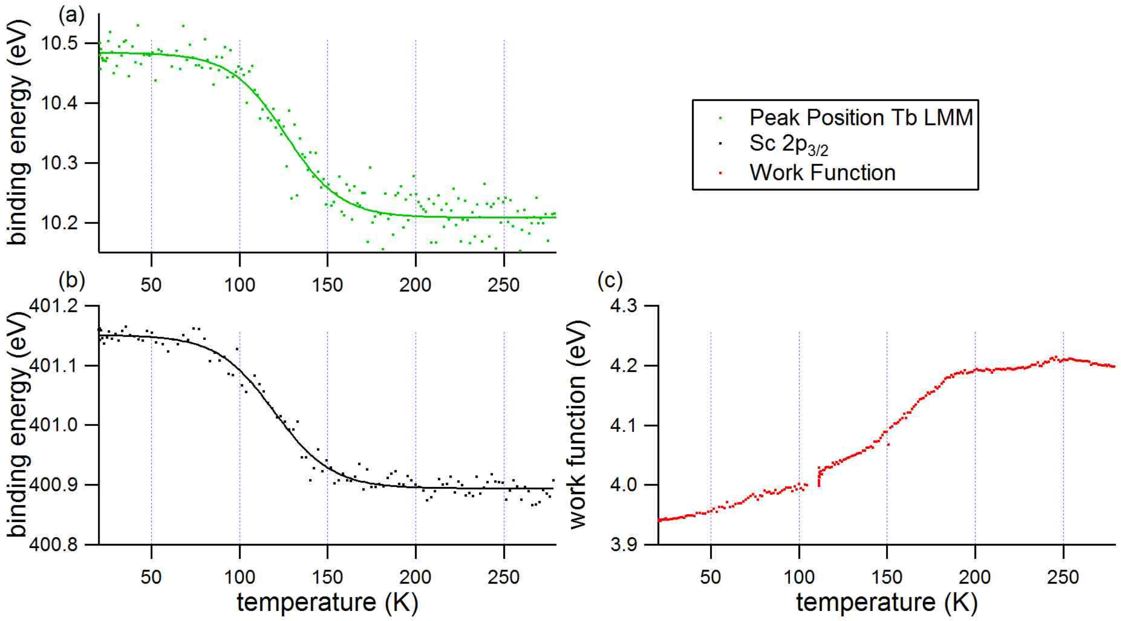

Figure 52: Comparison of work function shift with chemical shifts in dependence of temperature: (a) shows the shift in binding energy of the resonant excited Tb MNN; (b) Sc $2p_{3/2}$; (c) measured work function.

The regime of the shifting binding energy in dependence of temperature is consistent for the elastic lines of the molecular components as well as for the work function. The same temperature range of 80 K $< T <$ 170 K and the magnitude of the change in the range of about $\Delta E = 250$ meV is consistent between all endohedral components (Tb, Sc, N) and the work function ϕ. The carbon shift appears to be slightly larger ($\Delta E \approx 280$ eV) which could origin from the mobile charge distribution and its influence on the carbon positions within the cage (refer Section 6.5.4). No shifts were observed for the Ni elastic lines of the single crystal nor for the components of the h-BN layer.

Considering that tri-metal endofullerenes posses an electric dipole field [133], the work function change could be explained with a picture of the endohedral units statistically point towards the (6,5) positions closest to the h-BN/Ni(111) substrate in it's frozen state at $T = 30$ K. This conformation generates a total dipole moment towards the surface. An increased temperature, and thus the transition into a non-frozen state, enables the hopping along the (6,5) positions. With an increasing number of endohedral units being in motion, the total dipole moment towards the surface would be reduced. At temperatures where the hopping rate mimics permanent motion of the endohedral units, the distribution of the electric dipole orientation can be approximated as isotropic and thus the total dipole moment disappears.

Adding the temperature dependent work function shift of the molecular components to our findings for the carbon cage as shown in Figure 47 results in Figure 53. The increase in binding energy for 170 K $> T >$ 80 K coincidences perfectly with an increased forward scattering probability of the Tb signal for an emission angle $\theta = 2.5°$. At the same temperature a decreasing tendency can be observed for $\theta = 42°$. This corroborates the suggestion that the hopping rate of the endohedral unit along the (6,5) positions decreases over a wide range of temperature between 170 K $> T >$ 80 K causing both the chemical shift and changes in the forward scattering probability. Comparing the characteristic temperature of the chemical shift ($T_{\text{char,shift}} \approx 124$ K) with the characteristic temperature of the forward scattering (Section 6.6.3: $T_{\text{char,xpd}} \approx 41$ K) results in a higher temperature.

This could be explained by a slow hopping rate of the endohedral unit positions with respect to the carbon cage and the surface along more favored positions at lower temperatures. XPD is a very sensitive method for structural changes and a very statistical method (comparing measurement and molecular motion time scales), thus changes in scattering intensities can be detected once the endohedral unit turns unfrozen. At higher temperatures the motion could be more freely and the endohedral unit may align into all possible (6,5) positions. In this picture the second process would contribute stronger the work function shift.

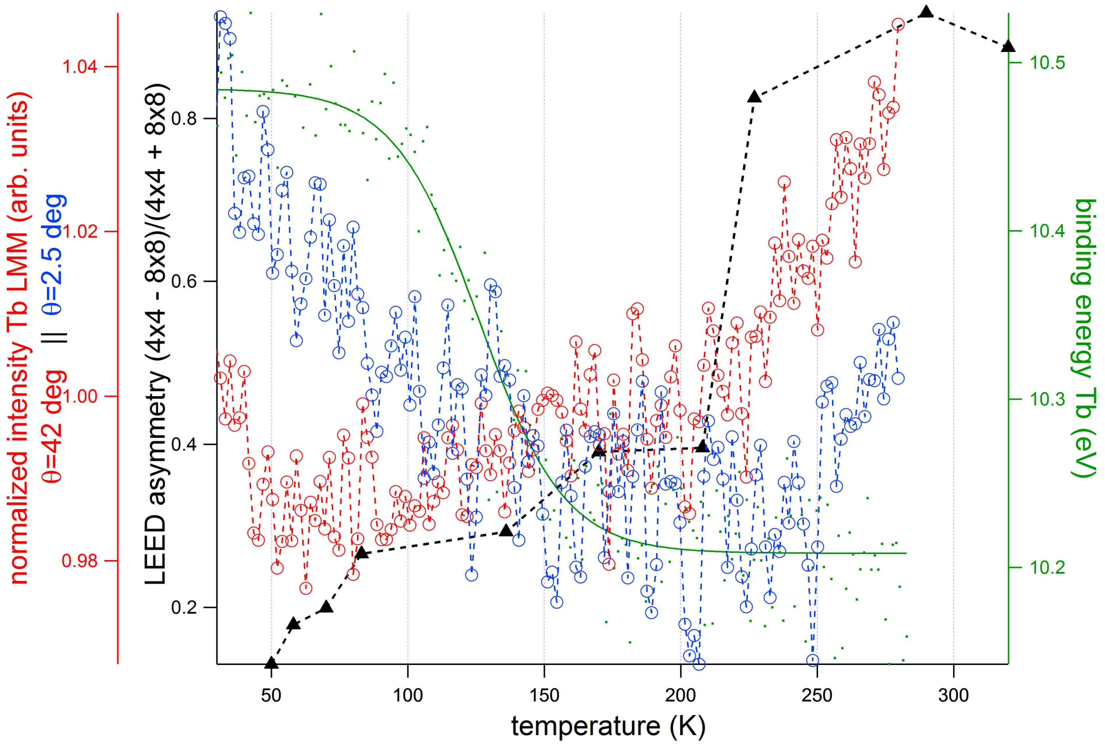

Figure 53: Temperature dependence of the observed effects: Basing on Figure 47 with the LEED asymmetry in black and the intensity scattering effects in red/blue additionally the binding energy of the Tb elastic line is shown in green.

6.8. Onset of endohedral motion in $TbSc_2N@C_{80}$

6.8.1. Field induced orientation of the endohedral unit

To have a direct access to the Tb behavior, the magnetic properties of the 4f spin orientation can be accessed, using SQUID measurements. In a strong magnetic field the endohedral units of a powder sample in the SQUID measurement position are expected to align with the magnetic field. In the absence of a magnetic field the endohedral units and thus the N-Tb axis is expected be randomly aligned.

The $TbSc_2N@C_{80}$ sample was cooled down from room temperature to $T = 1.8$ K in two different magnetic field environments. First a zero-field cooling (cooling down without magnetic field: $\mu_0 H \approx 0$ T) was performed prior measurement of the magnetization curve. To compare the influence of in-field cooling the sample was cooled down in a magnetic field of $\mu_0 H = 7$ T. The magnetization curves as shown in Figure 54a show a stronger magnetization for the in-field cooled measurements compared to the zero-field cooled case at $T = 1.8$ K.

In a second step the $TbSc_2N@C_{80}$ powder sample was warmed up at a rate of $\beta = 3$ K/s while measuring the magnetization. Comparing the two cases shows a different dependence of the magnetic moment on the temperature (shown in Figure 54b). Up to $T = 50$ K the magnetization shows a clear difference then the curves merge and asymptotically approach the same value above $T \approx 150$ K.

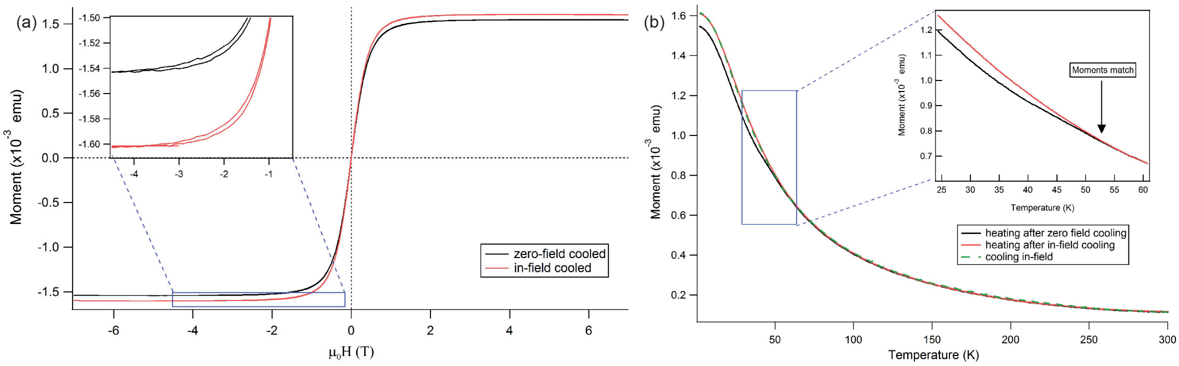

Figure 54: Magnetization data: (a) magnetization curve of $TbSc_2N@C_{80}$ in-field cooled at $B = 7$ T (red) and zero-field cooled at $B \approx 0$ T (black) taken at the same temperature $T = 1.8$ K; (b) temperature dependent magnetization measured during warm-up after in-field and zero-field cooling.

This difference in magnetic behavior can be explained by the alignment of the endohedral units that carry the magnetic moment. When the temperature drops below a critical temperature the endohedral unit freezes in motion and, for the case of the in-field cooled sample, the magnetic moments remain statistically better aligned, what results in a higher total magnetization.

For the case of zero-field cooling the alignment of the endohedral units (and thus the

N-Tb axis and the f-spin of the terbium) are not aligned after immobilization (freezing) of the endohedral unit, with respect to the C_{80} cage, when passing the a freezing temperature at $T_F = 50$ K. This results in a lower measured total magnetic momentum compared to the aligned endohedral units after in-field cool-down.

During the warm-up process in an external magnetic field of $\mu_0 H = 7$ T to measure the magnetic momentums, this can explain the difference up to a temperature of $T = 50$ K. After passing the freezing temperature, the endohedral units can align to the external field $\mu_0 H$. This transition appears to have a strong initial effect, though a temperature of $T > 150$ K is required for the the measured magnetization curves to overlap, as shown in Figure 55.

The characteristic temperature can be determined by the highest slope of the quotient of the heat ramps (in-field and zero field). The characteristic temperature here results in $T_{\text{char,squid}} \approx 41$ K, which is in very good agreement with T_{char} measured for the temperature dependent XPD profiles (Section 6.6.3). This strengthens the picture of an endohedral onset of motion (or freezing temperature) in this temperature regime.

This completes the picture of the different transitions as developed before and shown in Figure 53. The difference of magnetic moments ΔM for the in-field and the zero-field cooled $TbSc_2N@C_{80}$ sample during warm-up cycles is added in magenta. A clear coincidence is visible between the starting point of the work function shift around $T \approx 170$ K, the change in forward scattering probability and an increase in ΔM. The strong increase of ΔM around $T = 50$ K is in lie with a change in forward scattering probability for the $\theta = 42°$ profile of the Tb intensity map and the $\theta = 2.5°$ profile (as shown in Figure 47).

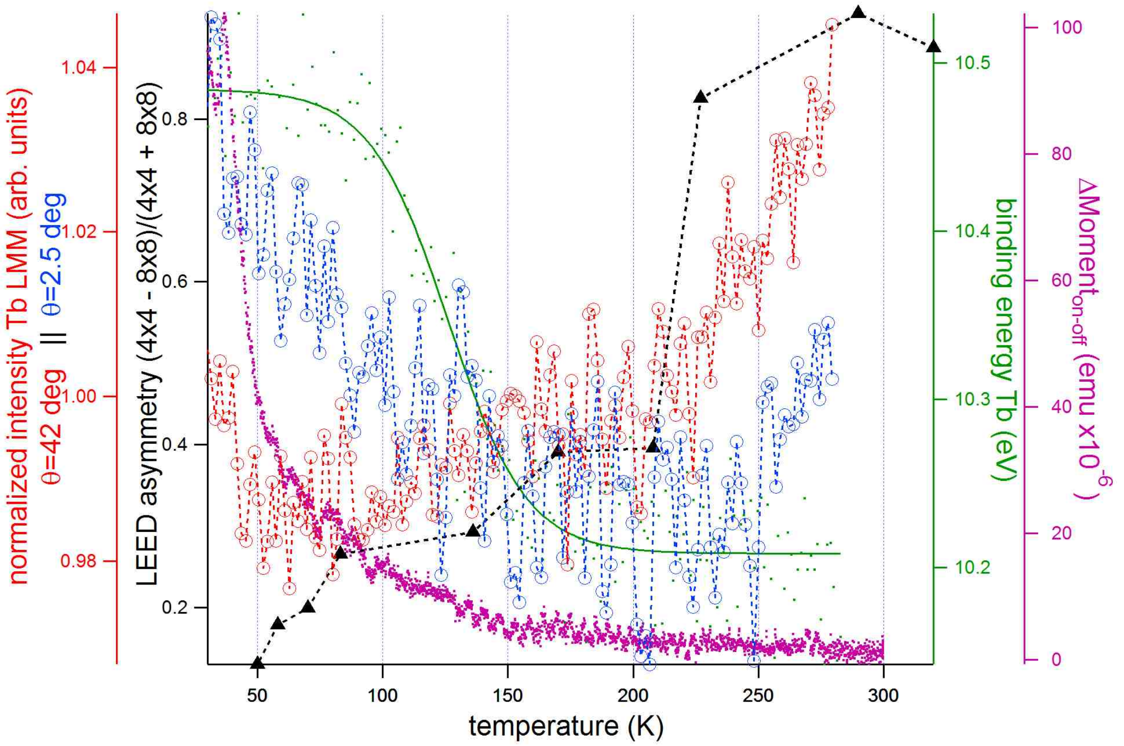

Figure 55: Combined plot for the different indications of changes in the molecular conformations: LEED asymmetry (black) between 4x4 and 8x8 superstructure intensity with a clear change between 210 K $< T <$ 240 K (discussed in Section 6.6.1); temperature dependent XPD scans in red (for $\theta = 42°$) and blue ($\theta = 2.5°$) showing the changes in scattering probability in the same temperature regime like the LEED asymmetry with additional changes for $T <$ 150 K (as discussed in Section 6.6.3); work function shift indicated by the Tb binding energy (in green) shows the same onset for changes as the temperature dependent XPD profiles for 170 K $> T >$ 80 K (discussed in Section 6.7) - all shown in Figure 53; now added: the difference of the magnetic moments caused by in-field and zero-field cooling measured during a warm-up cycle at $\mu_0 H = 7$ T (in magenta) with the same onset of change as the work function shift and the temperature dependent XPD profiles around $T \approx$ 170 K.

6.8.2. Angle scanned XPD at low temperature: Structural Analysis of $TbSc_2N@C_{80}$ on h-BN/Ni(111)

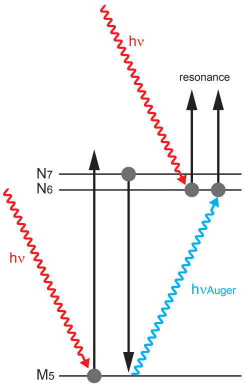

Figure 56: Schematic sketch to demonstrate the Auger transition leading to resonance with the Tb $4f_{5/2}$ photo electron.

To strengthen the argumentation for transition temperatures of $TbSc_2N@C_{80}$ further structural analysis was performed using angle scanned XPD. At temperatures $T = 30$ K where the system is immobilized in all degrees of freedom the structure should be comparable with simulations using the EDAC multiple scattering code [44].

To measure the Tb signal at a coverage of less than 6% of a monolayer Tb, compared to the h-BN/Ni(111) substrate, is a task that can be accessed by resonant XPS [134] and resonant XPD [135], as first demonstrated by Treier, *et al.* [50]. We took advantage of the resonant enhancement of the Tb MNN auger electron with the Tb $4f_{5/2}$ (sketched in Figure 56) to increase the signal intensity by roughly two orders of magnitude as shown in Figure 57a.

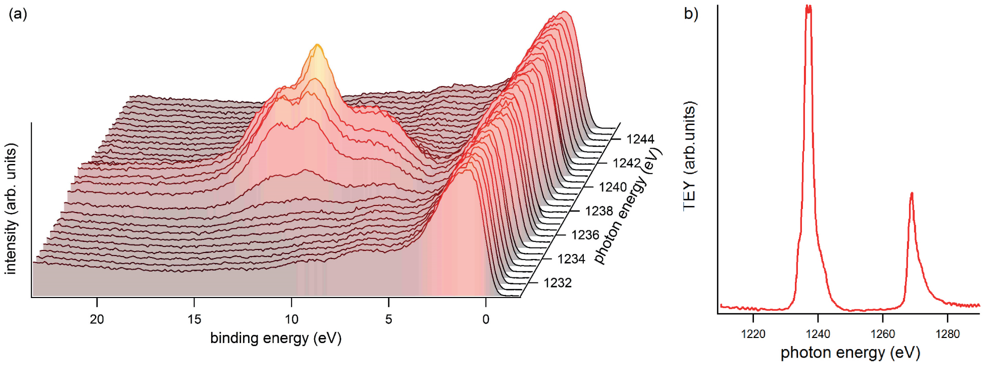

Figure 57: XPS scan in dependence of photon energy to find the best resonance: (a) scanning at different beam energies along the Tb M_4 absorption edge 1228 eV $\leq h\nu \leq$ 1248 eV to find the best resonant enhancement; (b) XAS taken at the Tb $M_{4,5}$ edge.

To find the resonance photon energy and measurement range for the elastic lines XPS spectra were taken of a binding energy regime of 24 eV $\geq E_B \geq -2$ eV, below the Fermi edge, while passing the photon energy through the Tb M_4 absorption edge (Figure 57b). This allowed to increase the signal to background ratio of the Tb MNN effect by orders of magnitude using the resonant enhancement of the Tb MNN auger electron with the Tb $4f_{5/2}$ photo electron. The strongest enhancement was found to be at a photon energy setting of $h\nu = 1237.9$ eV and a kinetic energy of $E_{kin} = 1215.1$ eV, corresponding to $E_B \approx 11$ eV. To reduce background effects that may arise from the Ni fcc(111) substrate, the energy windows of the rXPD were alternating measured on-resonance ($h\nu = 1237.9$ eV) and off-resonance ($h\nu = 1234$ eV) for each polar (θ) and azimuthal (ϕ) manipulator angle setting at the same binding energy regime in order to allow simple background subtraction.
DFT calculations resulted that the lanthanides within lanthanide-nitride endofullerenes favor positions where hexagons and pentagons meet [126, 131]: the so called (6,5)-sites. The C_{80}-I_h isomer has 60 pentagon-hexagon-hexagon sites for carbon positions ((6,5) sites) and thus 60 favored positions pointing to the carbon atoms and 60 possible positions pointing to the C-C bond.

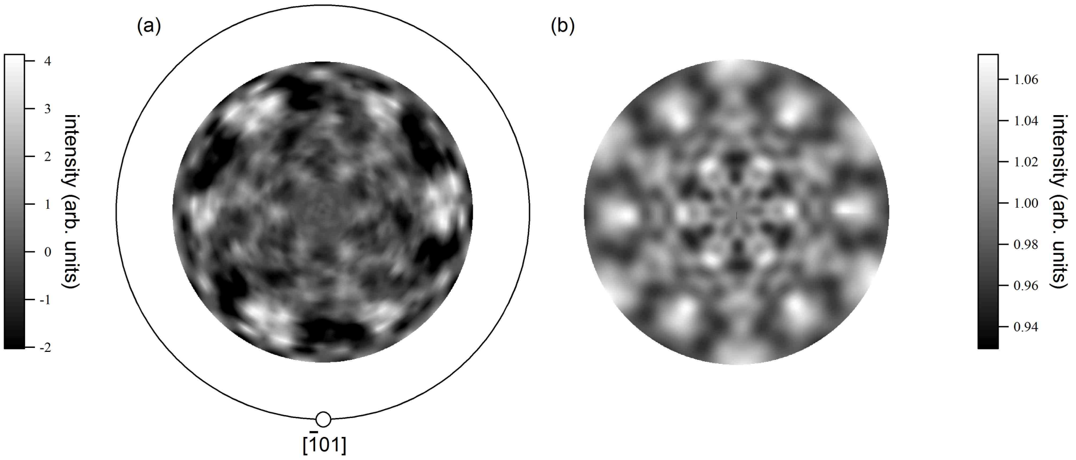

Figure 58: (a) resonant XPD of the Tb MNN auger, taken at $T = 30$ K at a photon energy $h\nu = 1237.9$ eV, 3 fold symmetry averaged. The ring indicates the polar angle $\theta = 90°$ position; (b) Simulation using the EDAC code as a sum of 16 single simulations; both shown for polar angles $\theta \leq 70°$.

Combinations of multiple scattering simulations using the EDAC code [44] in order to access the best-agreement between experiment and simulation resulted in a favored position of the Tb atoms pointing towards the C atoms of the (6,5) positions (in C_s conformation) in the lower hemisphere towards the h-BN/Ni(111) substrate as sketched in Figure 59 in side-view (left) and top view (right). The combinations base on all 120 possible Tb positions [123] assuming that in the frozen state at $T = 30$ K the Tb atom is positioned in a state of minimal enthalpy. The sum of the simulations resulting in the best agreement is shown in Figure 58b and shows all main features of the experimental data in Figure 58a in the right angle regime. All single simulations and the isotropic cases are shown in Appendix D

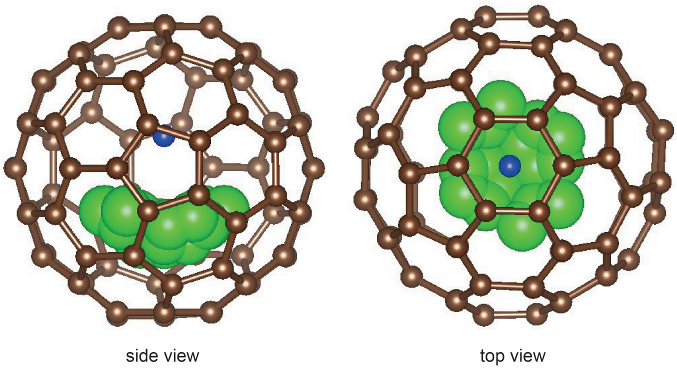

Figure 59: The 16 Tb positions for the EDAC simulation shown in Figure 58b: The Tb atoms always point towards the (6,5) position in the lower hemisphere towards the substrate; brown: carbon atoms, blue: nitrogen atom, green: all Tb positions.

Figure 60 shows the simulations for in-plane (parallel to the surface) orientation of the N-Tb axis (Figure 60a-c) and the case of Tb pointing away from the substrate. In all cases the same normalizations were done (phi averaged and 3-fold symmetry) to compare to the measurement shown in Figure 58a. In neither case the forward scattering maxima directions, as observed in the experiment, could be reproduced.
This indicates a different arrangement compared to the findings for $Dy_2ScN@C_{80}$ on Rh(111) where the endohedral triangle follows the substrate [116], and leads to the suspect of an interaction between the Ni(111) substrate and the endohedral unit. This is consistent with the findings of $TbPc_2$ on Ni films where a strong magnetic coupling between the SMM and the substrate could be verified [136].
Linear dichroism was measured at $T = 30$ K to further investigate the difference between $TbSc_2N@C_{80}/h$-BN/Ni(111) and $Dy_2ScN@C_{80}$/Rh(111). XAS measurements using horizontally linear polarized light were taken at different incidence angles as shown in Figure 61a. No angle dependence in spectral shape or intensity could be observed in the total electron yield as it could be expected for an in-plane conformation [116].

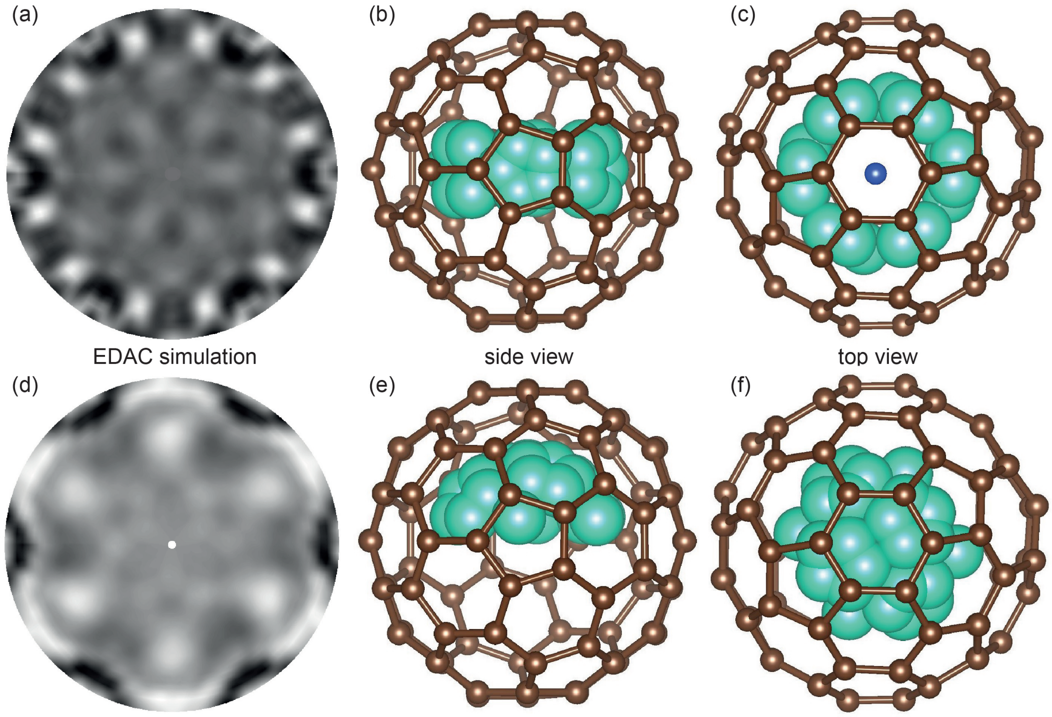

Figure 60: EDAC simulations for different Tb positions, in all cases the Tb points towards the (6,5) side ($\theta \leq 70°$): (a) in-plane case with the N-Tb axis being parallel to the sample surface with sketches in side view (b) and top view(c); (d)-(f) analogous for the case of Tb pointing away from the sample.

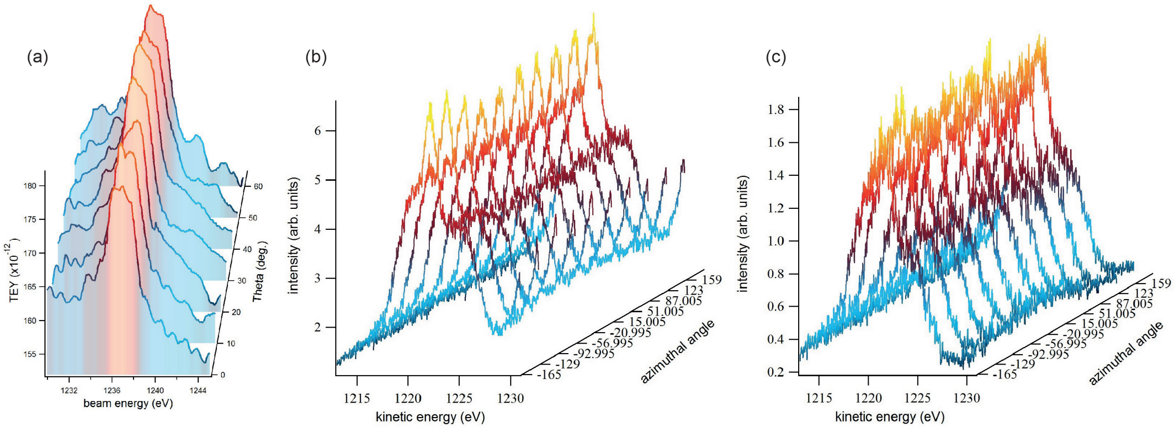

Figure 61: No dependence on incidence angles of the linear polarized beam: (a) XAS taken at different incidence angles; (b) resonance of the Tb MNN taken at different azimuthal angles at 60° incidence angle; (c) at 0° incidence angle.

As an additional indication for the absence of in-plane alignment of the Tb 4f orbitals the rXPS spectra taken at both 60° and normal incidence angle are shown in Figure 61b and c, respectively. A variation of about 2% can be observed that can be attributed to origin from a slightly inhomogeneous distribution of the molecules on the surface of the h-BN/Ni(111) substrate. This is consistently observed in the XPD patterns. Thus we suggest that the f-orbitals are aligned in more than 2 dimensions supporting the result of the EDAC simulations.

To additionally confirm the Tb positions as determined from XPD (Figure 59) within the cluster, EDAC calculations were performed using the same Tb positions along the (6,5) positions for 80 emitting C1s atoms of the cage in order to compare to the C1s XPD taken at $T = 30$ K.

Figure 62a shows the stereographic map of the C1s XPD pattern taken at a photon energy of $h\nu = 600$ eV and thus a kinetic energy of $E_{kin} \approx 290$ eV compared to the EDAC simulation based on the findings for the Tb rXPD as described above. The sum of 16 multiple-scattering simulations with the Tb atom pointing in the (6,5) positions of the lower hemisphere (see Figure 59) resulted again in the best-agreement simulation: All structural main features could be reproduced at the polar and azimuthal angle positions.

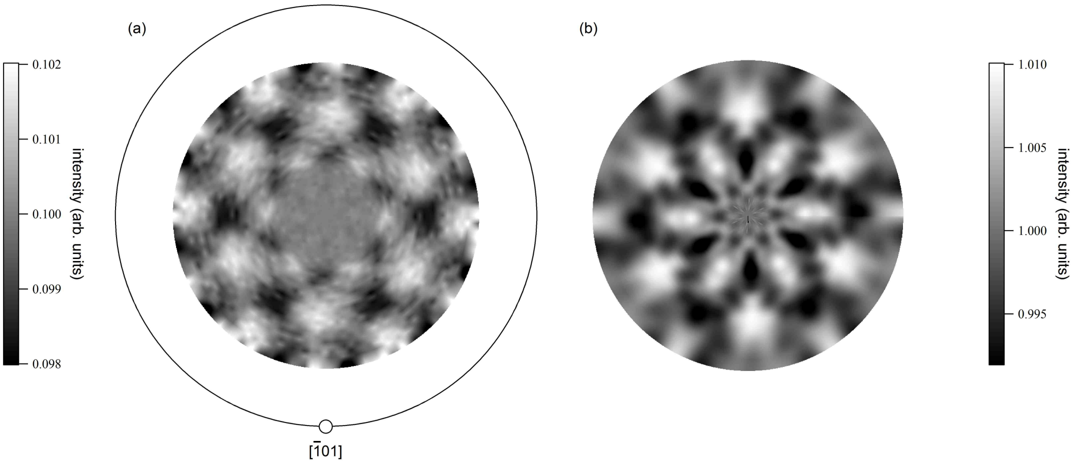

Figure 62: XPD stereographic map of the C1s elastic line taken at $h\nu = 600$ eV at $T = 30$ K, showing the inner 70 degree, 6 fold-averaged, the circle indicates the 90° polar angle; (b) best agreement simulation as a sum of 16 single EDAC simulations.

6.9. Temperature dependent angle scanned XPD of TbSc$_2$N@C$_{80}$ on h-BN/Ni(111)

To strengthen the argumentation on the two rotational degrees of freedom for the C$_{80}$ cage and the endohedral unit and their threshold temperatures, XPD measurements were performed at different temperatures for all molecular components.

For the case of the C1s signal, where 6-fold averaging is legitime due to the 2-fold symmetry of the icosahedral molecule with hexagon towards top, in combination with the 3-fold symmetry, due to the substrate, we chose temperatures which were clearly distinct by the different measurements: $T = 30$ K (Fig. 63a) at a temperature where no molecular motion - neither endohedral nor of the cage is expected; at an intermediate temperature $T = 185$ K (Fig.63b) which should be below the onset of the carbon cage motion and room temperature $T = 300$ K (Fig. 63c) where both endohedral unit and carbon cage are expected to be in motion.

Comparing the the patterns between the measurement at $T = 30$ K (Figure 63a) and $T = 185$ K (Figure 63b) no difference in structure and only minor changes in anisotropy are observed. A blurring effect of the structural patterns can be accounted for thermal effects and the influence of a mobile endohedral unit inside the carbon cage. In comparison the measurement taken at room temperature (Figure 63c) shows a clear decrease in anisotropy, if compared to the other stereographic maps.

To visualize the effect of the changes we take the asymmetries between the intensities following

$$A = \frac{I_{T_1} - I_{T_2}}{\sum\limits_{i=1,2} I_{T_i}}, \tag{34}$$

as shown in Figure 64. Here we use as convention that T_1 corresponds to the lower temperature (and T_2 for the higher temperature) of the asymmetry. The color code shows white for no change, blue for a positive value and thus more scattering (and structural effects) at the lower temperature. Analogously red indicates a tendency towards more scattering in the patterns measured at the higher temperature T_2.

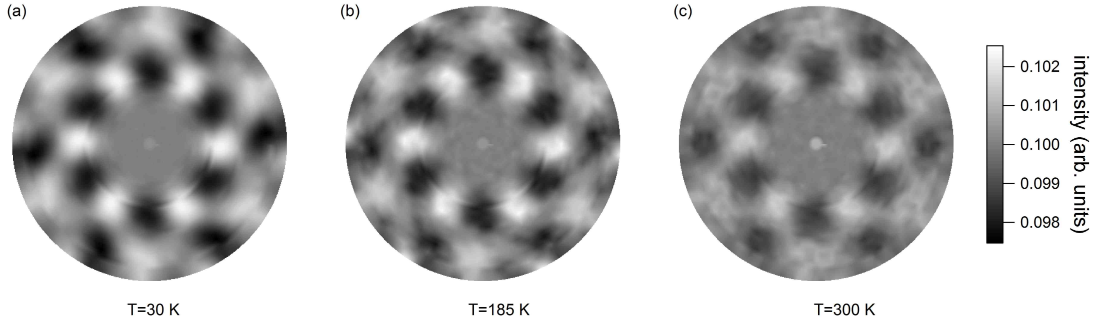

Figure 63: C1s XPD stereographic maps taken at $h\nu = 800$ eV, shown for polar angles $\theta \leq 60°$, 6-fold averaged: a) T=30K, b) T=185 K c) T=300 K.

The asymmetry map of $T_1 = 30$ K and $T_2 = 185$ K indicates the absence of structural change for polar angles $\theta < 55°$, as shown in Figure 64a. The decrease of the 6 forward scattering peaks at $\theta = 57°$ can be accounted to arise from the mobility of the endohedral unit, though the absence of changes in the inner polar angles shows the immobility of the carbon cage for $T = 185$ K.

Stronger changes in the asymmetry between the stereographic projections of $T_1 = 185$ K and $T_2 = 300$ K are observed: The 6-fold symmetric structure around $\theta = 30°$ which follows the [110] lattice direction of the substrate diminishes while the areas azimuthally rotated between the spots show stronger effects at room temperature. The signal is smearing out on the entire azimuth of the polar coordinates. For the case of the expected carbon cage rotation around the z-axis a decrease in forward scattering at the C atoms and thus a decrease in the asymmetry is in perfect agreement like the increase of the scattering along the azimuths between the forward scattering features at lower temperatures.

To visualize the effect more, azimuthal cuts were taken through the stereographic maps (Figure 63) and are shown in Figure 65a. The decrease of anisotropic change in going from $T = 30$ K (blue) to $T = 300$ K (red) is much stronger compared to the changes between $T = 30$ K and $T = 185$ K. The asymmetries shown in Figure 65b base on Formula 34 and verify that a faint anisotropy change can be observed in the asymmetry between $T_1 = 30$ K and $T_2 = 185$ K, compared to a ten times stronger effect in the asymmetry between intermediate temperature ($T_1 = 185$ K) and room temperature ($T_2 = 300$ K).

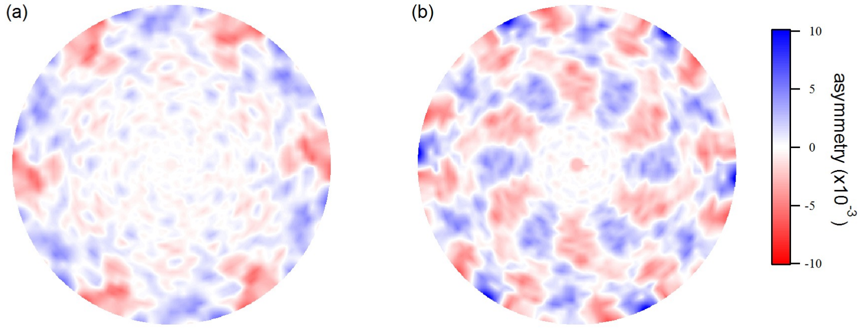

Figure 64: Asymmetry maps of the C1s XPDs - shown are the inner 60 degree of polar angles: a) Asymmetry between $T = 30$ K and $T = 185$ K (30-185) - b) asymmetry between $T = 185$ K and $T = 300$ K; red (blue) indicates an increased forward scattering for the higher (lower) temperature.

This is strongly strengthening the picutre of the onset of rotational motion around the z-axis can be narrowed down to 185 K $< T_{trans} <$ 300 K. It is consistent with the transition temperature observed for the superstructure in temperature dependent LEED measurements $T \approx 210$ K and the higher temperature for a trend change in temperature dependent XPD measurements $T \approx 210$ K, as described in Chapter 6.6.1. We can conclude that the motional onset for the C1s cage is around a temperature of $T \approx 210$ K. Considering we still see a preferred structure of the top hexagon at $T = 300$ K (Fig. 63c) a higher temperature is expected to be required to put all carbon cages into constant rotational motion.

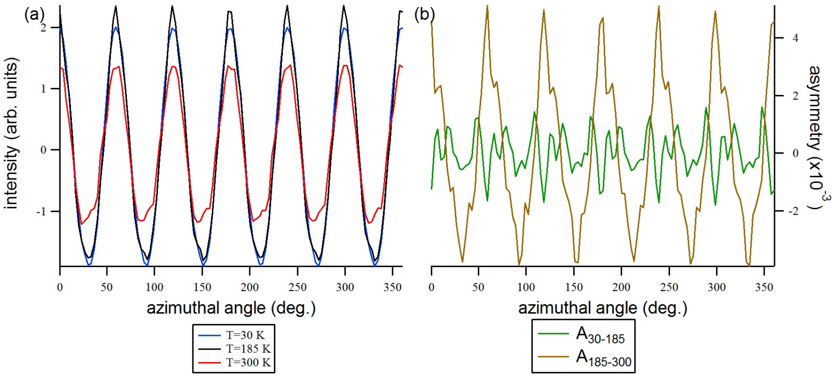

Figure 65: a)Azimuthal cuts at a polar angle of $\theta = 38°$ at the different temperatures $T = 30$ K, 185 K, 300 K as shown in Figure 63 (blue, black, red respectively) - b) Cuts through the asymmetry maps in Fig. 64.

N1s signal: The separation of the N1s elastic lines of h-BN and $TbSc_2N@C_{80}$ allows to take XPD measurements of the endohedral nitrogen signal. To investigate the temperature dependent structural changes in $TbSc_2N@C_{80}$/h-BN/Ni(111) XPD measurements were taken at the same temperatures like for C1s in order to allow comparison and to measure off the transition temperatures: $T = 30$ K where no motion is expected (Figure 66a), $T = 185$ K where the endohedral unit is in motion and the carbon cage immobilized (Figure 66b) and room temperature $T = 300$ K where the carbon cages are free to rotate (Figure 66c).

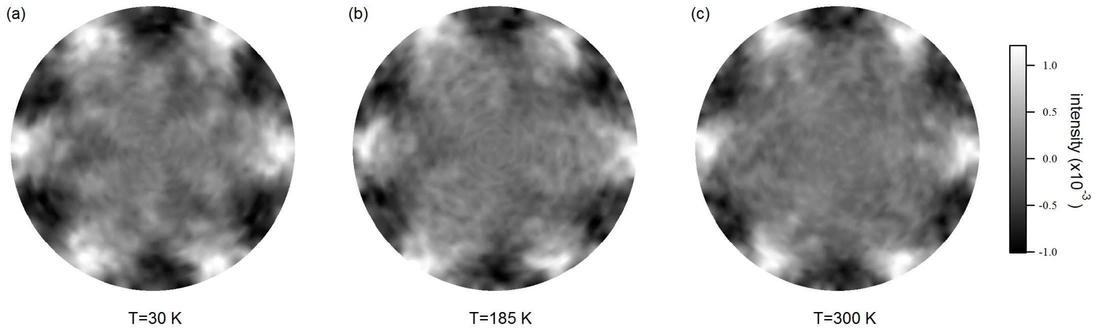

Figure 66: XPD N1s for polar angles $\theta \leq 70°$; 3-fold averaged a) $T = 30$ K b) $T = 185$ K c) $T = 300$ K.

To compensate for an imperfect distribution of $TbSc_2N@C_{80}$ on the substrate a sine was fitted for each polar angle with the same azimuthal phase and frequency (of $f = \frac{1}{2\pi}$) to substract the background. The features of the immobilized molecules around $\theta = 60°$ and $\theta = 42°$ arise from scattering effects with the C1s cage. The smaller 3-fold structure

and the 6 forward scattering peaks visible at $T = 30$ K (Figure 66) around $\theta = 42°$ arise from scattering with the top hexagon of the immobile C_{80} cage.
With increasing temperature to $T = 185$ K (Figure 66b) a strong "smearing" effect of the inner structure is observed which indicates a motion of the endohedral nitrogen as emitter. This can be explained by the picture that the N1*s* emitter can be expected to be delocalized around the center of the carbon cage once the endohedral unit unfreezes. At room temperature (Figure 66c) no inner structure can be resolved anymore which is consistent with the observed motional onset of the C_{80} cage as shown in Figure 63. Even though we do not expect all C_{80} cages to be in motion at room temperature the anisotropy would drop further. The faint inner structure with low anisotropy at $\theta = 42°$ for lower temperatures disappears in the background.

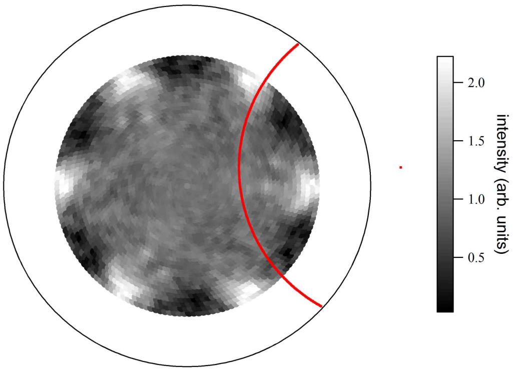

Figure 67: XPD N1s at $T = 300$ K as shown in Figure 66c, 3 fold-averaged; the red line visualizes the visible diffraction ring.

Three faint arcs appear, as visualized in Figure 67, which are suggested to arise from backscattering with the *h*-BN layer as they are opposing to the *h*-BN diffraction rings measured in-plane as forward scattering and shown in Figure 29c. The remaining signal at $\theta = 60°$ shows a lower asymmetry than at lower temperatures which is consistent with the picture that not all molecules are in constant rotational cage-motion at room temperature.
Figure 68a shows the stereographic map of the N1s signal at $T = 30$ K with enhanced contrast. The forward scattering signals of the cage at $\theta = 50°$ are still visible in the stereographic map. The inner structure shows higher contrast and visualizes the 3-fold character of the signal.
To visualize the structural changes for $TbSc_2N@C_{80}$/*h*-BN/Ni(111) at different temperatures, asymmetries of for $\theta < 52°$ are investigated, following Formula 34, similar as discussed in Chapter 6.8.2 for the case of the C1s signal.
Figure 68b shows the asymmetry between $T_1 = 30$ K and $T_2 = 185$ K: Blue stands for a loss in structural information when increasing the temperature while red stands for an increase of structural influence. The strongest effect is reduced scattering at the position

of three of the top-hexagon scattering cones as marked in Figure 68 a-c with a green dashed circle. Also a reduction of the 60° rotated signatures at the same azimuthal angle is visible but fainter. The N1s atom is centralized in the C_{80} carbon cage with a slight dislocation and thus no strong movement is expected after motional onset. We suggest a motion on the surface of a dislocation sphere from the center in dependence on the (6,5) positions of the Tb and Sc atoms what explains the faint effect and washed out changes in the asymmetry.

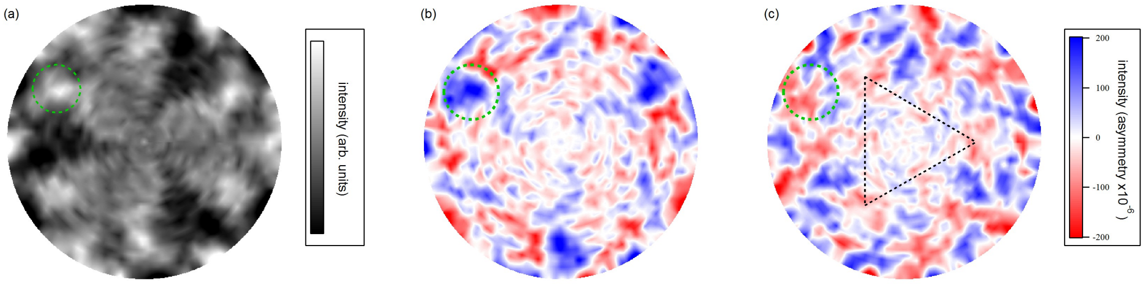

Figure 68: Visualization of changes: a) N1s stereographic map for $\theta \leq 50°$ at $T = 30$ K; b) Asymmetry between $T = 30$ K and $T = 185$ K; c) Asymmetry between $T = 185$ K and $T = 300$ K.

In the asymmetry plot between $T_1 = 185$ K and room temperature $T_2 = 300$ K the complementary three positions of the same azimuth (rotated by 60° at $\theta = 42°$) show signal loss and the remaining azimuthal angles along this polar angle show an increased forward scattering what is consistent with the onset of the cage motion considering the carbon atoms of the top hexagons are statistically more distributed along the same cone. A faint fcc(111) structure arises which may origin from backscattering from the substrate: the [110] and equivalent directions are hinted with the black dashed triangle at $\theta = 32°$.

Tb signal: Additionally, rXPD measurements were taken of the Tb MNN transition at the same three temperatures as for the C1s (Figure 63) and the N1s (Figure 66) signal, as shown in Figure 69: At the lowest temperature of $T = 30$ K where the endohedral unit is aligned towards the (6,5) positions of the lower hemisphere as discussed in Section 6.8.2 and both endohedral unit and cage are immobilized, at the intermediate temperature of $T = 185$ K, where the endohedral unit is in motion within an immobilized carbon cage and at room temperature where also the cage has the option to be in rotational motion around the z-axis perpendicular to the sample surface.
The stereographic map taken at $T = 30$ K (Figure 69a) shows a clear structure of scattering peaks as discussed in Section 6.8.2 and can be reproduced by a sum of simulations with immobilized endohedral units.
At $T = 185$ K (Figure 69b) where endohedral motion is expected, no clear scattering

peaks are (contrary to $T = 30$ K) observed and instead diffuse rings are observed as 3-fold structure following the substrate into the ⟨110⟩ direction. An additional set of rings is rotated by 60° but fainter and a different polar angle. This diffuse structure could be due to endohedral motion as the Tb hops between the (6,5) positions and further fades out $T = 300$ K at lower anisotropy.

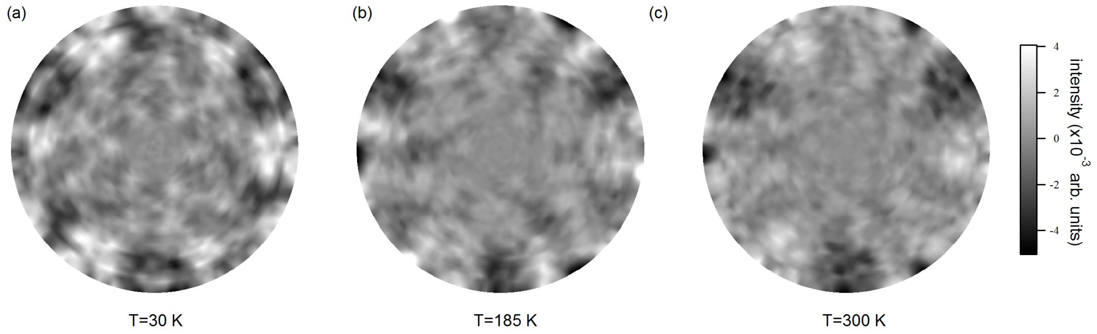

Figure 69: resonant XPD Tb MNN after sinus background subtraction up to 70 degree; 3-folded a) T=30K b) T=185 K c) T=300 K.

This fits into the picture of an onset on endohedral movement at the transition temperature $T = 50$ K positioned between the measured $T = 30$ K and $T = 185$ K and the onset of cage rotation at $T = 210$ K.

6.10. Conclusions and Outlook

Highly purified $\mathrm{TbSc_2N@C_{80}}$ evaporated at a temperature of $T \approx 800$ K on a substrate of *h*-BN/Ni(111) at a substrate temperature of $T \approx 450$ K forms a 4x4 superstructure. The substrate temperature allows the molecules to have enough energy to form connecting islands and to grow Frank-van-der-Merwe growth like, LEED and XPS investigations suggest that molecules can move with respect to each other, so that the second layer molecules may find voids and island borders to combine with the the first layer. Additionally they are free to align in a way that the $\mathrm{TbSc_2N@C_{80}}$ layer orients following the [110] direction of the *h*-BN/Ni(111) substrate in form of large single-domains. This can consistently be verified by LEED, STM and XPD measurements.

At room temperature the molecules lost their translation movement and are reduced to a rotational motion along the z-axis perpendicular to the substrate surface for the C_{80} cage with a hexagon pointing towards the substrate and towards the surface. The endohedral unit is in an independent three dimensional motion where the Tb and Sc atoms "hop" from one (6,5) position to the next pointing to the C atoms of the carbon cage. At $T = 300$ K the thermal energy appears not to be high enough to increase the hopping rate of the C_{80} cages enough to mimic a permanent rotation of all molecules as shown by XPD measurements of the carbon cage and verified for other molecular components.

Reduction of the temperature towards $T = 185$ K decreases the rate of molecular rotation until the motion of the C_{80} cage entirely freezes around $T = 230$ K. An 8x8 superstructure forms in addition to the 4x4 superstructure. Here four molecules combine to a larger supercell due to the three different alignments of the C_{80}-I_h icosahedral cage symmetry which can form patches of four molecules. An increased forward scattering is observed in XPD stereographic maps of the C1*s* signal and intra-molecular structure can be resolved using scanning tunneling microscopy. The endohedral unit continues its three dimensional rotational hopping along the (6,5) positions at an unchanged hopping rate.

Further reduction of the temperature reduces the hopping rate of the endohedral unit as there is less 'activation' energy to leave an energetic favorable position. The most favorable alignment of the endohedral unit appears to be with the Tb atom pointing towards the (6,5) sites of the lower hemisphere, as observed with low temperature XPD measurements. The total dipole moment is not isotropically distributed anymore and causes a decrease in work function for the entire system for a temperature range $170 \text{ K} > T > 80 \text{ K}$. This effect is visualized by a shift of the elastic lines for all molecular components in the order of $\Delta E \approx 250$ meV towards a higher binding energy.

Magnetization measurements of powder samples of $TbSc_2N@C_{80}$ taken during heat ramps after in-field cooling at an external magnetic field of $\mu_0 H = 7$ T, compared to zero-field ($\mu_0 H < 1$ mT) cooling, show a difference in magnetic moments. This indicates that not all molecules are aligned by the external magnetic field and this effect appears to become stronger at lower temperatures. This picture is consistent with the insight given by temperature scanned XPD profiles along the polar emission angles $0° < \theta < 45°$. A change in forward scattering probability shows a change in hopping rate.

The work function decreases in dependence of the temperature and turns constant around $T = 70$ K indicating that a statistical majority of the endohedral units align towards the (6,5) positions close to the substrate. Around $T = 50$ K the endohedral unit turns immobilized as also hinted by an increased difference of in-field and zero-field cooled measurements of the magnetic moment in dependence of the temperature.

The frozen Nitride clusters remain in a state of minimal enthalpy with the Tb atom pointing into a (6,5) position in the lower hemisphere towards the Ni(111) substrate. This was verified in a structural analysis using EDAC simulations in comparison with resonant XPD measurements of the Tb MNN transition as well as for XPD measurements of all molecular components. The difference in magnetic moment (comparison of a powder sample in-field cooled compared to a zero-field cooled) shows an increased magnetization difference towards minimal temperature of $T = 1.8$ K, which may originate from the aligned magnetic moments, compared to randomly oriented magnetic moments in the zero-field cooled case. This suggests the freezing point of the endohedral unit being positioned around $50 \text{ K} < T < 70 \text{ K}$. A powder sample does not have the surface influence of a submonolayer of $TbSc_2N@C_{80}$ on *h*-BN/Ni(111) and thus the freezing point of the endohedral unit should be expected at the lower part of this range for the case of $TbSc_2N@C_{80}$/*h*-BN/Ni(111) .

All Effects, as the motional onsets of both endohedral unit and C_{80} cage as well as the work function shift, are reversible and can be reproduced with the same substrate several times. Changes in the density of states of single molecules as found using LT scanning tunneling microscopy indicate the possibilities to manipulate the endohedral units. Given the long relaxation times of some metallofullerenes, the size of roughly $d \leq 1$ nm and that they are additionally screened by a highly stable carbon cage of 80 atoms makes this system a candidate for information storage and applications in the future.

A. Temperature calibration at the XP preparation chamber

The preparation chamber for the x-ray unit of the PEARL endstation (XP-chamber) has no direct temperature read out for the sample temperature. In order to calibrate the temperature several cycles with additionally attached thermocouples (K-type) and pyrometer (Maurer) were performed.

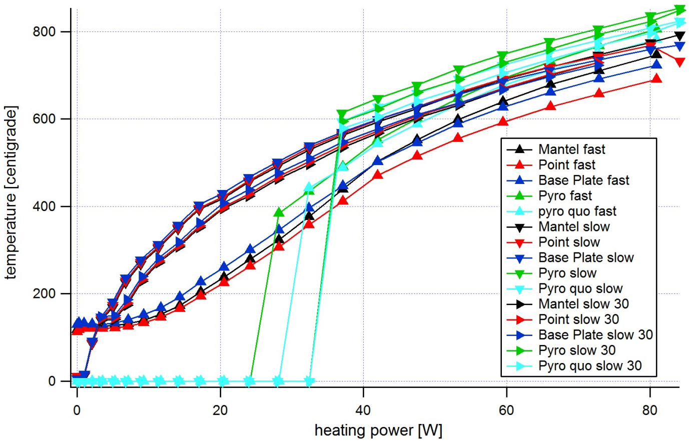

Figure 70: Temperature calibration of the XP chamber.

In Figure 70 three sets of calibrations are shown using a mantle thermocouple introduced into a hole in a dummy sample, a point welded thermo couple (on the dummy sample), the heating stage base plate thermo couple and a Maurer two wavelengths pyrometer as sketched in Figure 71.

The three sets of measurements were taken at different time frames after adjusting the temperature by hand: "fast", "slow" and "slow 30" here stand for time frames of 10 s, 180 s and 30 s respectively.

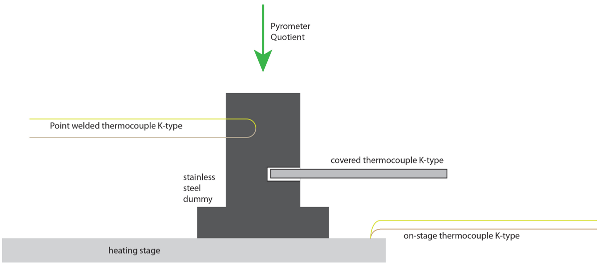

Figure 71: Schematic setup of the temperature calibration: 3 thermocouples K-type: Spot welded on the sample, positioned on the stage and introduced into the sample as a mantle thermo couple in addition to a Maurer 2-wavelengths pyrometer (Type QKTRD 1075).

B. Temperature dependent ordering of TbSc$_2$N@C$_{80}$ on h-BN/Ni(111)

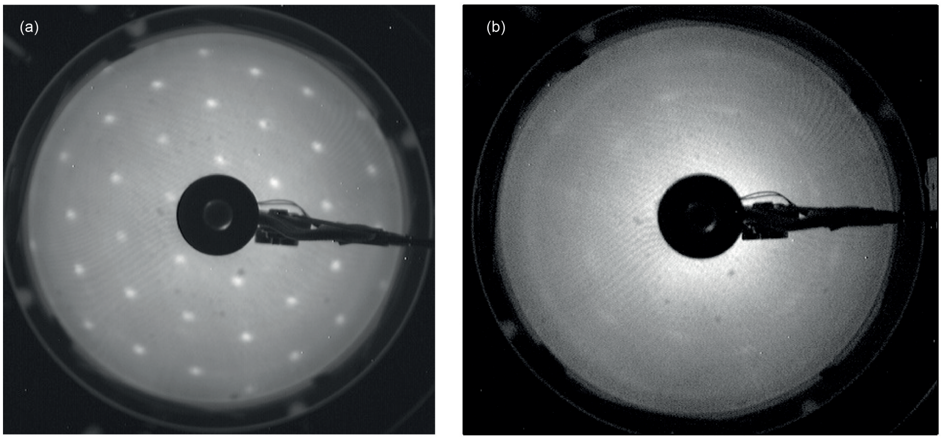

Figure 72: LEED images taken $E = 30$ eV after identical preperation parameters except substrate temperature: (a)substrate temperature $T = 450$ K (b) without heating of the sample (room temperature).

Comparison of preparations performed at different temperatures of the sample are shown in Figure 72. Room temperature preparations (Figure 72b) show strong disorder rings which indicate a vast amount of domains and no ordering of the molecules with respect to the substrate structure. Contrary, preparations performed during a substrate counterheating at $T > 450$ K show a very clear ordering of the molecules at the absence of disordering rings. Both preparations have a comparable coverage as shown in Figure 73. The ratio between intensity of the N1s (h-BN) and the N1s (TbSc$_2$N@C$_{80}$) elastic lines is 0.07 for Preparation a, compared to 0.08 for Preparation b.

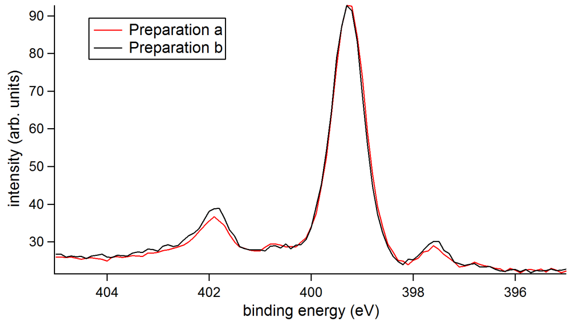

Figure 73: XPS measurements of the preparations shown in Figure 72 taken at $h\nu = 600$ eV; Preparation a and b correspond to Figure 72 (a) and (b).

C. *h*-BN XPD: Simulation

The XPD measurement of the N1s signal of *h*-BN/Ni(111) as shown in Figure 29c to characterize the substrate were verified with an EDAC simulation (4 substrate layers of Ni(111) with an *h*-BN layer on top as shown in Figure 74.

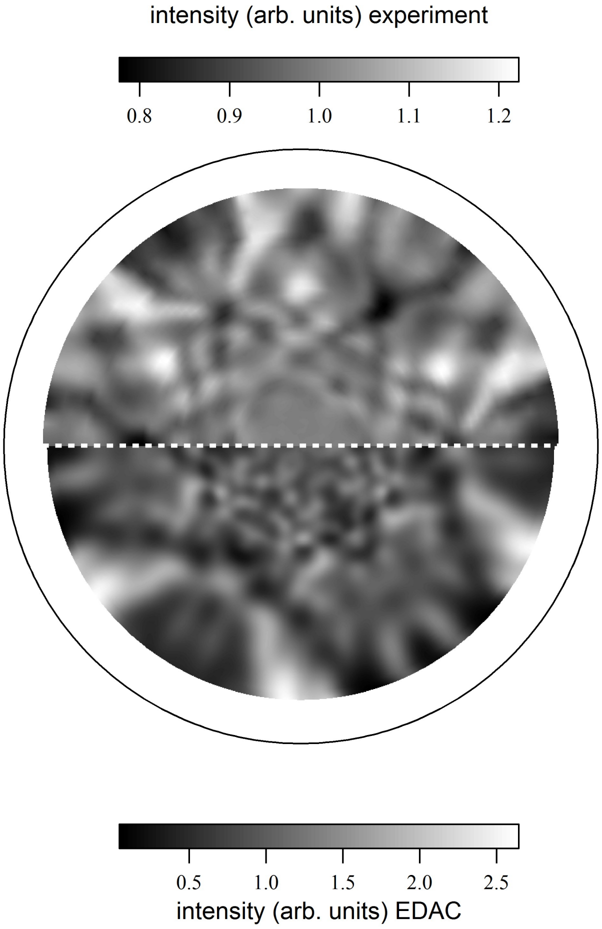

Figure 74: N1s signal of *h*-BN/Ni(111): Measurement as shown in Figure 29c on top; EDAC simulation on bottom; experiment was performed at room temperature and photon energy $h\nu = 600$ eV, simulation accordingly with a kinetic energy of of $E_K = 200$ eV.

Both, simulation and experiment, are in very good agreement. One major difference are the strong scatterers in the signal at polar angle $\theta = 56°$. While the feature is present in the simulation, it appears to be very energy dependent and could not be entirely reproduced.

D. Simulations of Tb conformations: C_s and C_3

For completeness in this section more simulations are shown which lead to the calculations as discussed in Section 6.8.2. All simulations were done using the EDAC code [44] and base on the two different energetic minima of the endohedral orientation as calculated by A. Seitsonnen [123] and A. Popov, *et al.* [137]. The calculated clusters were for $Y_3N@C_{80}$ as a good approximation for $TbSc_2N@C_{80}$.
The stereographic maps are 3-fold symmetrized to respect the surface symmetry and ϕ-averaged to compare with the evaluation method as described in Chapter 4.

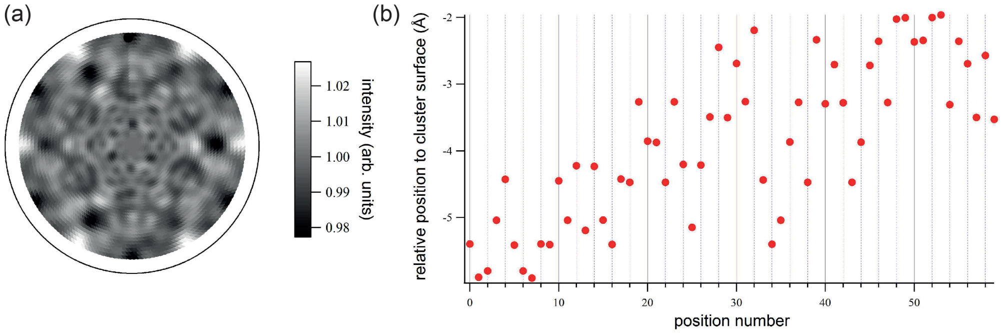

Figure 75: (a) Sum of 60 simulation of the C_s conformation of the icosahedral isomer; (b) position code with respect to the surface corresponding to the single simulations shown in Figures 79 to 82.

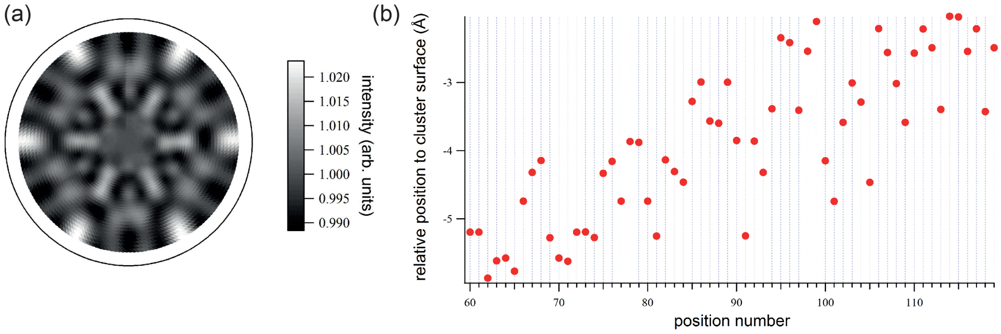

Figure 76: (a) Sum of 60 simulation of the C_3 conformation of the icosahedral isomer; (b) position code with respect to the surface corresponding to the single simulations shown in Figures 83 to 86.

Figure 75 and 76 show the sums of all calculated positions for the C_s and C_3 conformations, respectively. The sum of all different conformations is shown in Figure 76 and schematic sketches to visualize the clusters are shown in Figure 78. Figures 79 to 86 show all single simulations with corresponding relative z-coordinates as shown in Figures 75b and 76b.

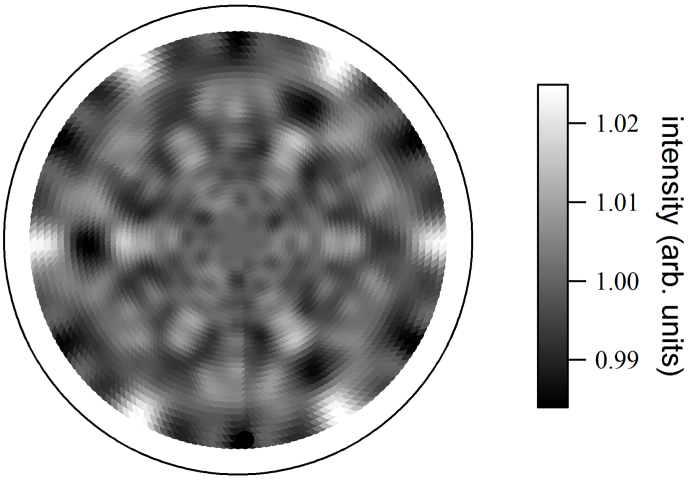

Figure 77: Sum of all 120 simulation of the C_3 and C_s conformation (the sum of Figure 75 and 76.

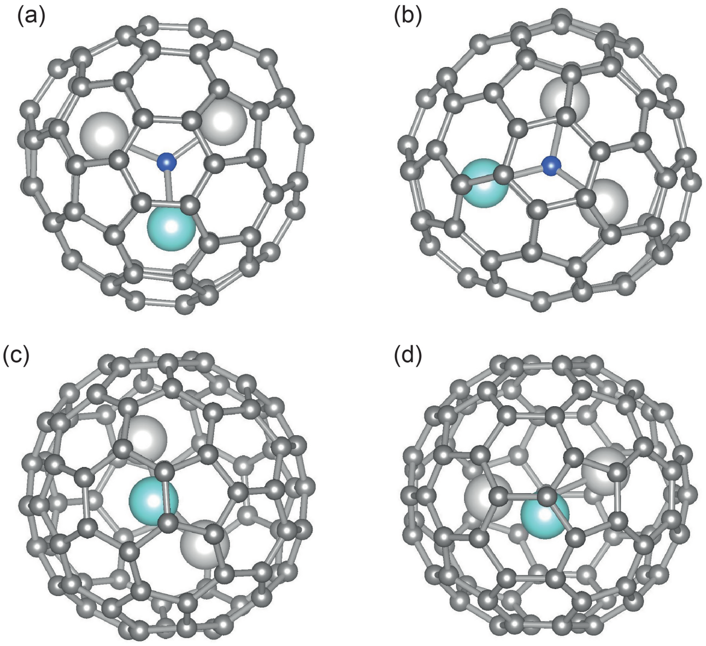

Figure 78: Different conformations of the calculated clusters: C_3 conformation ((a) and (c)) and C_s conformation ((b) and (d)) in top view ((a), (b)) and to visualize the atomic positions with respect to the carbon cage ((c), (d)).

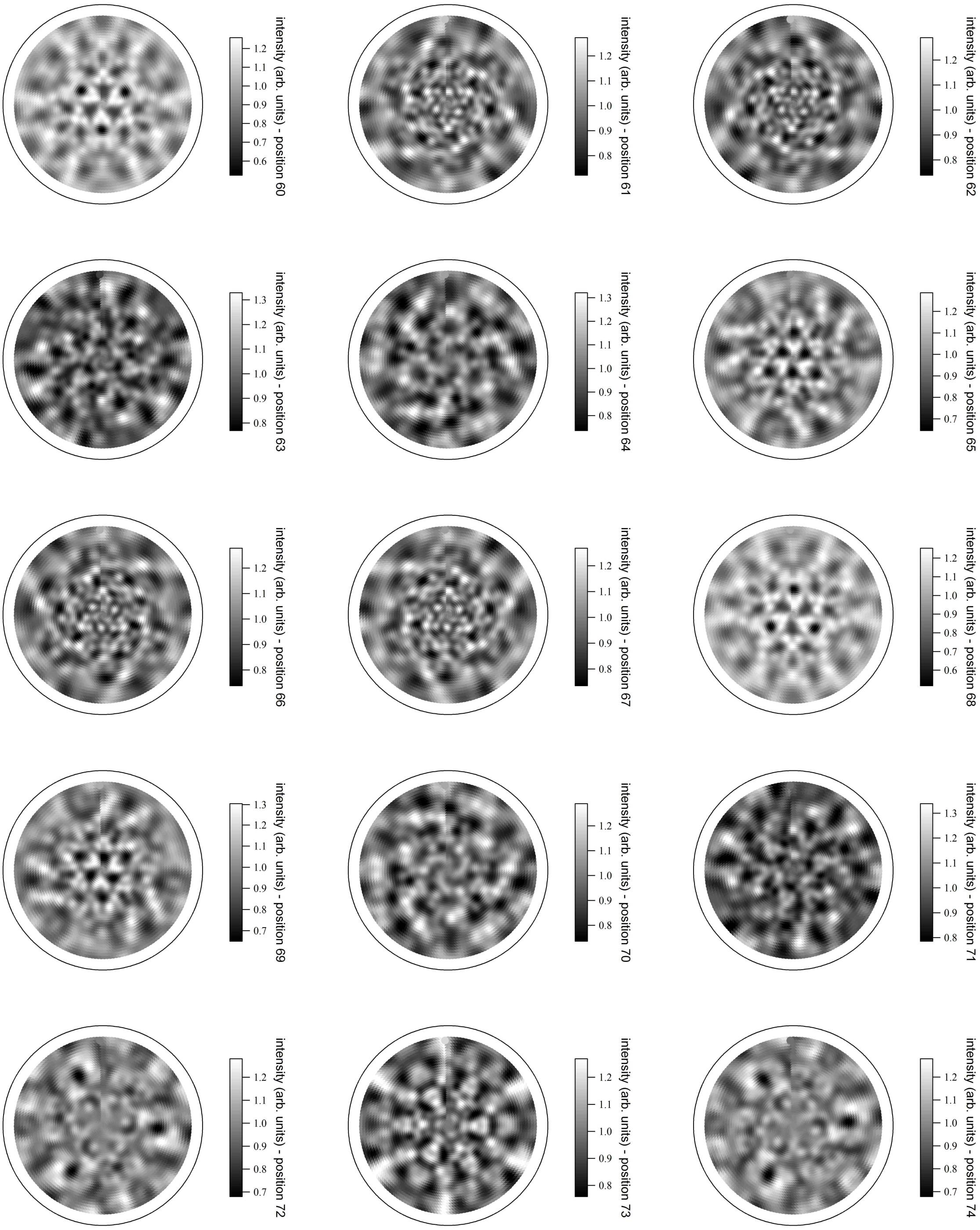

Figure 79: Single Simulation Sets (3-fold average and ϕ-averaged): 00 to 14.

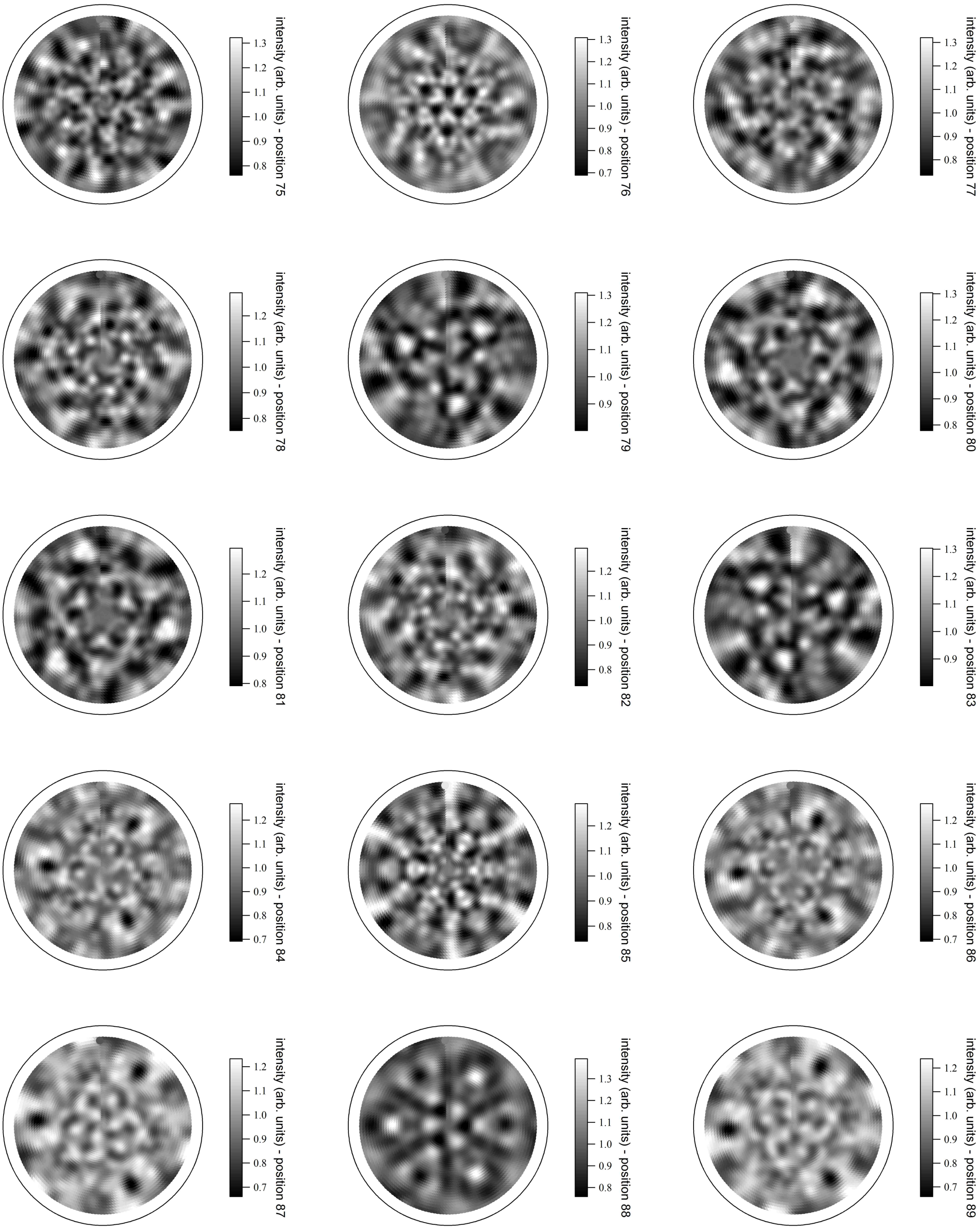

Figure 80: Single Simulation Sets (3-fold average and ϕ-averaged): 15 to 29.

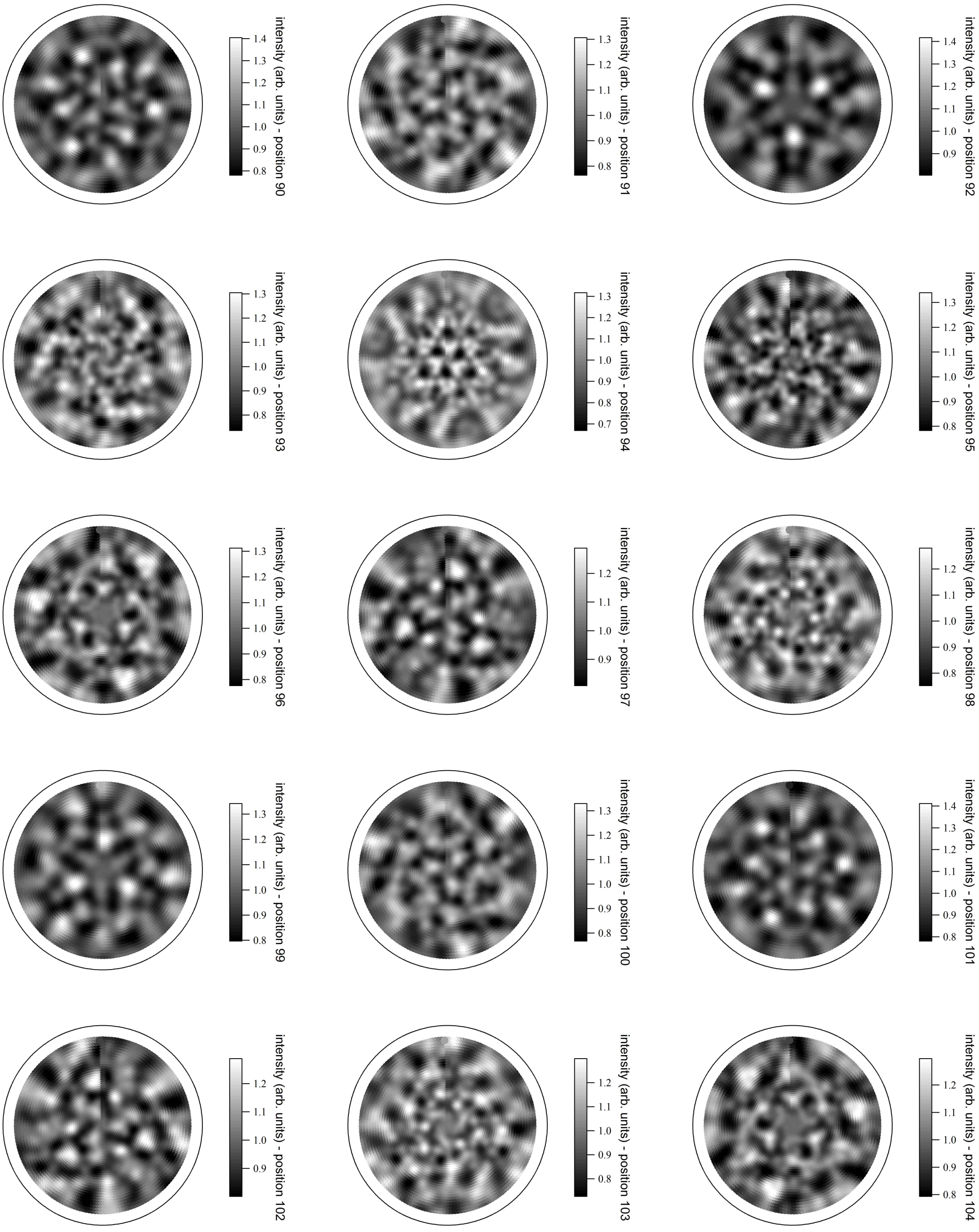

Figure 81: Single Simulation Sets (3-fold average and ϕ-averaged): 30 to 44.

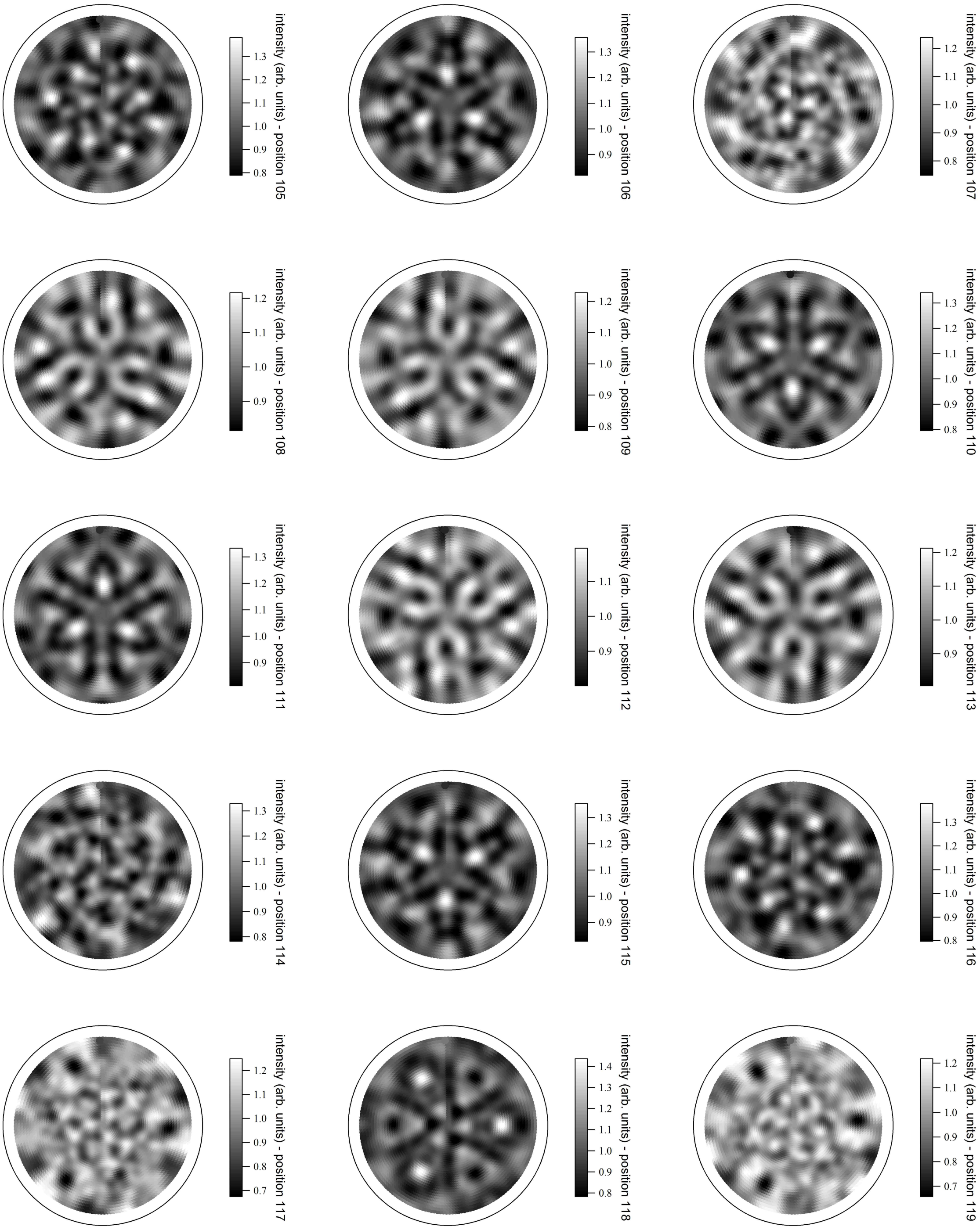

Figure 82: Single Simulation Sets (3-fold average and ϕ-averaged): 45 to 59.

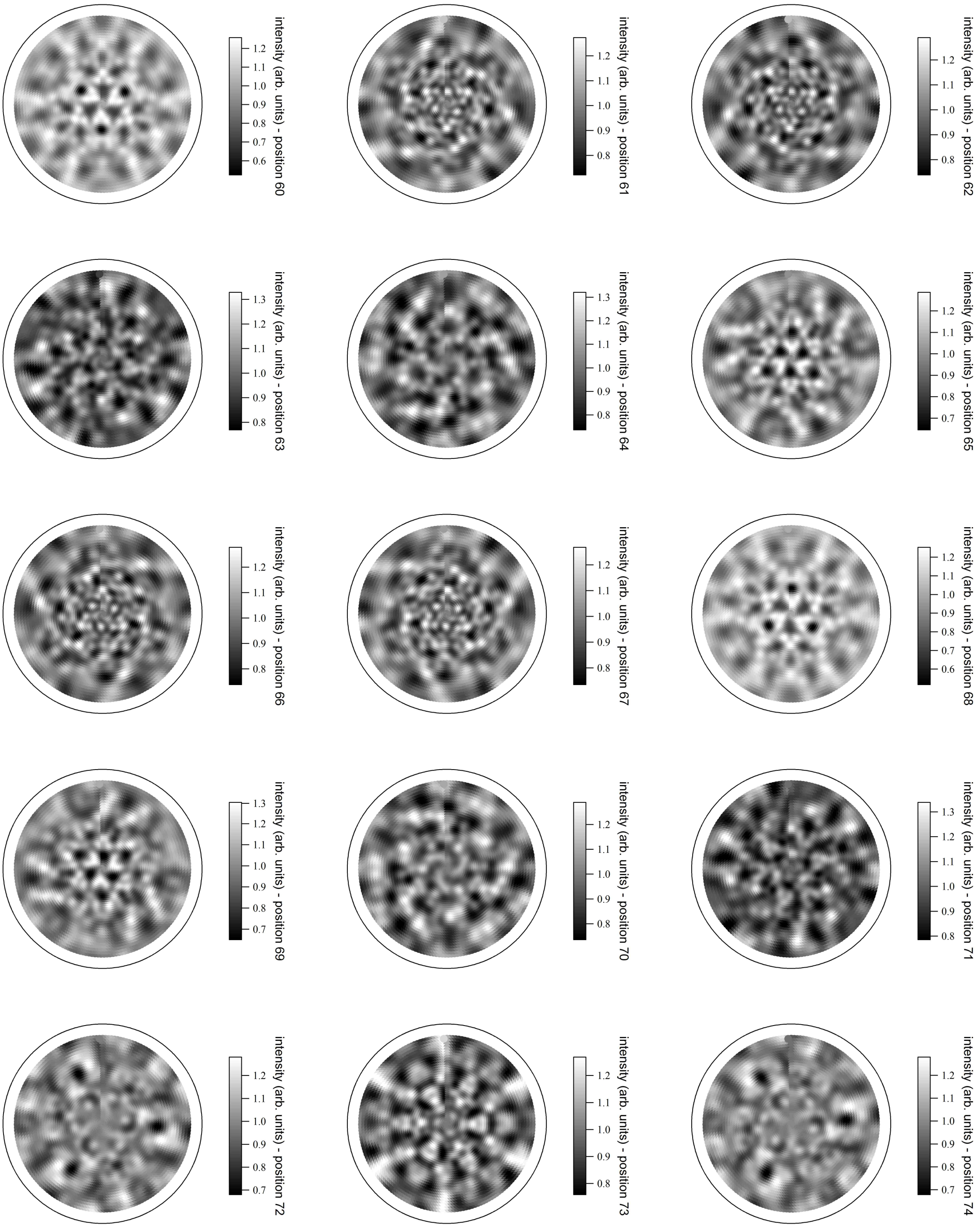

Figure 83: Single Simulation Sets (3-fold average and ϕ-averaged): 60 to 74.

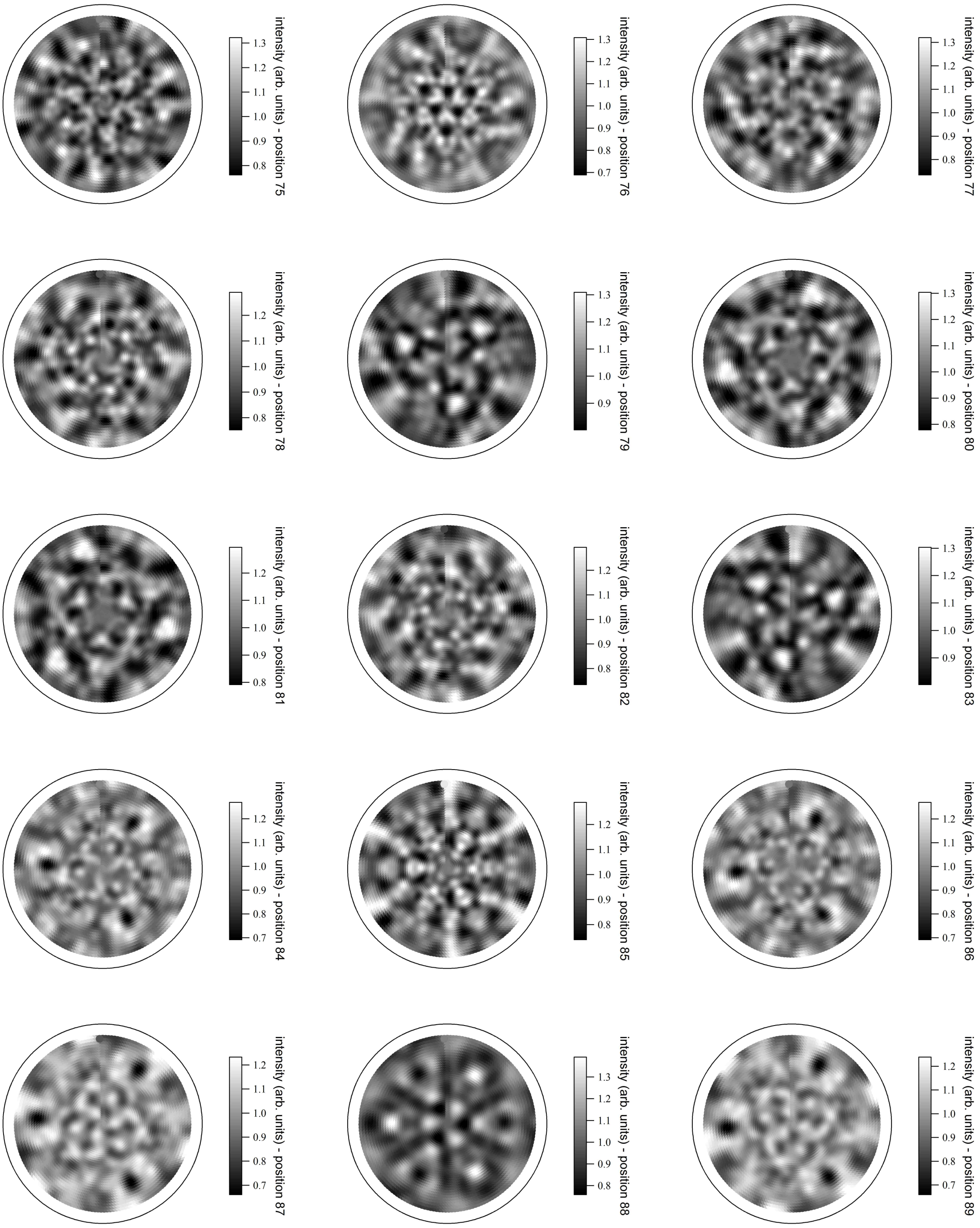

Figure 84: Single Simulation Sets (3-fold average and ϕ-averaged): 75 to 89.

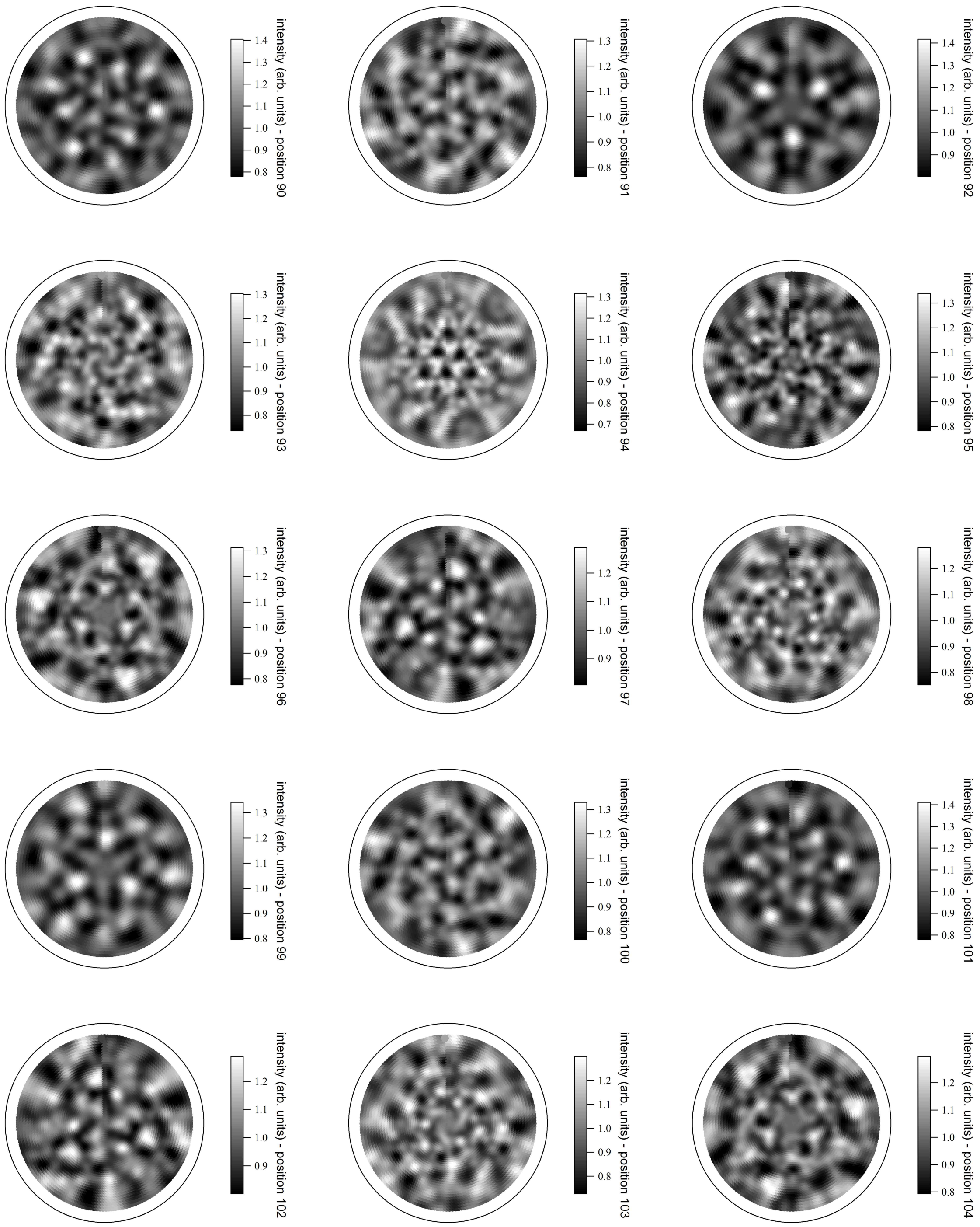

Figure 85: Single Simulation Sets (3-fold average and ϕ-averaged): 90 to 104.

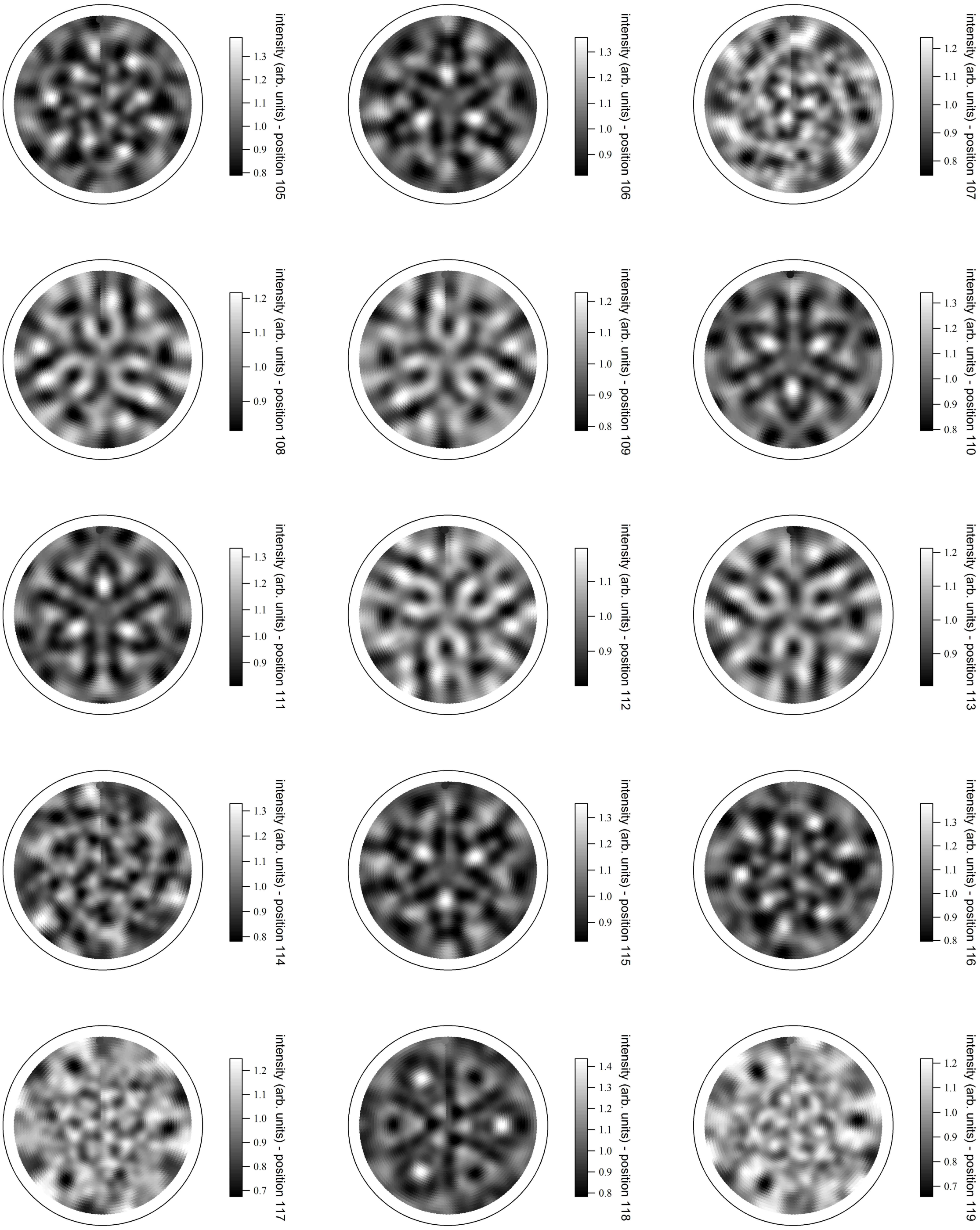

Figure 86: Single Simulation Sets (3-fold average and ϕ-averaged): 105 to 119.

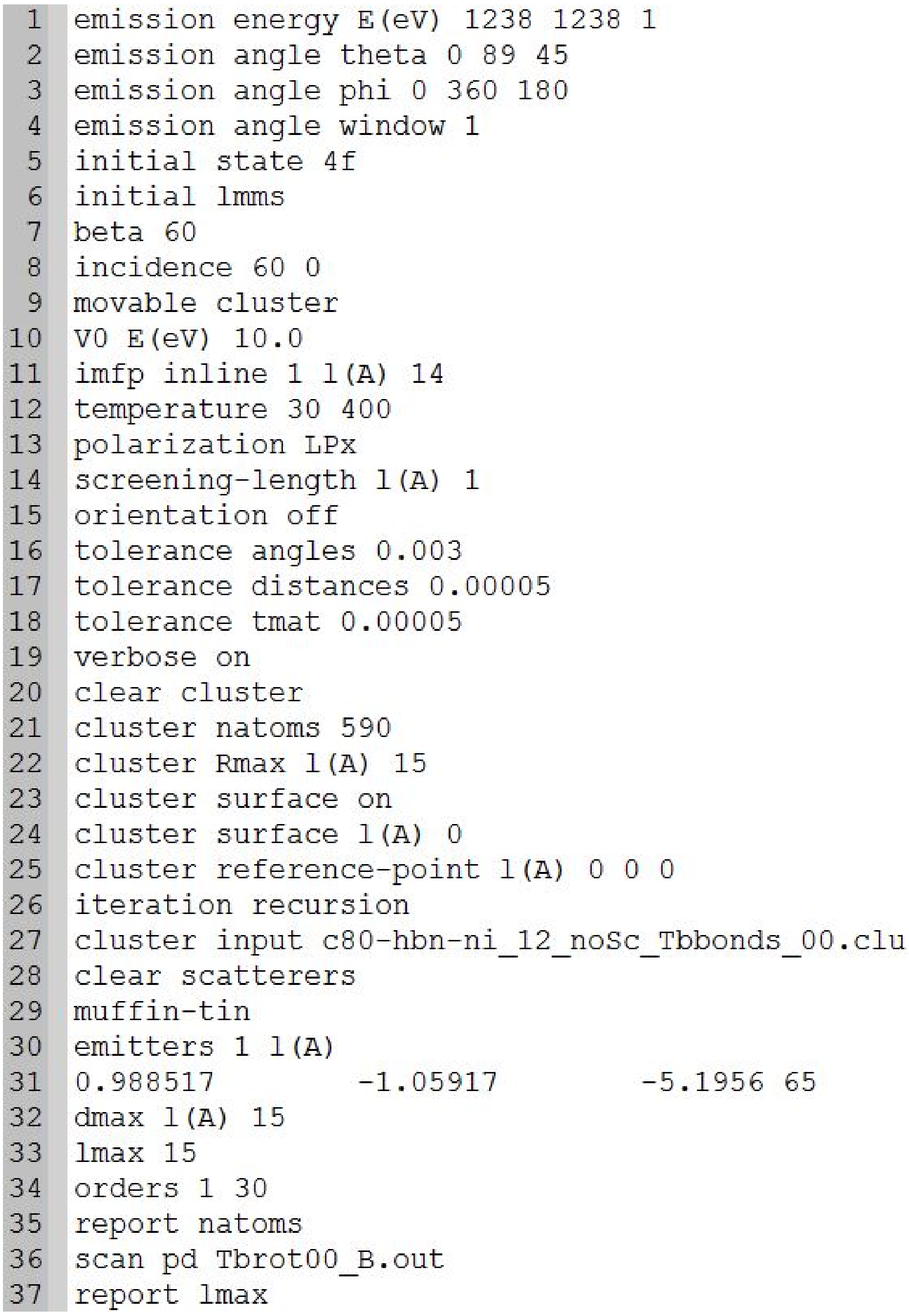

```
emission energy E(eV) 1238 1238 1
emission angle theta 0 89 45
emission angle phi 0 360 180
emission angle window 1
initial state 4f
initial lmms
beta 60
incidence 60 0
movable cluster
V0 E(eV) 10.0
imfp inline 1 l(A) 14
temperature 30 400
polarization LPx
screening-length l(A) 1
orientation off
tolerance angles 0.003
tolerance distances 0.00005
tolerance tmat 0.00005
verbose on
clear cluster
cluster natoms 590
cluster Rmax l(A) 15
cluster surface on
cluster surface l(A) 0
cluster reference-point l(A) 0 0 0
iteration recursion
cluster input c80-hbn-ni_12_noSc_Tbbonds_00.clu
clear scatterers
muffin-tin
emitters 1 l(A)
0.988517        -1.05917        -5.1956 65
dmax l(A) 15
lmax 15
orders 1 30
report natoms
scan pd Tbrot00_B.out
report lmax
```

Figure 87: Example EDAC input file for a single calculation.

E. Fermi edge of $TbSc_2N@C_{80}$/h-BN/Ni(111)

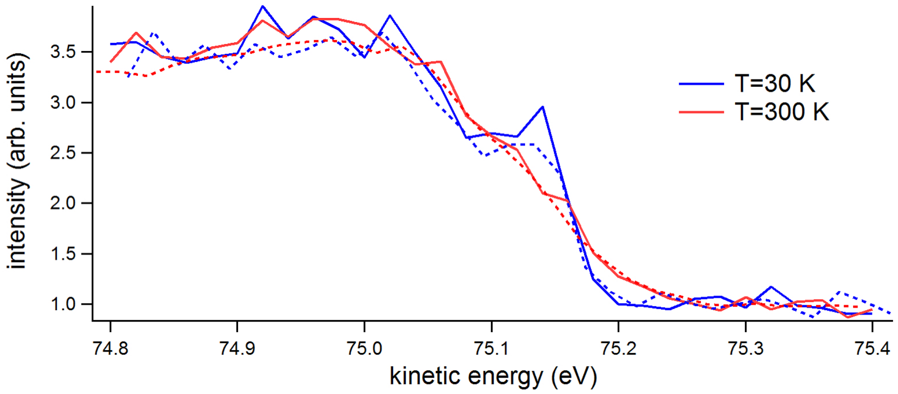

Figure 88: Fermi edge measured using a photon energy of $h\nu = 70$ eV for two different preparations at $T = 300$ K (red) and $T = 30$ K (blue). The full line and the dashed line account each for one preparation.

The Fermi edge, resolved at a photon energy of $h\nu = 70$ eV (Figure 88) shows the reproducible possible electronic state at $T = 30$ K in contrary to the measurements performed at $T = 300$ K.

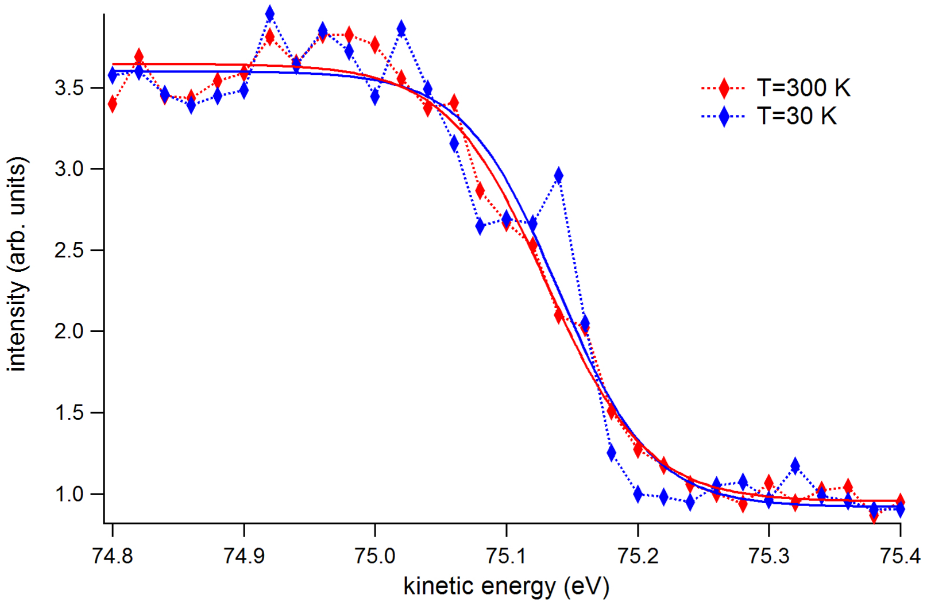

Figure 89: Fit of the Fermi edge to determine the energy resolution, following Equation 35.

Despite the reproducibility the resolution of the PEARL beamline at $h\nu = 70$ eV is limited and a Fermi fit under inclusion of the machine resolution, following

$$f_{\text{Fermi}}(E,T) \rightarrow f_{\text{Fermi}}\left(E, \sqrt{T^2 + \left(\frac{\Delta E^{\text{exp}}}{4k_B}\right)^2}\right), \tag{35}$$

where E is the energy, T the temperature, ΔE^{exp} the energy resolution and k_B the Boltzmann constant [138], as shown in Figure 89, results in a machine resolution of $\Delta E = 0.10 \pm 0.04$ eV and $\Delta E = 0.11 \pm 0.02$ eV for $T = 30$ K and $T = 300$ K, respectively. Hence, the data points around $E_K = 75.2$ eV are intriguing but below machine resolution.

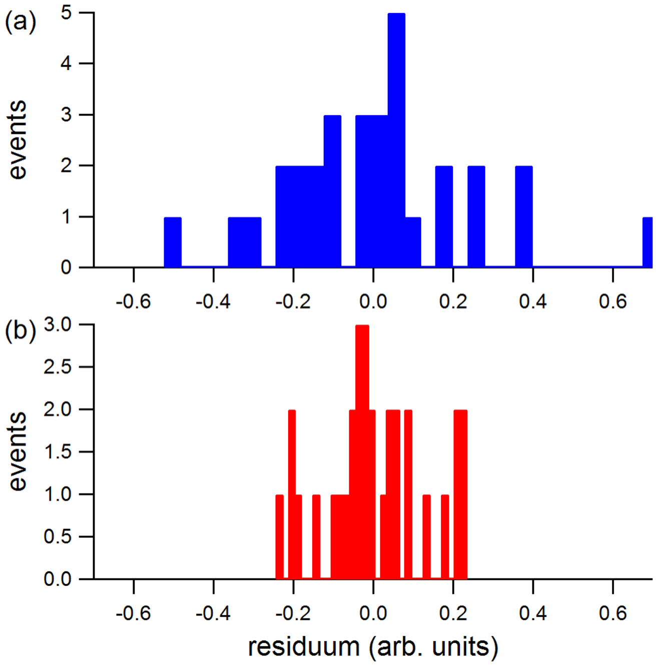

Figure 90: Histograms of the residua of Figure 89: (a) $T = 30$ K, (b) $T = 300$ K.

The histograms of the residua, as shown in Figure 90, show the difference between the room temperature sample (Figure 90b) and $T = 30$ K (Figure 90a). Several statistical differences between the measurements for low temperature and room temperature hint for the possible existence of an additional electronic state.

References

[1] G. E. Moore. Electronics, 38(8):114–117, 1965.

[2] Wgsimon, 2011.

[3] M. M. Waldrop. Nature, 530:144–147, 2016.

[4] J. Gittleman, B. Abeles, and S. Bozowski. Phys. Rev. B, 9(9):3891, 1974.

[5] S. Wolf, D. Awschalom, R. Buhrman, J. Daughton, S. von Molnár, M. Roukes, A. Chtchelkanova, and D. Treger. Science (New York, N.Y.), 294(5546):1488–1495, 2001.

[6] A. Nagashima, N. Tejima, Y. Gamou, T Kawai, and C. Oshima. Phys. Rev. Lett., 75(21):3918–3921, 1995.

[7] R. M. Desrosiers, D. W. Greve, and A. J. Gellman. Surf. Sci., 382:35–48, 1997.

[8] T. Greber, L. Brandenberger, M. Corso, A. Tamai, and J.Osterwalder. e-Journal of Surface Science and Nanotechnology, 4:410–413, 2006.

[9] L. Paffett, R. Simonson, P. Papin, and R. Paine. Surf. Sci., 232:286–296, 1990.

[10] F. Müller, K. Stöwe, and H. Sachdev. Chemistry of Materials, 17:3464–3467, 2005.

[11] E. Ćavar, R. Westerström, A. Mikkelsen, E. Lundgren, A. S. Vinogradov, M. L. Ng, A. B. Preobrajenski, A. A. Zakharov, and N. Mårtensson. Surf. Sci., 602:1722–1726, 2008.

[12] A. B. Preobrajenski, M.A. Nesterov, M. L. Ng, A. S. Vinogradov, and N. Mårtensson. Chem. Phys. Lett., 446:119–123, 2007.

[13] M. Corso, W. Auwärter, M. Muntwiler, A. Tamai, T. Greber, and J. Osterwalder. Science (New York, N.Y.), 303(5655):217–220, 2004.

[14] S. Berner, M. Corso, R. Widmer, O. Groening, R. Laskowski, P. Blaha, K. Schwarz, A. Goriachko, H. Over, S. Gsell, M. Schreck, H. Sachdev, T. Greber, and J. Osterwalder. Z. Angew. Chem. (International ed.), 46(27):5115–5119, 2007.

[15] M. Morscher, M. Corso, T. Greber, and J. Osterwalder. Surf. Sci., 600:3280–3284, 2006.

[16] D. Martoccia, P. R. Willmott, T. Brugger, M. Björck, S. Günther, C. M. Schlepütz, A. Cervellino, S. A. Pauli, B. D. Patterson, S. Marchini, J. Wintterlin, W. Moritz, and T. Greber. Phys. Rev. Lett., 101:126102, 2008.

[17] R. Sessoli, H.-L. Tsai, A. R. Schake, S. Wang, J. B. Vincent, K. Folting, D. Gatteschi, G. Christou, and D. N. Hendrickson. J. Am. Chem. Soc., 115:1804–1816, 1993.

[18] D. Gatteschi, R. Sessoli, and J. Villain. Molecular Nanomagnets. 2006.

[19] D. Woodruff, R. Winpenny, and R. Layfield. Chemical reviews, 113(7):5110–5148, 2013.

[20] M. Mannini, F. Pineider, C. Danieli, F. Totti, L. Sorace, Ph. Sainctavit, M.-A. Arrio, E. Otero, L. Joly, J. C. Cezar, A. Cornia, and R. Sessoli. Nature, 468:417–422, 2010.

[21] https://apps.webofknowledge.com/.

[22] M. A. Aldamen, J. M. Clemente-Juan, E. Coronado, C. Martí-Gastaldo, and A. Gaita-Ariño. J. Am. Chem. Soc., 130:8874–8875, 2008.

[23] N. Ishikawa, M. Sugita, T. Ishikawa, S. Koshihara, and Y. Kaizu. J. Am. Chem. Soc., 125:8694–8695, 2003.

[24] C. Zaleski, E. Depperman, J. Kampf, M. Kirk, and V. Pecoraro. Angewandte Chemie (International ed. in English), 43(30):3912–3914, 2004.

[25] M. A. Antunes, L. C. J. Pereira, I. C. Santos, M. Mazzanti, J. Marçalo, and M. Almeida. Inorg. Chem., 50:9915–9917, 2011.

[26] P. Arnold. Nature chemistry, 4(12):967–969, 2012.

[27] B. G. Wybourne. Spectroscopic Properties of Rare Earths. Interscience (Wiley), New York, 1965.

[28] S. Hüfner. Photoelectron Spectroscopy. Springer, 2003.

[29] G. Ertl and J. Küppers. Low Energy Electrons and Surface Chemistry. VCH,Weinheim, 1985.

[30] J. Osterwalder. Surface Analysis by Auger and X-ray Photoelectron Spectroscopy (Chapter 20). IM Publications and Surface Spectra Limited, 2003. edited by D. Briggs and J. Grant.

[31] R. G. Steinhardt and E. J. Serfass. Anal. Chem., 23:1585–1590, 1951.

[32] A. Fahlman and K. Siegbahn. Arkiv for Fysik, 32:111, 1966.

[33] A. Einstein. Analen der Physik, 17:132, 1905.

[34] W. E. Spicer. Phys. Rev., 112:114–122, 1958.

[35] J. J. Yeh and I. Lindau. At. Data. Nucl. Data Tables, 32:1–155, 1985.

[36] C. Guillot, Y. Ballu, J. Paigne, J. Lecante, K. P. Jain, P. Thiry, R. Pinchaux, Y. Petroff, and L. M. Falicov. Phys. Rev. Lett., 39:1632–1635, 1977.

[37] W. Mehlhorn. Atomic Inner Shell Physics. Physics of Atoms and Molecules, 1985. edited by B. Crasemann.

[38] C. Laubschat, E. Weschke, G. Kalkowski, and G. Kaindl. Physica Scripta, 41:124–129, 1990.

[39] U. Fano. Phys. Rev., 124(6):1866, 1961.

[40] J. Osterwalder, T. Greber, A. Stuck, and L. Schlapbach. Phys. Rev. B, Condensed matter, 44(24):13764–13767, 1991.

[41] T. Greber, J. Wider, E. Wetli, and J. Osterwalder. Phys. Rev. Lett., 81:1654–1657, 1998.

[42] D. J. Friedman and C. S. Fadley. J. Electron Spectrosc. Relat. Phenom., 51:689–700, 1990.

[43] A. P. Kaduwela, D. J. Friedman, and C. S. Fadley. J. Electron Spectrosc. Relat. Phenom., 57:223, 1991.

[44] F. J. García de Abajo, M. A. Van Hove, and C. S. Fadley. Phys. Rev. B, 63:075404, 2001.

[45] R. Stania, W. Heckel, I. Kalichava, C. Bernard, T. C. Kerscher, H. Y. Cun, P. R. Willmott, B. Schönfeld, J. Osterwalder, S. Müller, and T. Greber. Phys. Rev. B, 93:161402, 2016.

[46] http://www.dl.ac.uk/MEIS/stereographs/.

[47] D. Naumovic, A. Stuck, T. Greber, J. Osterwalder, and L. Schlapbach. Phys. Rev. B, Condensed matter, 47(12):7462–7479, 1993.

[48] http://www.parkafm.com/images/spmmodes/electrical/.

[49] H. B. G. Casimir and F. K. du Pré. Physica, 5:507–511, 1938.

[50] M. Treier, P. Ruffieux, R. Fasel, F. Nolting, S. Yang, L. Dunsch, and T. Greber. Phys. Rev. B, 80:081403, 2009.

[51] F. C. Frank and J. H. van der Merwe. Proceedings of the Royal Society of London, Series A, 198:205–216, 1949.

[52] I. N. Stranski and L Krastanow. Zeitschrift für Kristallographie, 99:444–448, 1938.

[53] M. Volmer and A. Weber. Z. Phys. Chem, 119:277–301, 1926.

[54] T. Greber, O. Raetzo, T. Kreutz, P. Schwaller, W. Deichmann, E. Wetli, and J. Osterwalder. Rev. Sci. Instrum., 68(12):4549–4554, 1997.

[55] A. Hemmi, H.Y Cun, S. Roth, J. Osterwalder, and T. Greber. J. Vac. Sci. Technol., 32:023202, 2014.

[56] W. Auwärter, T. J. Kreutz, T. Greber, and J. Osterwalder. Surf. Sci., 429:229–236, 1999.

[57] H. Petersen, C. Jung, C. Hellwig, W. B. Peatman, and W. Gudat. Rev. Sci. Instrum., 66(1):1–14, 1995.

[58] P. Oberta, U. Flechsig, M. Muntwiler, and C. Quitmann. Nuclear Instruments and Methods in Physics Research Section A: Accelerators, Spectrometers, Detectors and Associated Equipment, 635:116–120, 2011.

[59] VG Scienta. Instrument Manual SCIENTA EW4000, volume v1.1. 2012.

[60] M. Muntwiler, J. Zhang, R. Stania, F. Matsui, P. Oberta, U. Flechsig, L. Patthey, C. Quitmann, T. Glatzel, R. Widmer, E. Meyer, T. A. Jung, P. Aebi, T. Greber, and R. Fasel. submitted, 2016.

[61] H. Y. Cun, M. Iannuzzi, A. Hemmi, S. Roth, J. Osterwalder, and T. Greber. Nano Lett., 13(5):2098–2103, 2013.

[62] P. Willmott, D. Meister, S. Leake, M. Lange, A. Bergamaschi, M. Böge, M. Calvi, C. Cancellieri, N. Casati, A. Cervellino, Q. Chen, C. David, U. Flechsig, F. Gozzo, B. Henrich, S. Jäggi-Spielmann, B. Jakob, I. Kalichava, P. Karvinen, J. Krempasky, A. Lüdeke, R. Lüscher, S. Maag, C. Quitmann, M. Reinle-Schmitt, T. Schmidt, B. Schmitt, A. Streun, I. Vartiainen, M. Vitins, X. Wang, and R. Wullschleger. J. Synchr. Rad., 20(Pt 5):667–682, 2013.

[63] Ch. Steiner, B. Schönfeld, M. J. Portmann, M. Kompatscher, G. Kostorz, A. Mazuelas, T. Metzger, J. Kohlbrecher, and B. Demé. Phys. Rev. B, 71:104201, 2005.

[64] E. Platzgummer, M. Sporn, R. Koller, S. Forsthuber, M. Schmid, W. Hofer, and P. Varga. Surf. Sci., 419:236, 1999.

[65] T. Greber. Handbook Of Nanophysics (Chapter 18). CRC Press, 2010. edited by K. D. Sattler.

[66] S. Doniach and M. Šunjić. Journal of Physics C: Solid State Physics, 3:285–291, 1970.

[67] D. Shirley. Phys. Rev. B, 5(12):4709–4714, 1972.

[68] G. Kresse and J. Furthmüller. Phys. Rev. B, 54(16):11169, 1996.

[69] G. Kresse and J. Furthmüller. Comp. Mat. Sci., 6:15, 1996.

[70] J. M. Sanchez, F. Ducastelle, and D. Gratias. Physica, 128A:334, 1984.

[71] D. Lerch, O. Wieckhorst, G. L. W. Hart, R. W. Forcade, and S. Müller. Modelling Simul. Mater. Sci. Eng., 17:055003, 2009.

[72] P. E. Blöchl. Phys. Rev. B, 50(24):17953, 1994.

[73] G. Kresse and D. Joubert. Phys. Rev. B, 59(3):1758, 1999.

[74] J. P. Perdew, J. A. Chevary, S. H. Vosko, K. A. Jackson, M. R. Pederson, D. J. Singh, and C. Fiolhais. Phys. Rev. B, 46(11):6671, 1992.

[75] S. Müller, M. Stöhr, and O. Wieckhorst. Appl. Phys. A, 82:415, 2006.

[76] P. Welker, O. Wieckhorst, T. C. Kerscher, and S. Müller. J. Phys.: Condens. Matter, 22:384203, 2010.

[77] S. B. Maisel, T. C. Kerscher, and S. Müller. Acta Materi., 60:1093, 2012.

[78] T. C. Kerscher, W. Landgraf, R. Podloucky, and S. Müller. Phys. Rev. B, 86:195420, 2012.

[79] J. Klimeš, D. R. Bowler, and A. Michaelides. J. Phys.: Condens. Matter, 22:022201, 2010.

[80] J. Klimeš, D. R. Bowler, and A. Michaelides. Phys. Rev. B, 83:195131, 2011.

[81] H. J. Monkhorst and J. D. Pack. Phys. Rev. B, 13:5188–5192, 1976.

[82] G. Makov and M. C. Payne. Phys. Rev. B, 51:4014–4022, 1995.

[83] J. Neugebauer and M. Scheffer. Phys. Rev. B, 46:16067–16080, 1992.

[84] M. Schmid and P. Varga. The Chemical Physics of Solid Surfaces, 10:118–151, 2002.

[85] H. C. Siegmann, L. Schlapbach, and C. R. Brundle. Phys. Rev. Lett., 40(14):972–975, 1978.

[86] K. J. Mayrhofer, V. Juhart, K. Hartl, M. Hanzlik, and M. Arenz. Z. Angew. Chem. (International ed.), 48(19):3529–3531, 2009.

[87] F. F. Abraham. Phys. Rev. Lett., 46:546–549, 1980.

[88] B. C. Han, A. Van der Ven, G. Ceder, and B. J. Hwang. Phys. Rev. B, 72:205409, 2005.

[89] F. Esch, S. Günther, E. Schütz, A. Schaak, I. G. Kevrekidis, M. Marsi, M. Kiskinova, and R. Imbihl. Surf. Sci., 443:245–252, 1999.

[90] P. Sutter, J. T. Sadowski, and E. A. Sutter. J. Am. Chem. Soc., 132:8175–8179, 2010.

[91] E. Grånäs, M. Andersen, M. A. Arman, T. Gerber, B. Hammer, J. Schnadt, J. N. Andersen, T. Michely, and J. Knudsen. J. Phys. Chem. C, 117:16438–16447, 2013.

[92] A. Nierhoff, C. Conradsen, D. McCarthy, T. P. Johansson, J. Knudsen, and I. Chorkendorff. Catalysis Today, 244:130–135, 2015.

[93] H. Y. Cun, M. Iannuzzi, A. Hemmi, J. Osterwalder, and T. Greber. ACS nano, 8(7):7423–7431, 2014.

[94] A. B. Preobrajenski, A. S. Vinogradov, M. L. Ng, E. Ćavar, R. Westerström, A. Mikkelsen, E. Lundgren, and N. Mårtensson. Phys. Rev. B, 75:245412, 2007.

[95] C. S. Fadley. Progress in Surface Science, 16(3):275–388, 1984.

[96] J. Wider, F. Baumberger, M. Sambi, R. Gotter, A. Verdini, F. Bruno, D. Cvetko, A. Morgante, T. Greber, and J. Osterwalder. Phys. Rev. Lett., 86(11):2337–2340, 2001.

[97] R. Laskowski and P. Blaha. Phys. Rev. B, 81:075418, 2010.

[98] K. Momma and F. Izumi. Journal of Applied Crystallography, 44(6):1272–1276, 2011.

[99] H. W. Kroto, J. R. Heath, S. C. O'Brien, R. F. Curl, and R. E. Smalley. Nature, 318:162–163, 1985.

[100] S. Stevenson, G. Rice, T. Glass, K. Harich, F. Cromer, M. R. Jordan, J. Craft, E. Hadju, R. Bible, M. M. Olmstead, K. Maitra, A. J. Fisher, A. L. Balch, and H. C. Dorn. Nature, 401:55–57, 1999.

[101] R. Westerström, J. Dreiser, C. Piamonteze, M. Muntwiler, S. Weyeneth, H. Brune, S. Rusponi, F. Nolting, A. Popov, S. Yang, L. Dunsch, and T. Greber. Journal of the American Chemical Society, 134(24):9840–9843, 2012.

[102] H. Kroto. Nature, 329:529–531, 1987.

[103] http://www.nanotube.msu.edu/fullerene/fullerene.php?C=80.

[104] J. C. Duchamp, A. Demortier, K. R. Fletcher, D. Dorn, E. B. Iezzi, T. Glass, and H. C. Dorn. Chem. Phys. Lett., 375:655–659, 2003.

[105] K. Nakao, N. Kurita, and M. Fujita. Phys. Rev. B, Condensed matter, 49(16):11415–11420, 1994.

[106] M. Morscher. Dissertation: Tools for Investgating Molecular Magnetism: A New Mott Detector and Resonant Photoelectron Diffraction with Circular Dichrosim. 2009.

[107] G. B. Grad, P. Blaha, K. Schwarz, W. Auwärter, and T. Greber. Phys. Rev. B, 68:085404, 2003.

[108] R. Fasel, P. Aebi, R. G. Agostino, D. Naumovic, J. Osterwalder, A. Santaniello, and L. Schlapbach. Phys. Rev. Lett., 76(25):4733–4736, 1996.

[109] A. Santaniello. Fullerenes and Fullerene Nanostructures. World Scientific, Singapore, 1996. edited by H. Kuzmany and J. Fink and M. Mehring and S. Roth.

[110] R. Fasel, R. G. Agostino, P. Aebi, and L. Schlapbach. Phys. Rev. B, 60(7):4517, 1999.

[111] M. Muntwiler, W. Auwärter, A. Seitsonen, J. Osterwalder, and T. Greber. Phys. Rev. B, 71:121402, 2005.

[112] D. F. Leigh, C. Nörenberg, D. Cattaneo, J. H. G. Owen, K. Porfyrakis, A. Li Bassi, A. Ardavan, and G. A. D. Briggs. Surf. Sci., 601:2750–2755, 2007.

[113] C. Nörenberg, D. F. Leigh, D. Cattaneo, K. Porfyrakis, A. Li Bassi, C. S. Casari, M. Passoni, J. H. G. Owen, and G. A. D. Briggs. Journal of Physics: Conference Series, 100:052080, 2008.

[114] M. Morscher, A. P. Seitsonen, S. Ito, H. Takagi, N. Dragoe, and T. Greber. Phys. Rev. A, 82:051201, 2010.

[115] T. Huang, J. Zhao, M. Feng, A. Popov, S. Yang, L. Dunsch, and H. Petek. Nano letters, 11(12):5327–5332, 2011.

[116] R. Westerström, A.-C. Uldry, R. Stania, J. Dreiser, Cinthia Piamonteze, M. Muntwiler, F. Matsui, S. Rusponi, H. Brune, S. Yang, A. Popov, B. Büchner, B. Delley, and T. Greber. Phys. Rev. Lett., 114(8):087201, 2015.

[117] W. Krätschmer, L. Lamb, K. Fostiropoulos, and D. Huffman. Nature, 347:354–358, 1990.

[118] A. Svitova, K. Braun, A. Popov, and L. Dunsch. ChemistryOpen, 1(5):207–210, 2012.

[119] https://vuo.elettra.eu/services/elements/WebElements.html.

[120] Y. Gamou, M. Terai, and A. Nagashima. Sci. rep. RITU, A44:211–214, 1997.

[121] R. Stania. Master Thesis: Lateral Segregation in *h*-BN/PtRh(111), 2012.

[122] M. Treier. Dissertation: Novel Approaches to the Bottom-up Fabrication of Ordered Organic Nanostructures on Metal Surfaces. 2009.

[123] A. Seitsonnen, DFT calculations, unpublished.

[124] P. A. Heiney, J. E. Fischer, A. R. McGhie, W. J. Romanow, A. M. Denenstein, Jr. P. P. McCauley, III A. B. Smith, and D. E. Cox. Phys. Rev. Lett., 66(22):2911–2914.

[125] W. Wernsdorfer, N. Aliaga-Alcalde, D. Hendrickson, and G. Christou. Nature, 416(6879):406–409, 2002.

[126] L. Dunsch and S. Yang. Small, 3:1298–1320, 2007.

[127] L. H. Ahrens. Cosmochim. Acta, 2:155–169, 1952.

[128] J. Onoe, A. Nakao, and K. Takeuchi. Phys. Rev. B, 55(15):10051, 1997.

[129] P. J. Benning, F. Stepniak, and J. H. Weaver. Phys. Rev. B, 48(12):9086–9096, 1993.

[130] A. Goldoni, C. Cepek, and S. Modesti. Phys. Rev. B, 54(4):2890–2895, 1996.

[131] S. Stevenson, C. J. Chancellor, H. M. Lee, M. M. Olmstead, and A. L. Balch. Inorganic Chemistry, 47:1420–1427, 2008.

[132] A. Popov, C. Chen, S. Yang, F. Lipps, and L. Dunsch. ACS nano, 4(8):4857–4871, 2010.

[133] M. Qian, S. V. Ong, S. N. Khanna, and M. B. Knickelbein. Phys. Rev. B, 75:104424, 2007.

[134] L. C. Davis. Journal of Applied Physics, 59:R25–R63, 1986.

[135] P. Krüger, S. Bourgeois, B. Domenichini, H. Magnan, D. Chandesris, P. Le Fèvre, A. Flank, J. Jupille, L. Floreano, A. Cossaro, A. Verdini, and A. Morgante. Phys. Rev. Lett., 100(5):055501, 2008.

[136] A. Lodi Rizzini, C. Krull, T. Balashov, A. Mugarza, C. Nistor, F. Yakhou, V. Sessi, S. Klyatskaya, M. Ruben, S. Stepanow, and P. Gambardella. Nano Lett., 12(11):5703–5707, 2012.

[137] A. Popov, S. Yang, and L. Dunsch. Chem. Rev., 113(8):5989–6113, 2013.

[138] T. J. Kreutz, T. Greber, P. Aebi, and J. Osterwalder. Phys. Rev. B, 58(3):1300–1317, 1998.

Curriculum Vitae

Name	Roland Stania
Birthday	6.4.1978
Place of Birth	Bonn, Germany
Nationality	German

Education

06/2012 - present	PhD studies: *Nanotemplates and Conformations of Tri-Metal Endofullerenes on Surfaces*; Surface Physics group of Prof. Dr. J. Osterwalder and Prof. Dr. T. Greber
05/2012	Master of Science degree in Physics, University of Zurich: *Lateral Segregation in h-BN/PtRh(111)*; Surface Physics group of Prof. Dr. J. Osterwalder and Prof. Dr. T. Greber
03/2011 - 05/2012	Advanced courses in condensed matter, University of Zurich
03/2011	Bachelor of Science in Physics, University of Zurich: *Holographische Untersuchung an Graphitflakes*; Biophysics group of Prof. Dr. W. Fink
01/2009 - 03/2011	Bachelor studies in physics, University of Zurich
10/2003 - 06/2007	Advanced courses in physics and biophysics, Ludwig-Maximilians-Universität Munich
09/2000 - 09/2003	Intermediate Diploma in Physics, Ludwig-Maximilians-Universität Munich
06/1999	Eidgenössische Matura, Typus-C, Kantonsschule Alpenquai, Luzern

Teaching Experience

2012 HS - 2013 HS	Tutoring Assistant: Physics for Chemists and Biologists I & II (PHY 117/127)
2014 FS	Laboratory Assistance: Physics II (PHY 122)
2014 HS	Tutoring Assistant: Physics I & II (PHY 111/121)
2015 HS	Tutoring Assistant: Physics for Chemists I (PHY 118)